מכון ויצמן למדע
WEIZMANN INSTITUTE OF SCIENCE

Thesis for the degree

Doctor of Philosophy

עבודת גמר (תזה) לתואר

דוקטור לפילוסופיה

Submitted to the Scientific Council of the

Weizmann Institute of Science

Rehovot, Israel

מוגשת למועצה המדעית של

מכון ויצמן למדע

רחובות, ישראל

By

Eran Erdal

מאת

ערן ארדל

פיתוח קונספטים חדשים של גלאי קרינה מבוססי נוזל אציל עבור אירועים נדירים

Development of novel concepts of noble-liquid detectors for rare-event searches

Advisors:

Prof. Amos Breskin

Dr. Shikma Bressler

מנחים:

פרופ' עמוס ברסקין

ד"ר שקמה ברסלר

August, 2020

אב, התש"ף

Contents

1 Acknowledgements

It is my great pleasure to thank all those who assisted me during my Ph.D. thesis research period.

First and foremost, I would like to extend special and cordial thanks to my supervisors **Prof. Amos Breskin** and **Dr. Shikma Bressler** who granted me an opportunity to take active part in the cutting edge research of particle detection techniques, by guiding my project using their vast knowledge and experience. Their never-ending devotion, support and attention, both to my project and to me personally extends far beyond expectations and has been invaluable.

Very special thanks to **Dr. Lior Arazi** for his co-guidance and assistance and for countless hours spent together in the laboratory and in meaningful conversations.

Cordial thanks to **Dr. Michael Rappaport** for sharing with me the intimate secrets of vacuum, cryogenics and laboratory hardware, without which my projects could have never been as successful.

To **Dr. David Vartsky** and for being a partner in research, a helping hand, a guide and a friend.

To all my former and current lab colleagues and mates: **Dr. Sergei Shchemelinin**, **Dr. Artur Coimbra**, **Dr. Itamar Israelashvili**, **Dr. Arindam Roy**, **Dr. Purba Battacharia**, **Yevgeniya Korotinsky**, **Dr. Luca Moleri**, **Darina Zavazieva**, **Abhik Jash**, and **Andrea Tesi**, for useful conversations and for their support whenever and wherever needed.

To **Oz Diner** and **Benjamin Pasmantirer** for their elegant design of my setups and to **Haim Sade**, **the workshop team** and to **Yoel Chalaf** for their devotion to the all of my construction projects. To **Yehuda Asher** for his help, knowledge and guidance in all mechanical aspects.

To the best administrative team I could have ever imagined: **Michal Hirshberg**, **Hemda Atziz**, **Natalia Leybovich**, **Revital Ackler**, **Hadar Alper**, **Yuri Yegudaev**, **Amir Bar-On** and **Hila Shtudiner** for their proficient and efficient support. But most of all, for creating a vivid and happy environment that makes one smile every morning.

To my life partner **Eliav** for encouraging me and supporting me through every step of the way. To my very special family and friends, **Shimon and Rotem**, **Mandy and Judith, Odi and Yoav** and **Miriam and Ido**, without whom this could have never been achieved. To my sister **Talia**, who always found a good way to explain to the world what her brother is working on. And finally to **my Mother**, who was the proudest of all when I started this journey, and who would have been the proudest to see its end.

2 Declaration

I hereby declare that this presented work summarizes my independent research.

The entire work was conducted in collaboration with colleagues from Weizmann Institute of Science. In particular with Dr. Lior Arazi (2015 – 2017 as part of the Weizmann Institute of Science, since 2017 at Ben Gurion University), Dr. David Vartsky, Dr. Sergei Shchemelinin Dr. Arindam Roy, Andrea Tesi, Dr. Michael L. Rappaport and Dr. Enrico Segre.

The work on the cryogenic RPWELL was done in collaboration with our colleagues at Instituto de Cerámica de Galicia.

3 Abstract

Over the past two decades, noble-liquid detectors have come to play a leading role in several fields of physics requiring rare events detection. Typical examples are neutrino physics and dark-matter searches. Particle interactions in noble liquids result in light and charge signatures, which can propagate with little attenuation over large distances. This, along with their high density and scalability, turns them into a preferred option for experiments requiring large target masses with ultra-low background, event topology reconstruction, and high sensitivity to radiation-induced low-energy depositions. The leading noble-liquid detectors instruments are dual-phase Time Projection Chambers (TPC). While many TPC-signal readout technologies exist, there is concern regarding their scalability into the planned multi-ton size experiments.

The novel concept of the Liquid Hole Multiplier, LHM, the topic of this thesis work, was conceived as a single-element sensor for combined detection of radiation-induced ionization charges and scintillation light in a noble-liquid detection media. It suggests detection of ionization-electrons and UV-induced photoelectrons, through electroluminescence (EL) occurring in a gas bubble trapped under a CsI-coated perforated electrode immersed in the noble liquid.

The work done during the course of this Ph.D. aimed at deeper understanding of the mechanisms governing the operation and performance of the “bubble-assisted Liquid Hole Multiplier”. Most of the research has been carried out in liquid xenon (LXe). The first chapter in the results section establishes the experimental procedures performed in order to build and operate an LHM detector. It is followed by a comparative study of different electrode geometries in terms of light yield, energy resolution, timing resolution and relative photon detection efficiency. It is followed by a study of the photon detection efficiency and of radiation imaging using Silicon Photomultipliers. A first demonstration of LHM operation in liquid argon (LAr) is also presented. The last three chapters present new ideas related to the LHM detector concept: a double-stage LHM, an LHM with a vertical electrode and generation of EL between two parallel meshes.

Each chapter concludes with a short discussion. The final discussion summarizes all achievements, the remaining open questions to be investigated (along with some experimental suggestions) as well as some ideas for possible implementation in future Dark Matter experiments.

In addition, a second concept for charge multiplication, the cryogenic Resistive Plate WELL detector (RPWELL), has been suggested. The work however could not be completed due to difficulty in obtaining suitable resistive materials. Work in this context appears as an appendix to the thesis.

4 Introduction

Over the past two decades, noble liquid detectors have come to play a leading role in several fields of physics requiring rare events detection; examples are in direct dark matter (DM) searches [1-3], neutrino experiments [4] and rare hypothetical processes such as neutrino-less double beta decay [5], proton decay [6] and the $\mu \rightarrow e\gamma$ decay [7]. Noble-liquid detectors are also applicable in Compton medical-imaging cameras [8] and gamma & neutron radiography in homeland security [9-11]. Particle interactions in noble liquids result in large light and charge signals, which can propagate with little attenuation over large distances. This, along with their high density and scalability, turns them into a preferred technological option for experiments requiring large target masses with ultra-low background, event topology reconstruction, and high sensitivity to radiation-induced low-energy deposition [3].

4.1 Interaction with the noble liquid

Detection of particles and radiation in noble liquid detectors begins with their interaction with the noble liquid atoms. This primary interaction may lead to the emission of charged particles, depositing their energy in terms of heat, ionization and excitation. The two latter are the detectable form of energy depositions relevant to this work. The nature of the primary interaction depends on the particle, its energy and cross section for different processes. Photons, for example, interact with matter mostly through the processes of photoelectric absorption, Compton scattering or pair production [12]. All three interaction channels result finally in the emission of an electron inside the liquid volume. Neutrons on the other hand, interact mainly through scattering off the liquid nuclei [13]. Interactions can be either elastic, resulting in a recoil of the entire nucleus, or inelastic when energy reaches (or exceeds) the MeV scale. Neutrinos, depending on their flavor and energy, may show different channels of interaction. For example, GeV scale ν_e interact in three main channels [14]: elastic scatter off electrons, charge current interaction resulting in an inverse beta decay or neutral current interaction resulting in a π^0 decaying into two gammas which interact with the noble liquid at some distance from the original interaction point. Weakly Interacting Massive particles (WIMP), which are hypothetical particles searched for in various DM experiments are expected to produce elastic nuclear recoils in the noble liquid.

Charged particles emitted by the primary interaction travel through the media, depositing their energy in the form of ionization and excitation along their track. The mean energy loss per unit distance was first described by the Bethe-Bloch formula [15]:

$$< \frac{dE}{dx} > = -\frac{4\pi}{m_e c^2} \cdot \frac{nz^2}{\beta^2} \cdot \left(\frac{e^2}{4\pi\varepsilon_0}\right)^2 \cdot \left[\ln\left(\frac{2m_e c^2 \beta^2}{I \cdot (1-\beta^2)}\right) - \beta^2\right] \qquad \text{Eqn. 1}$$

where m_e is the electron rest mass, c is the speed of light, n is the mean electronic density, β is the relativistic velocity and I is the mean excitation potential. Since, according to the above formula, the energy loss depends directly only on β, different particles traveling in the liquid with the same energy, will show different ionization patterns. For example, a 5.5 MeV alpha particle will deposit its energy along a 40 µm long track [16], while an electron with similar energy will travel ~1.2 cm [16]. Since the same energy is distributed along different track length, this also means that different particle result in different ionization densities. As will be discussed later, this is an important tool for particle identification and background suppression in noble liquid detectors.

4.2 Scintillation signal

In the absence of an external electric field, the electrons liberated by the decelerating charged particle recombine with the ions and the excited atoms return to their ground state. These processes however are not direct and involve a long chain of chemical reactions, the end of which are the formation of excited bound states of two atoms called excimers. Excimers can be formed either in a singlet or in a triplet molecular bound state. The dissociation of the excimer into two neutral atoms is accompanied by the emission of an energetic photon in the VUV range. This light pulse is normally referred to as *prompt scintillation* or *S1* pulse. The processes are shown in details in Table 1 below (from [3]).

Table 1 Deexcitation and recombination processes in LAr and LXe. R stands for LAr or LXe atom. Taken from [3].

Ion recombination	**Deexitation**
$R^+ + R + R \rightarrow R_2^+ + R$ $e^- + R_2^+ \rightarrow R^{**} + R$ $R^{**} + R \rightarrow R^* + R + heat$ $R^* + R + R \rightarrow R_2^* + R + heat$ $R_2^* \rightarrow R + R + h\nu$ (R_2^* - purely electronic excitation)	$R^* + R \rightarrow R_2^{*,\dagger}$ $R_2^{*,\dagger} + R \rightarrow R_2^* + R$ $R_2^* \rightarrow R + R + h\nu$ ($R_2^{*,\dagger}$ - excited states including vibrational states)

The timescales for photon emission (i.e. of the excimer dissociation) depends on the molecular bound state (R_2^* in Table 1). Excimers in the singlet state decay faster than those in the triplet state. The wavelengths and relevant time scales for the scintillation processes in LXe and LAr are summarized in Table 2. The ratio of excimers found in the singlet state to excimers in the triplet state is strongly correlated with the ionization density. In principle, the denser the ionization is, the more excimers are found in the singlet state. Specifically in LAr, as can be seen in Table 2, the two emission timescales differ by two orders of magnitude making it easy to measure. Therefore, the primary ionization density can be inferred by measuring the ratio of the long lived to the short lived excimers. This effect can be used, for example in LAr based DM detectors, to distinguish between the densely ionizing nuclear recoils (the signal the detector is looking for) and more sparsely ionizing electronic recoils (background) [17].

Table 2 Summary of important physical parameters of LXe and LAr.

	LXe		LAr	
Liquefaction temperature (@ 1bar)	165° K	[18]	87° K	[18]
Scintillation wavelength	175 nm	[3]	128 nm	[3]
Scintillation timescale (singlet / triplet , E=0)	34/34 ns	[3]	6.5 ns / 1000 ns	[3]
Scintillation timescale (singlet / triplet , E≠0)	2.2 ns / 27 ns	[3]	5 ns / 860 ns	[3]
Refraction index for scintillation wavelength	1.69	[19]	1.36	[20]
Scintillation yield (5.5 MeV α particle, E=0)	$3.1 \cdot 10^5$	[2]	$2.0 \cdot 10^5$	[2]
Energy gap for electrons: liquid-to-vapor	0.67 eV	[3]	0.2 eV	[3]
Electroluminescence threshold (vapor @ 1 bar)	1.6 kV/cm	[3]	2.1 kV/cm	[3]
Electroluminescence threshold (in liquid)	~ 400 kV/cm	[21]	No info found	

4.3 Ionization signal

Upon application of an external electric field, some of the electrons liberated in the primary interaction escape recombination and can be detected, as will be explained below, either directly or through some amplification process. The energy deposited in the primary interaction is distributed between scintillation and ionization, leading to anti-correlation between the two signals. In many experiments, this anti-correlation can be used to more precisely evaluate the energy deposited in the interaction [2, 3]. In addition, denser ionization results in a smaller fraction of electrons able to escape recombination. In LXe-based WIMP searches, this effect is used to distinguish between a signal of nuclear recoil and background electronic recoils (leading to sparser ionization and a lower light–to-charge ratio) [13, 22].

Furthermore, the relatively low diffusion of electrons from the interaction site until they arrive to their readout, retains to some extent the event ionization structure. Thus, with a spatially resolved charge readout, one can reconstruct the XY event topology. Knowing the drift velocity of electrons in the liquid and adding to the XY data also the time of arrival information (normally with respect to the prompt scintillation signal) allows a full 3D reconstruction of the event topology. This structure is called Time Projection Chamber (TPC) and is the basis of most noble liquid detectors today [2, 3].

There are many different advantages to understanding the energy deposition structure (or point, in the case of low-energy deposition) in a detector. First, it can be used to calibrate the energy response of the detector based on event location. Second, it can be used to reconstruct the event topology, such as is necessary for LAr-based neutrino experiments, where, upon an energetic neutrino interaction, one could reconstruct the identity, direction and energy of all outgoing particles [14]. Third, it can be used to exclude events based on their location. Examples for this are in WIMP DM matter searches where only event occurring at a central volume (the “fiducial volume”) are considered signal events, while events occurring outside of this are more likely to be neutrons-generated background events [13] [23].

However, not all the free electrons drifting from the interaction point reach the readout. Impurities in the noble liquid, and more specifically impurities which have a large electron affinity such as Oxygen and Water, tend to bind to the free moving electron, turning them into a negatively charged ion, drifting much slower than the free electron. Over a large drift path in the liquid, this effectively results in an exponential attenuation of the charge signal from the interaction point to the readout. This attenuation is usually measured in terms of “lifetime”, i.e. the time it takes for a drifting charge to be reduced by $1/e$. Continuous purification of the liquid reduces the amount of these electron capturing species and elongate the lifetime of electrons. To date, the XENON1T reported lifetime of 650 μs [24] in LXe and the protoDUNE demonstrators have reported a lifetime reaching 4 ms [25] in LAr.

4.4 Electrons extraction to vapor phase

Due to the density of the noble liquid media and the short mean free path of electrons when drifting in the liquid compared to gas, amplification processes such as electroluminescence (EL, detailed in the next section) and avalanche multiplication require extremely high (and mostly impractical to achieve) electric fields. Threshold values for EL in LXe were reported to be ~400 kV/cm for LXe [21]. Avalanche multiplication of course require even higher fields. Therefore, when charge amplification is required, electrons are drifted from the liquid and extracted into a gas phase, where EL and avalanche multiplication are possible.

Of specific interest to the forthcoming results and discussion presented in this thesis is the process of electron extraction from the liquid to the gas phase. In the presence of a free charge, the liquid in that vicinity is polarized, thus effectively generating a potential well [26] (note that this behavior is observed in liquid argon, liquid krypton and liquid xenon but not in liquid neon or liquid helium [26]). The depth of the potential well is 0.69 eV in LXe and 0.2 eV in LAr [3]. It is therefore clear that one needs an intense electric field in order to effectively extract electrons from the liquid into the vapor phase.

To the best of our knowledge, all the work done in this regards were in the context of the classical dual phase TPC (will be discussed below in details), namely when the electric field extracting the electrons is perpendicular to the interface. Efficiency of charge extraction was measured as a function of the electric field and are summarized in Figure 1 (taken from [3]). The time structure was measured by Buzulutskov et al. [27] only in LAr showing a slow (few µs) and a fast (less than ns) emission component. The fast component being hot electrons heated by the electric field and the slow component being thermionic emission of cold electrons. According to [28], no slow component has been observed in LXe and LKr, probably due to the larger potential well.

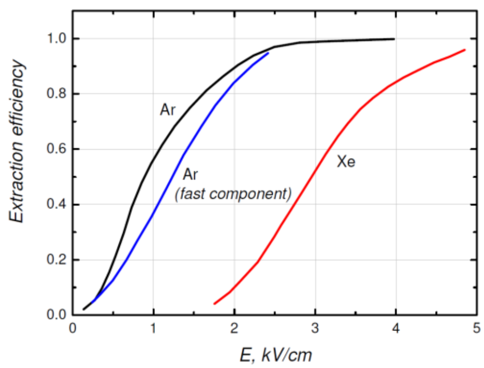

Figure 1 Extraction efficiency of electrons from the liquid phase into the vapor above it, as function of the electric field in the liquid. Figure taken from [3].

4.5 Electroluminescence

Once electrons have crossed the interface into the gas phase, electroluminescence (EL) can occur in the gas phase, under appropriate field intensity. In order for the EL to occur, electrons accelerating under the influence of the electric field need to accumulate enough energy between consecutive collisions with the gas atoms to excite the atom they collide onto. EL occurs above threshold field values; the threshold depends on the gas and on its pressure (or density); the photon yield, i.e. the number of photons emitted (to 4π) per unit drift length is given by the following formula [3]:

$$\frac{dN_{ph}}{dx} = \alpha E - \beta P - \gamma$$

Where E is the electric field, P is the pressure and the parameters α, β, γ depend on the gas and are given in Table 3 below.

Table 3 EL parameters for Xe and Ar vapor. From [3].

Parameter	Ar	Xe
$\alpha\,[V^{-1}]$	0.0819	0.137
$\beta[bar^{-1} \cdot cm^{-1}]$	139	177
$\gamma[cm^{-1}]$	30.6	45.7

The EL process is linear with the electric field; the threshold value (E_{th}) can be computed by solving the equation:

$$0 = \frac{dN_{ph}}{dx} \qquad \textit{Eqn. 2}$$

The total EL yield is then given by the integrating:

$$\int \frac{dN_{ph}}{dx} \cdot dl \qquad \textit{Eqn. 3}$$

along the trajectory of the electrons, and is valid only where the electric field is larger than the threshold field.

4.6 Detection technologies

There are many existing technologies for the detection of the scintillation signals. Most common today are the vacuum photomultiplier tubes (PMT) [3] and solid-state based multi-pixel photon counter (MPPC, also referred to as silicon photomultiplier – SiPM) [29]. Both technologies offer single photon sensitivity with high photon detection efficiency. Other existing technologies are the avalanche photodiodes (APD) [30] and the cryogenic gaseous photomultiplier (GPM) [31, 32], which has been under development in recent years in our group.

A few types of particle detection schemes are currently in use. The *single-phase scintillation-only* detectors, apply no electric field and record only the scintillation signal. An example for such an experiment is the MEG calorimeter searching for the non-standard model process $\mu \to e\gamma$ [7]. While this scheme offers a simple and readily scalable design, it cannot provide accurate topological information about event position, multiple-scattering events, or about the structure of charge particle tracks. This additional (and sometimes vital) layer of information can be obtained, however, in detectors employing a TPC as discussed above.

In a *single-phase TPC* (depicted in Figure 2, left), when an electric field is applied, the ionization electrons that have escaped recombination at the interaction location drift towards charge readout planes. The simplest form uses two parallel planes of wires for charge readout, one behind the other, and at an angle to each other. The charge is drifted towards the last plane (the “charge collection plane”), while, when traversing the first one, it induces a charge signal on it (“induction plane”). The XY position is reconstructed according to the charge signal on the two wire planes. The Z coordinate is determined from the time difference between the primary scintillation signal and the charge signal (referred to as “S2” signal). This is the scheme used, e.g., in the ICARUS experiment [6] and in the MicroBooNE experiment [33] and is planned for the first two modules of the future DUNE neutrino observatory [14] where a full interaction products characterization and calorimetry is required.

While in energetic neutrino experiments the charge signals are large (e.g. for a minimally ionizing particle in LAr, at 0.5 kV/cm, the liberated charge is ~5,000 e^{-}/mm [6]), in other experiments, e.g. in DM searches, the deposited energy is in the keV scale, meaning that only few electrons are eventually detectable. The main limit to the *single-phase TP*C as described is the large amount of charge needed to overcome the electronic noise of a readout channel. This problem is alleviated in the *dual-phase TPC* scheme, like the ones employed in DM searches (see Figure 2, middle) such as XENON1T [13] and LUX [34]. The free electrons drift towards the gaseous phase above the liquid. They are consequentially extracted in a high field region into the vapor phase, where they induce a secondary electroluminescence (EL) light signal ("S2" signal) [2, 3]. The XY position of the event is reconstructed according to the hit pattern on the top array of photosensors; the Z coordinate is calculated using the time difference between the S1 and the S2 signals. Current DM experiments employing the dual-phase technique are XENON1T [13], LUX [34] and Panda-X [35] using liquid xenon (LXe), and ArDM [23] and DarkSide [36] using liquid argon (LAr).

A second concept of a dual-phase detector uses charge amplification in the vapor phase (see Figure 2, right). An example for this is the WA105 technology demonstrator [37] investigating prototypes for future neutrino experiments. Charge extracted into the gaseous phase undergoes avalanche multiplication in a Large Electron Multiplier (LEM), a structure identical to a Thick Gas Electron Multiplier (THGEM) discussed below [38], recorded using position sensitive charge readout electronics. Such gain, may allow for better S/N in the readout electronics and therefore will allow for a longer drift of the electrons, lower price for the electronics and higher sensitivities to low energy events (e.g. Supernovae neutrinos) [37]. The charge signals can also be detected optically, by recording avalanche photons with appropriate photosensors [39].

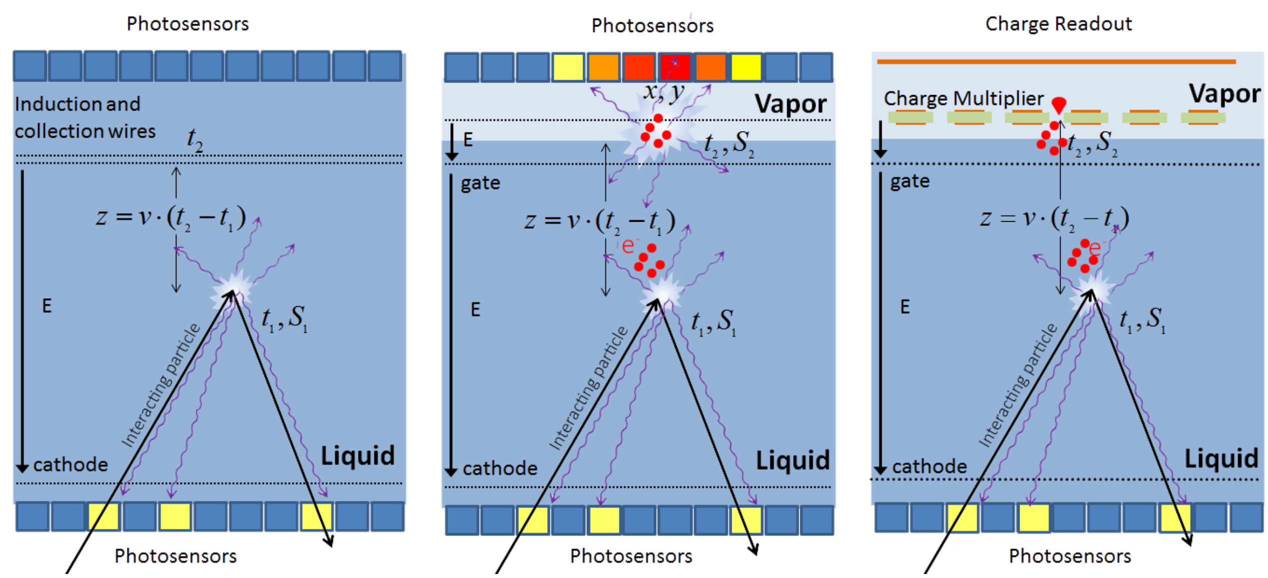

Figure 2 Left: Conceptual demonstration of the operation principle of a single-phase TPC. Particles interacting in the detector leave a cloud of ionization and excitation in the liquid. The deexcitation induces primary scintillation photons recorded on two arrays of photosensors at the top and at the bottom of the cryostat. The remaining electrons, drift upwards to two wire planes. When the charge drifts across the first plane (called "induction plane"), it induces a signal on the wires. The charge is then collected on the second wire plane ("collection plane") inducing a second charge signal. The planes are inclined at angle such that a full XY reconstruction of the event is possible. The Z coordinate is reconstructed according to the time difference between the primary scintillation and the charge signal. Middle: operating principle of a dual-phase TPC. Primary scintillation is read on two arrays of photosensors (top and bottom of cryostat). The charge is drifted towards the gaseous phase. It is extracted into the vapor using a high electric field where it induces an EL signal read out using mainly the top array of photosensors. XY position is reconstructed according to the hit pattern on the top array and the depth is reconstructed according to the time difference of the two signals. Right: operation principle of a dual phase TPC with charge amplification and readout in the vapor phase.

4.7 Next generation detectors

Scaling up of the detector size, although a well-motivated natural step-forwards from the physics point of view, poses technological challenges from the points of view of construction, reliable operation and signal readout [14, 22]. Specifically, scaling up detector size necessarily causes a reduction in the detectable radiation-induced scintillation-light and charge signals, causes an increase in intrinsic noise of the readout thus affecting the signal-to-noise ratio. Combining these with the cost of today's state of the art ultra-sensitive light sensors and low noise charge readout, one is highly motivated to look for new solutions and concepts for future large-scale experiments.

Weizmann Institute scientists are members of today's largest LXe-based DM experiment XENON1T [13] and XENONnT [40]. Our group is involved in DARWIN, the next-generation ultimate dark matter observatory; it is planned to employ a 50 tons dual-phase LXe TPC [22]. While the baseline readout of DARWIN relies on vacuum PMTs, other readout solutions are currently evaluated, among them SiPMs [41], CMOS sensors [42], large-area Abalone hybrid vacuum photosensors [43] and our Liquid Hole Multipliers (LHM) concept [22]. Future Liquid Argon (LAr) based neutrino experiments are planned to reach 150 kton target with the Deep Underground Neutrino Observatory (DUNE collaboration) [14]. The DUNE baseline design incorporates single-phase TPC with wire readout; the third TPC is foreseen to employ the dual-phase technology with a LEM based readout [44]. Other, newer technologies will be considered for the remaining module.

This Ph.D. work focuses on the R&D of a novel ideas for charge and light detection in future large volume noble liquid detectors. The Liquid Hole Multipliers (LHM) offer a solution for a combined detection of scintillation light and ionization charge in a single module immersed in the noble liquid. Though the R&D is still generic, the work was originally motivated by future large volume LXe based detectors for multi-ton dark matter searches and is carried out under the framework of the DARWIN collaboration [22]. In addition, during the course of this period, some work was also done towards demonstrating the operation of a cryogenic Resistive-Plate WELL (RPWELL) [31] detector, proposed as a possible solution for stable, enhanced avalanche-gain charge readout in future large volume dual-phase argon TPC detectors for neutrino experiments. The work on this project was very limited mainly due to the difficulty in finding material with suitable resistivity at cryogenic temperature, which is in the heart of the RPWELL detector. The work done in this context is therefore documented as an appendix to this thesis. Though not complete, it will, hopefully, serve as a first step for future investigation in this direction.

4.8 The Liquid-Hole Multiplier (LHM) project

The bubble-assisted LHM is a recent concept, proposed for the combined detection of ionization electrons and primary scintillation photons generated along charged-particle tracks in noble liquids [45-48]. A conceptual scheme of an LHM module is depicted in Figure 3. It consists of a perforated electrode, e.g., a gas electron multiplier (GEM) [49], or a thick gas electron multiplier (THGEM) [50] immersed inside the noble liquid, with a bubble of the noble gas trapped underneath. The top surface of the electrode is optionally coated with a VUV-sensitive photocathode such as cesium iodide (CsI) [51]. Heating elements (such as a plane of resistive wires) below the electrode generate the bubble on-demand. Once formed, the bubble fills the space below the electrode and remains stable as long as the system is in thermodynamic steady state, with buoyancy pushing it upward and surrounding walls confining it from its sides. The top and bottom surfaces of the electrode, as well as the heating wires, are held at different potentials, creating a dipole-like field in the electrode's holes and a transfer field between the electrode bottom and the wire plane. The drift field above the electrode is set by the potential difference between the top surface of the electrode and a distant drift electrode (cathode plane) above.

Particle interactions in the liquid lead to a prompt VUV scintillation signal (S1) and to the release of ionization electrons. These drift towards the LHM and are focused by the local field into its holes. Once they cross the liquid-gas interface into the bubble, they induce EL light (S2) in the gas, in the high-field region close to the bottom of the hole. Similarly, S1 photons impinging on the photocathode release photoelectrons (PEs); these are focused into the LHM holes, inducing an EL signal (S1') shortly after S1 (and typically long before S2). The S1' and S2 EL signals can be recorded by a position-sensitive photon detector (e.g., a Silicon Photomultipliers, SiPM, array) located below the electrode.

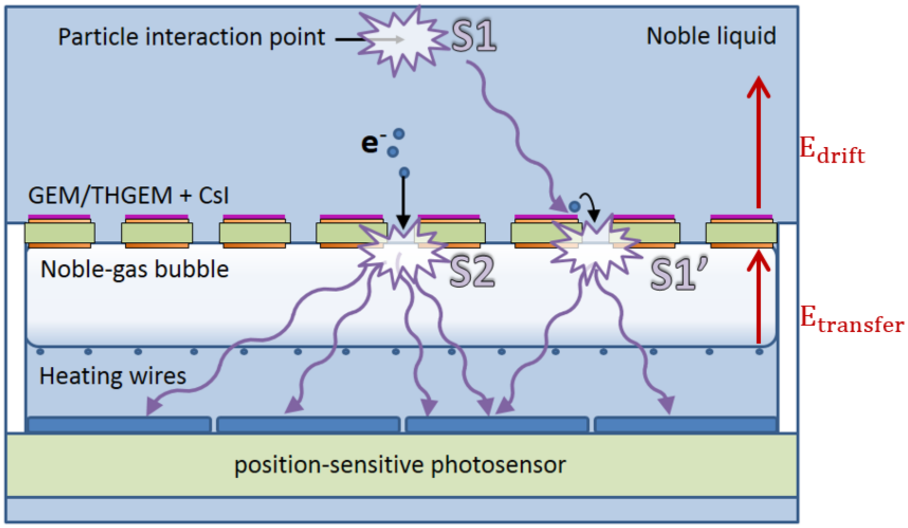

Figure 3 Conceptual scheme for an LHM module, comprising a perforated electrode (e.g., GEM or THGEM) coated on top with a photocathode (e.g., CsI), a grid of heating wires for forming the bubble and a position-sensitive photon detector below. The bubble is supported by buoyancy against the bottom of the electrode. Ionization electrons focused into the holes create EL light (S2) once they cross the liquid-gas interface into the bubble. Primary VUV scintillation (S1) photons impinging on the photocathode release photoelectrons which are focused into the holes and create similar EL signals (S1'). The lateral coordinates of the S2 and S1' signals are reconstructed by the position-sensitive photon detector.

Previous works performed with a configuration similar to that shown in Figure 3 demonstrated the idea, using GEM and THGEM electrodes immersed in liquid xenon (LXe), with alpha-particle tracks providing primary scintillation light and ionization electrons. It was shown that bubbles can indeed be formed on-demand by Ohmic heating and that once formed, they remain stable as long as the system stays in a thermodynamic steady state.

This research work aimed at deeper understanding the properties of the bubble-assisted LHM detector. The experimental work carried out in a dedicated LXe cryostat, accompanied by computer simulations, may shed light on some of the aspects that could become crucial for future experiments incorporating LHM detectors. A full report of the work done during the Ph.D. period is presented in the following chapters of this thesis. Every chapter is followed by a small discussion of the results and, then, finally, a discussion merging all the data and providing outlook for the project.

5 Research overview

During this thesis period, the research performed on the bubble-assisted LHM can be coarsely divided into six subchapters, each looking into a different aspect of the study of this novel detector concept. Except for the first demonstration of LHM operating in LAr, most of the work was done in LXe. The subchapters, as listed below, are discussed separately and integrated at the end to establish a complete body of work - with a full discussion of future work to be done beyond the scope of this thesis.

Comparative study of LHM electrodes (chapter 6.1)

This chapter first presents the concept of the LHM in detail, including the experimental setups, methodologies and analysis techniques. It outlines in detail the procedures developed for a successful operation of an LHM prototype. Then it outlines a long study done, with alpha particles, investigating different electrode structures (differing in geometry, dimensions and materials) operated as LHM elements in LXe. The analysis focuses on radiation-induced light yields and energy resolution of the different electrode structures, their timing properties and the relative photon detection efficiency. The purpose of the study is double, first to 'blindly' scan for electrodes yielding superior physical properties, and second to use the differences among them to provide a glimpse into the physics processes governing the performance of the detector.

Study of photon detection efficiency of LHM (chapter 6.2)

Since the LHM coated with a photocathode is a photon detector with potential use in experiments requiring single-photon detection, it is of utmost importance to establish its photon detection efficiency (PDE) for scintillation light. The study here included establishing the effective quantum efficiency (QE_{eff}) of a UV-sensitive CsI photocathode immersed in LXe, followed by an estimation of the expected PDE of an LHM element (15-20% depending on the electrode). Then, the PDE was directly measured using a single-photon source (PDE=2-4% depending on electrode). The discrepancy between the two values and its possible origins are discussed in length.

Position reconstruction (chapter 6.3)

Many of the experiments using noble-liquid media operate the detectors in a TPC mode. This requires establishing an X-Y position sensitive readout system for the LHM light output. The work on position-sensitive readout started with a self-written Matlab-based toy Monte Carlo simulation code. It was followed by imaging of an ^{241}Am alpha source in a THGEM-based LHM in LXe, using a quad-SiPM readout system and a simple center-of-gravity position reconstruction technique. The scalability of this technique, a discussion of its limitations and suggestions for future improvements and studies are discussed.

First proof of LHM operation in LAr (chapter 6.5)

Here, we present a first proof of a bubble-assisted LHM operation in LAr. The first demonstration was done only for charge readout (i.e. without a CsI photocathode) using a THGEM electrode. The chapter includes study of pulse shape, energy resolution and a first demonstration of imaging. It also discusses the differences between LXe- and LAr-based LHM detectors properties.

Double stage LHM (chapters 6.6)

The double-stage LHM consists of two independent LHM detectors one on top of the other, each electrodes with its heating wires below and its bubble. The bottom element is coated with a CsI photocathode. The top element was not coated with CsI in this set of experiments. VUV photons from the EL generated by the top electrode extract photoelectrons from the bottom photocathode, generating EL in the second electrode. The structure has so far not shown any improvement compared to a single-stage LHM.

Other ideas for bubble confinement (chapters 6.7 and 6.8)

In a more general sense, the novelty of the LHM is the encapsulation of a gas bubble inside the liquid volume. The two concepts presented here, take this concept in two different directions. First, the vertical LHM is the attempt to generate a bubble between a vertically oriented hole-electrode and a wall on the other end. Second, trapping of a gas bubble between two meshes, thus generating in practice a parallel plate detector. The studies of both concepts did not mature enough, but have helped shedding light onto some aspects of the bubble confinement and electron transmission.

6 Summary of main results

6.1 Comparative study of different LHM electrodes

In the current study, we have focused on investigating the light yield (number of photons per ionization electrons drifting towards the electrode), energy resolution, relative photon detection efficiency (PDE) and timing resolution of LHM elements. Different types and sizes of electrodes were investigated in our MiniX LXe cryostat - in an identical setup; all have undergone similar treatments and procedures. In particular, careful attention was made to create high-vacuum conditions prior to Xe filling and to maintain high gas purity. Most of the results shown here have been published in [52]. The procedures discussed here have become the “standard guideline” for assembly and operation of an LHM prototype.

6.1.1 Experimental setup and procedures

The experiments were conducted in a dedicated LXe cryostat designed and assembled by me, the Mini Xenon apparatus (MiniX), described in detail in [53] (see scheme in Figure 4). It comprises a 100 mm-diameter, 100 mm-tall cylindrical LXe volume filled with ~250 ml of LXe. The rest of the volume is equipped with instrumentation and PTFE holders and spacers. The detector assemblies are suspended from the topmost flange. The cryostat has a window which allows viewing the detector from below at 60° with respect to the vertical axis. A camera (CALTEX intruments VIP-50-HD60) is attached in front of the window to enable observation of the bubble formation and dynamic.

Xenon liquefaction is done on the LN_2-cooled cryostat wall. During operation, Xe is continuously circulated through an SAES hot getter at ~1.5 standard liters per minute. Before mounting detector assemblies incorporating CsI photocathodes, the cryostat was pumped down to high vacuum using a turbo-molecular pump and a LN_2-cooled cold finger to reach a water partial pressure below 10^{-6} mbar (verified using a residual gas analyzer). Assembly of the detector setups in the cryostat was done under constant Ar flushing, to minimize water contamination. Subsequent steps included pumping down the cryostat overnight, filling pure Xe gas at ~2.5 bar, circulating the gas through the SAES purifier (SAES MonoTorr PS3-MT3-R/N) for 1-2 days, cooling down, further filling of gas under Xe liquefaction, thermal stabilization (~12 hours), circulation of the liquid through SAES purifier for at least two days and bubble formation by Ohmic heating of a wire-grid. Measurements were normally conducted at a liquid temperature of 173 K, corresponding to the vapor pressure of 1.6 bar. For each investigated configuration, measurements were carried out over several days. For most setups, the measurement taken two days after liquefaction was repeated at the end of the data taking series (few days), making sure that the liquid purity (and other parameters such as PMT response) have not changed during the data taking period.

Four different LHM electrodes were investigated: a THGEM, a standard GEM with bi-conical holes and two single-conical GEM electrodes (SC-GEM) of different thicknesses [54]. The Cu surfaces of all electrodes were Au-plated. The geometrical properties of the investigated electrodes are listed in Table 1, and 3D models of their respective unit cells are shown in Figure 5. The four electrodes were measured in series, the THGEM being the first. In order to gain the confidence in the stability of the system (in terms of PMT responses, gas purity etc.), the THGEM measurements was repeated at the end, after all other electrodes have been measured. No significant change was observed.

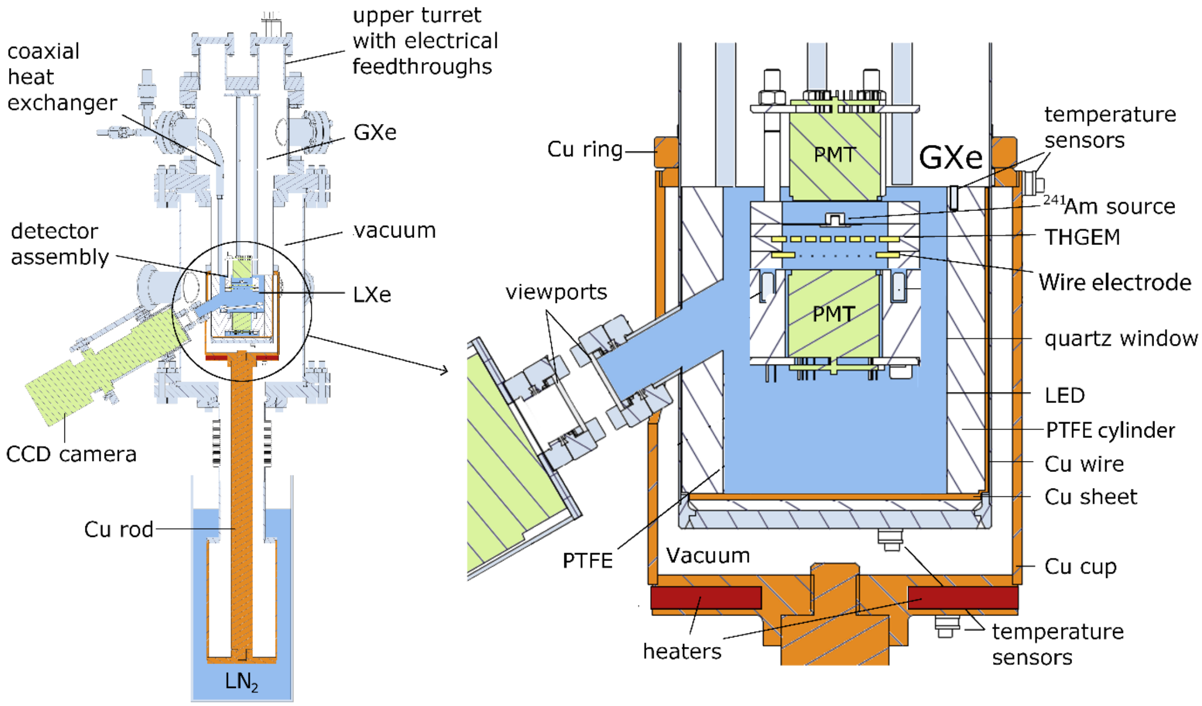

Figure 4 Schematic drawing of the MiniX cryostat.

A 300 nm-thick CsI layer was vacuum-deposited on the top surface of each electrode investigated, for the study of UV-photon detection (the SC-GEM was CsI-coated on the side with the smaller holes). The CsI-coated electrodes were transferred in dry N_2 from the deposition chamber into a dry N_2 filled glove box for assembling the detector setup (~1h assembly time), which was then quickly transferred (~20 s in ambient air) into the Ar-flushed cryostat (argon purity of 99.97%). The measured quantum efficiency (QE) value of all photocathodes investigated was in the range of 18-23% at 175 nm in vacuum; the relative loss in QE during transfer to the N_2-box and to the cryostat was measured to be below 10%.

Table 4 Specifications of the three electrodes used in this study.

	THGEM	Standard GEM	Single-conical GEM	Single-conical GEM
Insulator	FR4	Polyimide (Kapton®)	Polyimide (Kapton®)	Polyimide (Kapton®)
Thickness	0.4 mm	50 μm	50 μm	125 μm
Hole diameter(s)	0.3 mm	top/mid/bottom 70/50/70 μm	top/bottom 300/340 μm	top/bottom 300/400 μm
Hole pitch	0.7 mm	140 μm	600 μm	600 μm
Cu thickness	20 μm	5 μm	5 μm	5 μm
Hole rim	50 μm	none	none	none

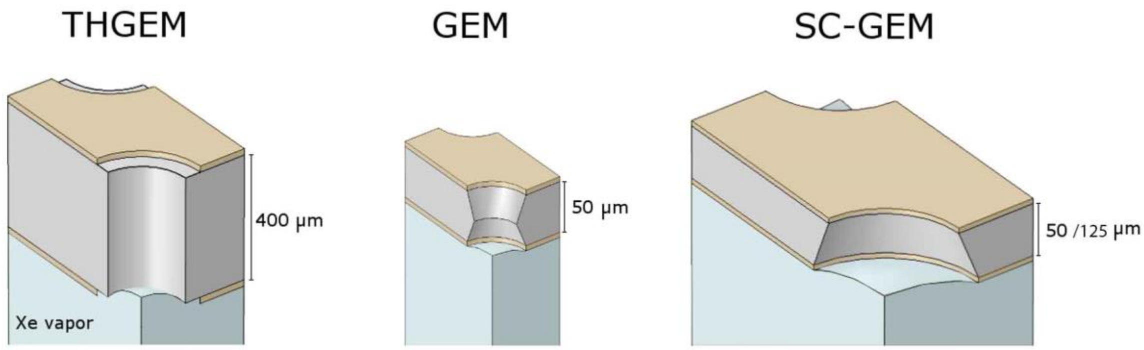

Figure 5 3D models of unit cells of the three LHM electrodes used in the experiments and in the accompanying simulations. The electrodes are immersed in LXe; the region below each electrode (in light blue) is Xe vapor, with a liquid-gas spherical interface penetrating into the holes. Note the different scale for the THGEM compared to the GEM and SC-GEM.

The detector assembly (Figure 6) comprised the CsI-coated LHM electrode, a spectroscopic ~180 Bq, 4 mm diameter ^{241}Am alpha-particle source located 7.9 mm above it, a field-shaping ring between the electrode and the source and a resistive-wire plane underneath. The field-shaping ring (inner diameter 20 mm) was introduced for creating a fairly uniform field across the central region of the photocathode, without the need for an intermediate mesh (the latter would have resulted in partial blocking of the drifting ionization electrons, or alternatively require an intense field between the mesh and electrode, thus interfering with photoelectron extraction from the photocathode). The potentials on the source, field shaping ring and the top of the electrode where calculated using COMSOL Multypysics® [55]. The active (perforated and CsI-coated) area of the GEM and SC-GEM was 14 mm in diameter; for the THGEM the active CsI area was 20 mm in diameter. The resistive-wire plane, located 1.6 mm below the electrodes, served two purposes: (1) allow for bubble formation by Ohmic heating, and (2) set the value and direction of the transfer field (E_t) below the electrode (allowing to either pull the electrons through the bubble or push them towards the electrode bottom); as discussed below, the transfer field can also serve to amplify the EL light by a large factor. Once formed, the bubble extended from the electrode bottom to the wires, filling a 30 mm-diameter region, as shown schematically in Figure 6.

Light signals were recorded by two Hamamatsu R8520 photomultiplier tubes (PMTs). The top PMT recorded S1 photons reflected off the PTFE ring and served as the trigger. The PMTs were operated mostly at -600V (lower than their recommended operating voltage of -800V) to avoid saturation of the electronics. At high voltages on the detectors, the resulting pulses were large enough to saturate the PMT readout. These high pulses were recorded at lower PMT voltages. Measurements taken at lower PMT voltages were then scaled to match the PMT gain of -600V and presented on the same figure. Readout of the S1 photons passing through the electrode's holes, as well as of the S1' and S2 EL signals, was done by passing the bottom PMT signal through a Phillips 777 linear amplifier (set to minimal gain of 1.8) and then digitized using a Tektronix MSO5204B oscilloscope. The digitized waveforms were post-processed using dedicated Matlab scripts.

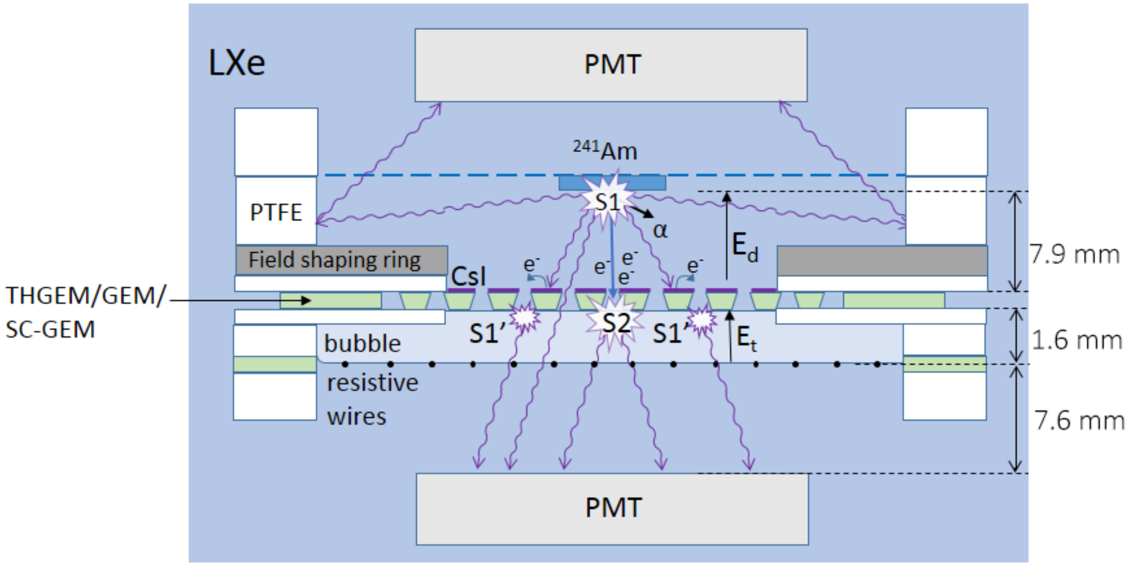

Figure 6 Schematic setup for the comparison between the THGEM, GEM and SC-GEM (shown here as an example) electrodes as horizontal bubble-assisted LHM elements; dimensions not to scale.

6.1.2 Results

6.1.2.1 Bubble formation and dynamics

The images presented in Figure 7 were taken with the camera looking at the bottom part of the LHM, equipped with a THGEM electrode. The detector assembly was very similar to the one shown in Figure 4 or Figure 6 except for the bottom PMT being placed at a larger distance from the detector assembly, enabling the full view of the bottom part of the THGEM. Figure 7A presents the view of the bottom part of the THGEM and the heating wires below it, without a bubble and with the heating wires turned off. Figure 7B presents small-bubbles formation with current passing through the heating wire (in this particular setup, current was passed only through the middle wire). The heating of the wires causes bubble to form, to travel upwards and to be stopped on the bottom face of the THGEM where they coalesce into a larger "macroscopic" bubble. Figure 7C is the result of stopping the heating before the bubble has managed to grow enough to cover the entire surface of the electrode. Figure 7D is a full bubble covering the entire surface of the electrode. One can clearly observe both the heating wires and their reflection due to total internal reflection at the liquid-to-gas interface.

Upon formation of the bubble under the THGEM electrode, the heating wires are turned off and the bubble is left to stabilize for 2-3 hours. During this time, it "breathes" up and down, covering and uncovering the heating wires in few-seconds period. Finally the bubble remains stable with only very small remaining "breathing" (i.e. up and down motion of the bottom interface), estimated by eye to be a fraction of a mm in magnitude. The breathing is probably due to small pressure fluctuation, and it exists with and without recirculation of the liquid. The bubble, with its small breathing movement, remains stable for the rest of the time. The longest time we held a bubble was 10 days, before the cryostat had to be freed for a different experiment. We therefore expect that a bubble could remain stable (under given operational conditions) for unlimited period.

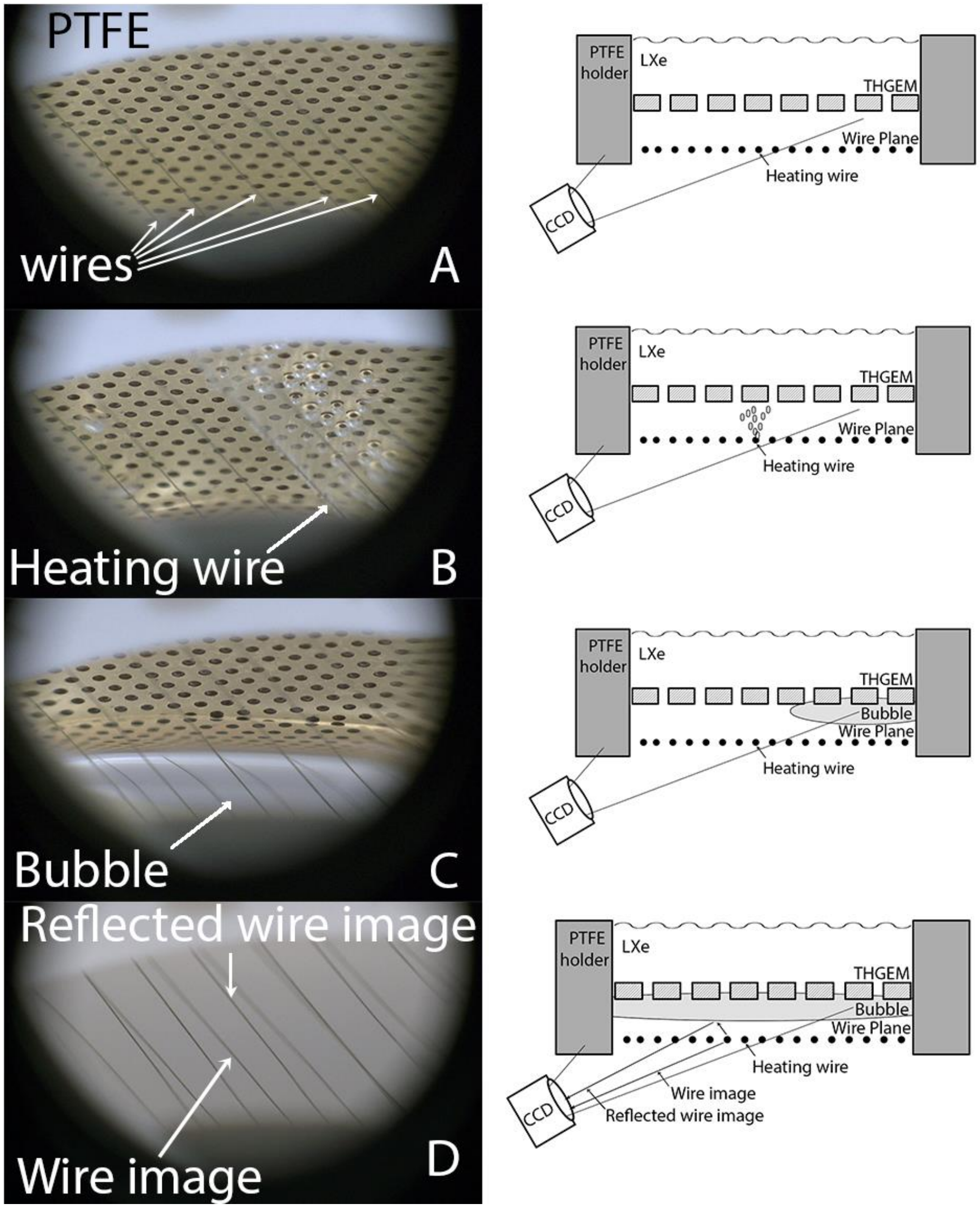

Figure 7 Typical images recorded by the camera: (A) without bubble, heating wires "off" (B) with the heating wires "on", bubbles start to form and coalesce into a larger bubble at the surface of the THGEM. (C) A bubble covering a fraction of the THGEM bottom surface, heating wires "off" (D) A bubble covering the entire surface of the electrode. One can observe the image of the wires as well as their total internal reflection from the liquid-to-gas interface.

6.1.2.2 EL from ionization charges and photoelectrons

6.1.2.2.1 Pulse shapes and energy spectra

As discussed above and shown schematically in Figure 6, for the CsI-coated LHM electrodes the waveform recorded by the bottom PMT, for each alpha particle emitted into the liquid, comprises three signals: (1) primary-scintillation light passing through the electrode holes (S1, green in Figure 8); (2) EL light generated inside the bubble by photoelectrons extracted from CsI following the absorption of primary scintillation photons in it (S1', red in Figure 8), and (3) EL light generated inside the bubble by ionization electrons liberated along the alpha-particle track, which drift towards the LHM and are focused into its holes – inducing EL in the bubble (S2, black in Figure 8). The nominal drift field in Figure 8 was $\mathrm{E_d} = 0.5\ \mathrm{kV/cm}$ for all electrodes and transfer field of $E_t = -1\ \mathrm{kV/cm}$. Note that the transfer field values in this work are quoted as if the gap between the electrode and the resistive-wire plane is a parallel plate. This however is only indicative as the wires are spaced 2 mm apart and the gap is only 1.6 mm.

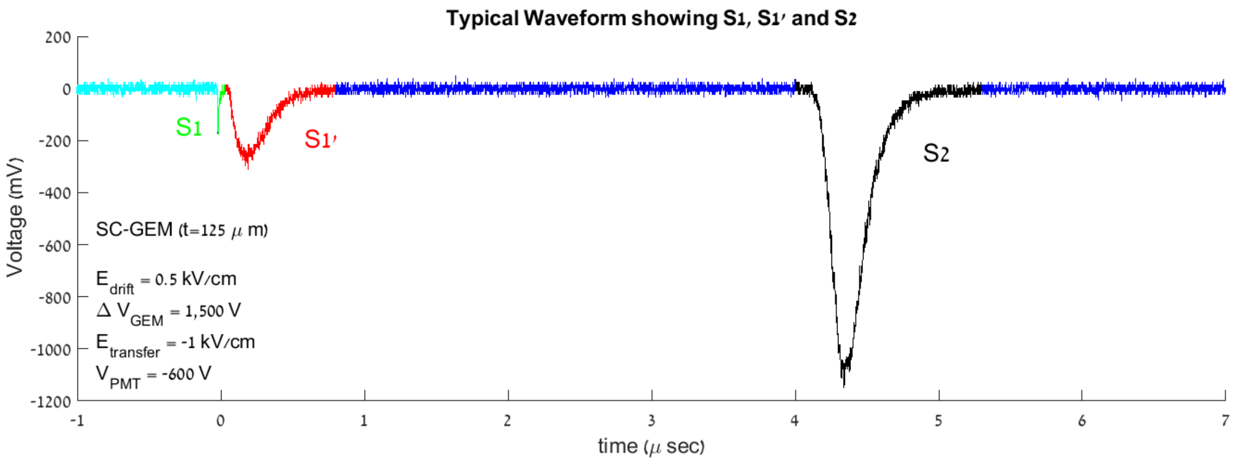

Figure 8 Sample waveform in a SC-GEM in LXe, showing three signals: the prompt scintillation signal (S1, green), the photoelectron-induced EL signals from CsI (S1', red) and the ionization- charge-induced EL signal (S2, black).

For given drift- and transfer fields, the voltage across the electrode was varied gradually, with typically 10,000 waveforms recorded at each voltage step. The integrated pulse area under S2 and S1' was computed for each waveform, serving to build a histogram of pulse areas for each voltage setting. For the amount of charge generating S1' and S2, the pulse area is a more precise measure as opposed to the pulse height as the former is insensitive to the pulse shape. This enables a direct comparison S1' and S2 areas without the need to correct for different pulse shapes. Also, since photoemission is a stochastic process, the pulse height is much more sensitive to fluctuation while the pulse area reduces this effect by averaging over the entire period of the pulse. A Gaussian fit was applied to each histogram, giving the mean E and standard deviation σ of the S2 and S1' distributions. Histograms for the S1' and S2 signals of the 125 µm thick SC-GEM, taken under the voltage configurations which yielded the best RMS resolutions, are shown in Figure 9. The Gaussian fit to both distributions was applied over the range starting one standard deviation to the left of the peak and ending four standard deviation to its right; it was done to exclude the low-amplitude contribution of events in which part of the alpha-particle energy was deposited inside the source substrate. When fitting the S2 data we also excluded the 'hump' on the right side of the peak, resulting from coincident emissions of alpha particles and 59.5 keV gamma rays from ^{241}Am. The best resulting RMS values for S2 and S1' were 5.5% and 6.5%, respectively.

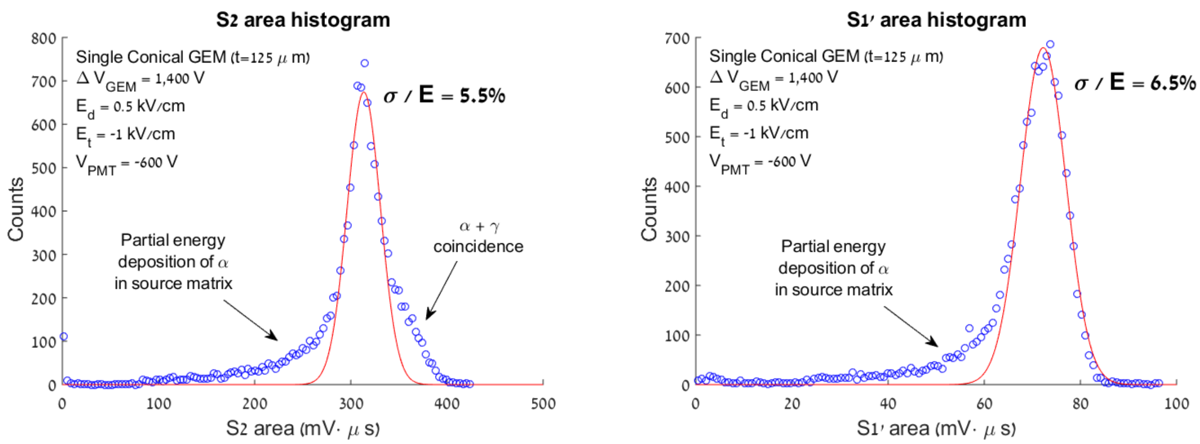

Figure 9 Spectra of S2 (left) and S1' (right) from a single-conical GEM biased to 1,400 V.

6.1.2.2.2 EL dependence on electrode voltage

Figure 10 shows the mean magnitude E (integrated pulse area) of S2 and S1' as a function of the voltage across the four investigated electrodes, for the above nominal drift- and transfer fields. The data in Figure 10 is given in 'raw form' on the left horizontal axis, i.e., as the measured pulse areas. Estimates of the corresponding effective EL yields of the four electrodes (number of EL photons per electron entering the electrode holes, emitted over 4π) are discussed below in the next section. The 125µm SC-GEM showed saturation in S2 signal starting from ~1,800V across the electrode (seen as a slight jump in the S2 signal magnitude). Therefore, Starting from 1,900V, data was acquired with $V_{PMT} = -550V$ and a scaling correction factor was applied according to the ratio of S1' pulse recorded at either voltages.

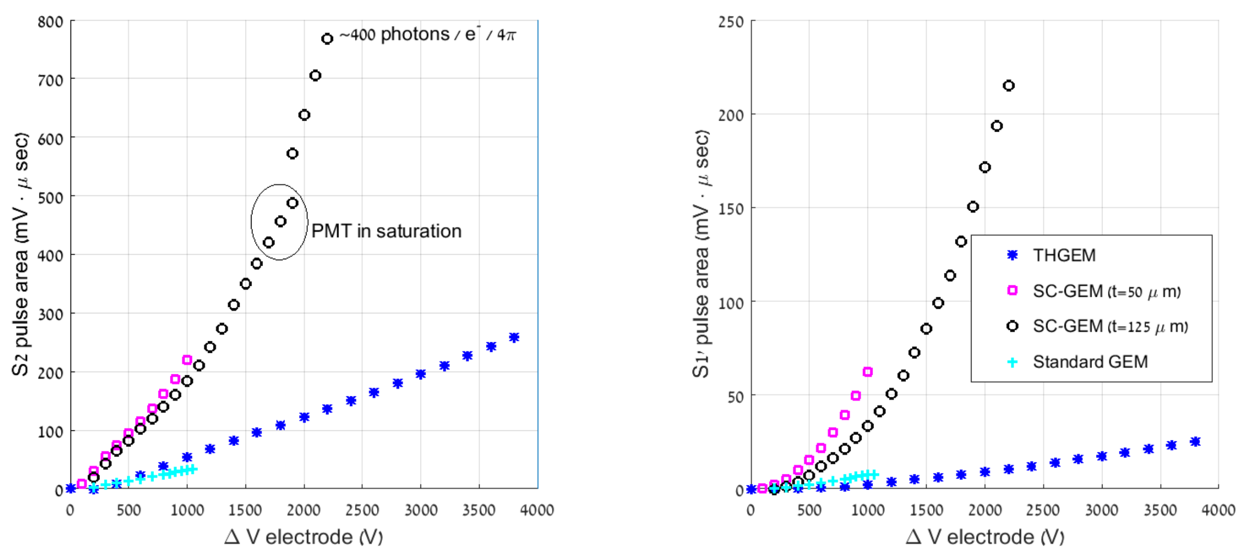

Figure 10 S2 and S1' signal amplitudes vs the voltage difference across the electrodes. Data was recorded at $E_d = 0.5\ kV/cm$, $E_t = -1kV/cm$ and $V_{PMT} = -600\ V$. The effective light yield is computed according to the methods described in the sections below.

At a given voltage, S2 magnitude is the largest for the thick SC-GEM: up to ~5 times larger than for the standard GEM (at the highest applicable voltage) and the THGEM. The maximal S2 value for the THGEM is similar to that of the thin SC-GEM, and is reached at roughly 3.5 higher voltages. The deviation from linearity starting at ~1kV for the thick SC-GEM (not visible for the other electrodes) is attributed to small avalanche multiplication within the bubble. It reaches an estimated maximum value of ~1.8 at 2200 V (by comparing the measured curve to a linear extrapolation from lower voltages).

The measured S1' signal is also the largest for the 125 µm SC-GEM: up to ~10 times larger than for the THGEM, at the same applied voltage. The maximal value of the SC-GEM S1' is ~5 times larger than that of the THGEM. For the S1' curves, the departure from linearity is attributed to two effects: small avalanche multiplication (similar to the effect seen in S2) and an increase in the field on the surface of the CsI photocathode, leading to a higher overall photoelectron extraction efficiency into the liquid (as in [56] and in chapter 6.2.3). The much larger measured value of S1' for the 125 µm SC-GEM compared to the THGEM is attributed to the higher surface field of the former (as verified by COMSOL calculations). This effect is also clearly visible as discussed in chapter 6.2.5.

When analyzing the difference in light yields between the electrodes, one should also explore the effect of electron diffusion. For smallest geometry, namely for a GEM, a fraction of the electrons (either ionization electrons or photoelectrons) could be lost by transverse diffusion to the hole's insulating walls. However, had this been the major factor in explaining the difference between the S2 response of a GEM and the SC-GEMs, then it is not consistent with the GEM and THGEM showing similar S2 response.

Note that in light of the low alpha-particle emission rate (~90 Hz) and the fact that the number of participating holes is 1-2 orders of magnitude larger than the number of photoelectrons per event (e.g., for the GEM the active area contains ~40,000 holes, while the number of PEs per event is ~1000), charging up effects during typical measurements lasting 1-2 hours should be minimal and can be neglected. Furthermore, measurements of S1' signals over ~12 days showed no reduction is signal magnitude (it did show ~10% increase of signal magnitude, probably due to cleaning of the liquid during this period).

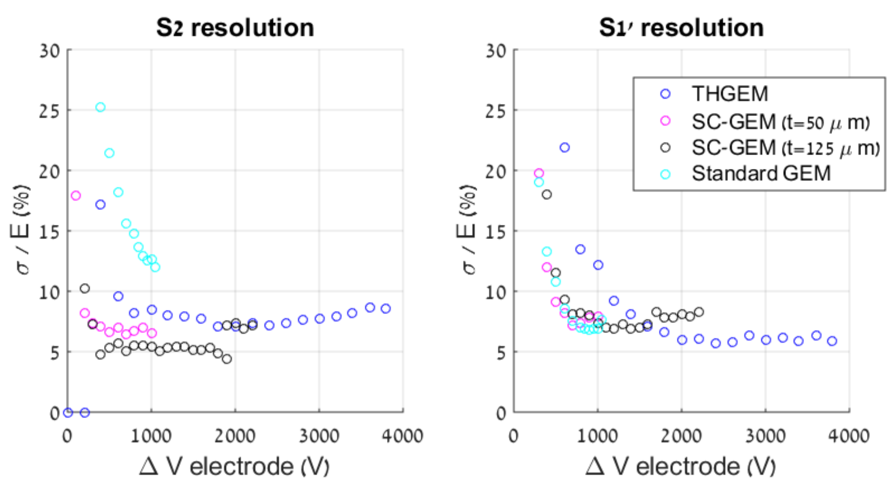

Figure 11 S2 and S1' resolutions vs the voltage difference across the electrodes. Data was recorded, for all 4 electrodes shown, at $E_d = 0.5\ kV/cm$, $E_t = -1kV/cm$ and $V_{PMT} = -600\ V$. The sudden degradation of the resolution at 1,900V in the thick SC-GEM is due to change in the PMT voltage.

The RMS resolution σ/E of S2 and S1' magnitude (pulse area) as a function of the voltage across the electrode is shown in Figure 11 for a drift field of 0.5 kV/cm. The PMT voltage was -600 V except for the 125 µm thick SC-GEM, where above 1,900V the PMT voltage was reduced to -550V resulting in a slight degradation of the energy resolution of the PMT. Initially the resolution improves as a function of the voltage, indicating a larger number of collected electrons into the holes. The best S2 resolution is ~5.5% RMS for the thick SC-GEM. The best S1' resolution is also obtained for the thick SC-GEM ~6.5% RMS. Note that the expected resolution just from Poisson statistics on the number of free primary electrons (without instrument effects) is $1/\sqrt{6{,}800} = 1.2\%$.

6.1.2.2.3 Timing properties

The timing properties of the electrodes was estimated by digitally applying a constant fraction discrimination procedure. This was done by integrating the S1' pulse and then numerically searching for the time point at which 30% of the integration is reached. The threshold value of 30% was chosen since the timing properties showed only few percent jitter when applying thresholds between 20% and 50%. A histogram of all time points from all waveforms was plotted and a Gaussian fit was applied. Figure 12 presents the standard deviation of this distribution for the different electrodes. When looking at the figure, one clearly observes two effects. First, the larger the pulse, the better the timing resolution. This is expected as higher photon emission smoothens the integral of the pulse (smaller deviations due to better statistics of the light emission) and therefore results in a more accurate timing result. Second, the timing properties is correlated with the hole size and spacing. The larger they are, the wider the spread in time of arrival of the electrons from the electrode to the bubble, resulting in a larger time spread. Eventually, the timing properties are theoretically limited by the number of photoelectrons and the fact that different photoelectrons are extracted from different places on the PC and thus have different trajectory lengths before generating EL. We therefore expect the timing resolution to saturate at large enough EL signals.

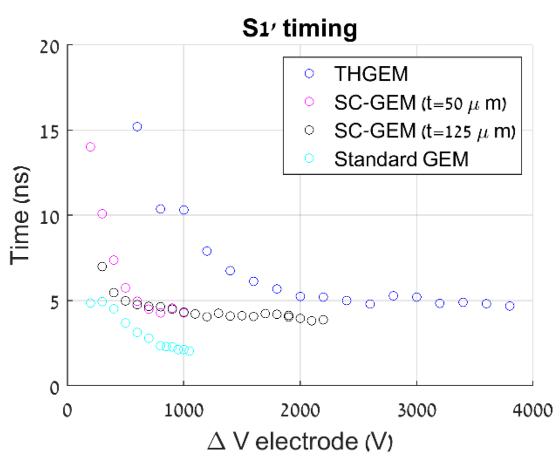

Figure 12 Timing properties of the different electrodes.

6.1.2.2.4 S1' and S2 dependence on drift field

For completeness, we present here in Figure 13 the effect of drift field on the pulse area for both charge (S2, left) and light (S1', right). While obviously at negative drift field no charge is being transferred to the electrode, the increase in pulse area with increasing electric field is a direct result of larger escape from recombination probability of the electrons at the site of interaction [3]. An interesting effect can be observed in the S1' response of the THGEM electrode, where at modest negative drift fields, a slight increase in the signal magnitude is observed before other effects (e.g. S1 light dependence on electrical field) degrade the signal.

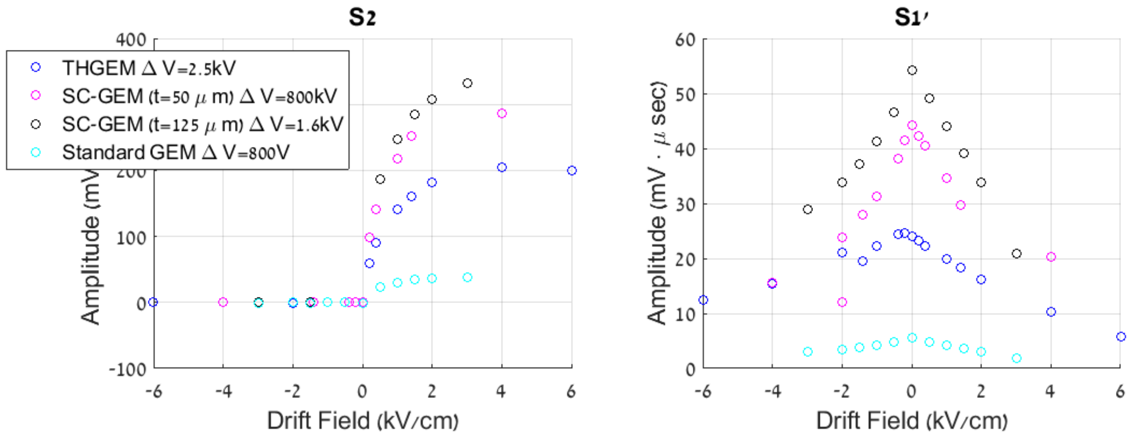

Figure 13 S1' and S2 signals as a function of the drift field.

6.1.2.2.5 S1 dependence on electrode voltage

Finally, it is worth also presenting the effect of the electrode voltage on the S1 pulse as detected from the PMT located below the electrode. The effect was reported in [46] (see Figure 14, left). The introduction of a bubble below the electrode reduces the S1 pulse by a factor ~2 compared to an electrode without a bubble. Furthermore, the application of voltage across the electrode results in a slight change of the S1 pulse. We attribute this effect (though further proof is necessary) to total internal reflection of photons when passing from the liquid to the gas phase. The slight variation in transmission with varying electrode voltage could be due to electrostriction forces altering the shape of the liquid-to-gas interface, thus modifying the reflective surface. It is interesting to note that the two different vapor pressures (1.3 bar and 2.1 bar) show different trends of the S1 signal with electrode voltage. This effect is not yet understood, but will be a part of future studies as will be discussed in the next chapters. A similar effect was observed for all electrodes. The results are presented in Figure 15 and show similar trends for the THGEM, the GEM and the 125 µm thick SC-GEM. The 50 µm thick SC-GEM S1 spectra seemed to consist of two partially overlapping Gaussians, therefore simple averaging was used to derive the mean instead of a Gaussian fit to the data. The double Gaussian structure however did not show neither in the S1' spectrum nor in the S2 spectrum.

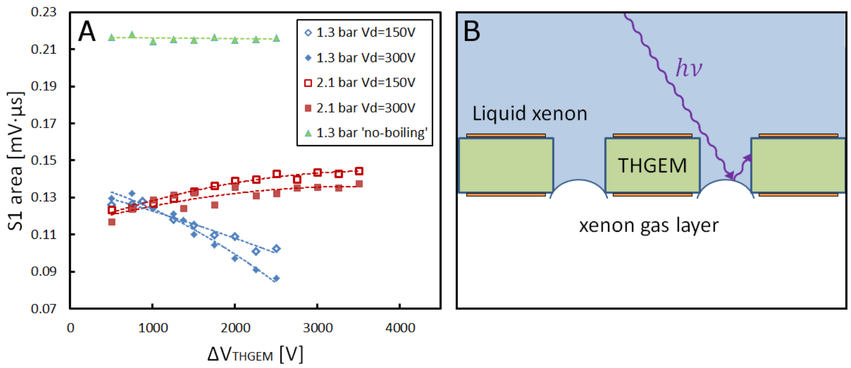

Figure 14 Left: effect of THGEM electrode voltage on S1 pulse detected by a PMT below the electrode with a bubble and without it. Right: possible explanation to this effect is total internal reflection of photons from the liquid to gas interface in the hole of the electrode. Figure taken from: [46].

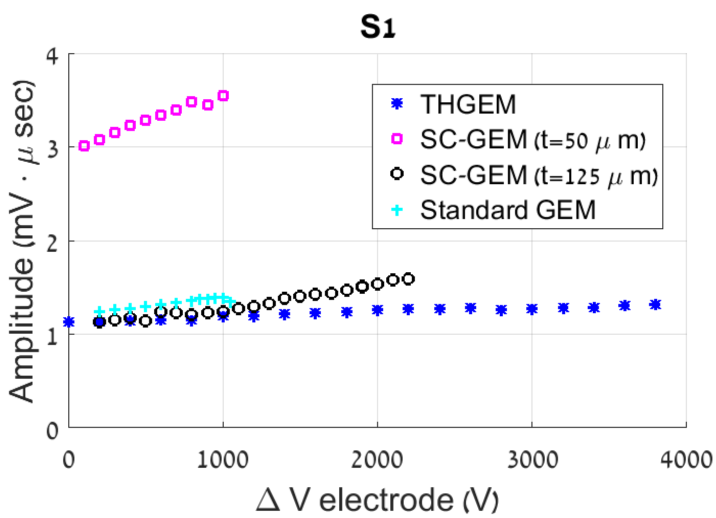

Figure 15 The effect of electrode voltage on the S1 pulse transmitted through the electrodes holes.

6.1.2.3 Amplification in the transfer gap

The threshold EL field in Xe vapor at 1.6 bar is 2.4 kV/cm [3]. At modest transfer fields between the bottom of the LHM electrode and the wire plane, the only region in which the local field is larger than the EL threshold one is within the bubble, at the bottom of the hole (at the liquid-gas interface). A major enhancement in the EL yield can be obtained by increasing the transfer field, pulling the electrons towards the heating wires. At first, additional EL occurs close to the wire surface, where the local field grows as $1/r$ (r being the distance from the wire center); at higher transfer voltages the field across the entire gap exceeds the threshold, causing EL light generation along the full electron drift-path across the bubble.

This effect is demonstrated for a 125 µm SC-GEM biased at 1,800 V with a drift field of 0.5 kV/cm. The nominal transfer field (E_t, voltage between the GEM bottom and wires, divided by the distance), was varied in steps between 0 and 15 kV/cm. The bottom PMT was operated at -450 V, to avoid signal saturation throughout the range of applied voltages. Figure 16 shows the average waveforms acquired at increasing E_t values. Initially, the waveforms look similar to those in Figure 8, comprising S1, S1' and S2 signals, where the latter two are produced in the bubble, close to the bottom of the hole. Increasing the transfer field, one observes delayed EL contributions appearing after both S1' and S2. These are EL signals produced in the bubble, at the vicinity of the wires, in addition to those produced close to the holes. Further increase of the transfer field above the EL threshold along the transfer gap itself, merges both latter EL signals. The merged EL signals grow in magnitude and diminish in width; the latter results from the increase of electron drift velocity in Xe vapor [57]).

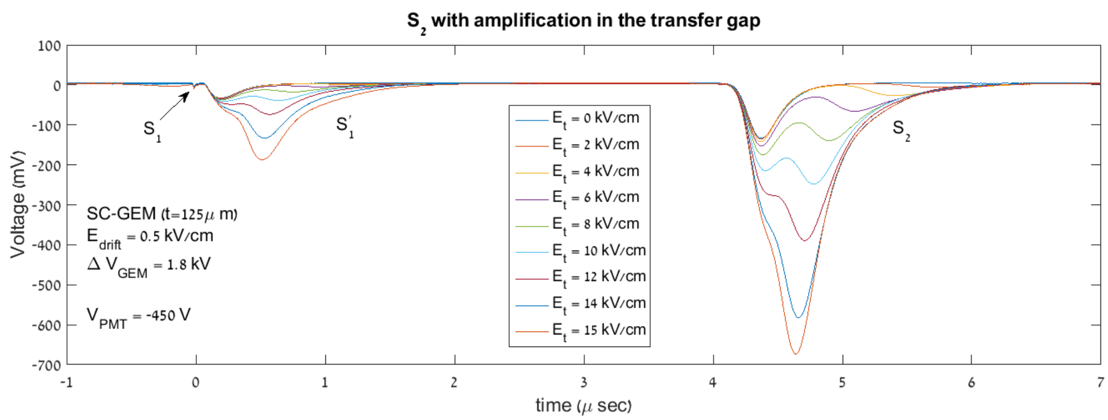

Figure 16 Average EL-signal waveforms for increasing values of the nominal transfer field between the bottom of a thick SC-GEM operated at 1,800V and the resistive-wire plane (1.6 mm below the electrode). The drift field is 0.5 kV/cm and the bottom PMT voltage is -450V.

The mean area of the amplified S1' and S2 signals for the different electrodes as a function of the transfer field are shown in Figure 17. Starting at ~2kV/cm (corresponding to a transfer voltage of 320V) an exponential trend appears, suggesting small avalanche charge gain, either at the bottom of the holes of the electrode, at the vicinity of the wires or even in the gap itself. The last points in the 125 µm SC-GEM and in the THGEM seem to saturate, however at these high field values instabilities might have caused voltage drops. At the highest E_t value, the light yield of a thick SC-GEM is estimated to be ~2,200 photons/e^-/4π.

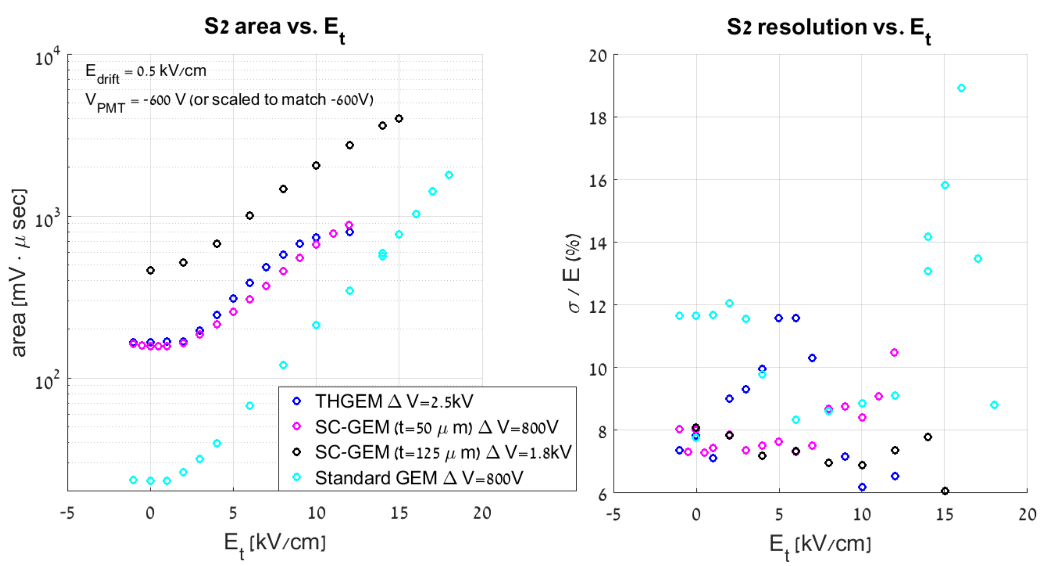

Figure 17 Left: S2 signal magnitude vs E_t keeping a constant drift field and potential difference across the electrode. Right: S2 energy resolution vs. E_t.

Along with the enhancement in light yield, the amplification in the transfer gap is also accompanied by a reduction in energy resolution. There are a few effect which may contribute to this. First, it is well known that avalanche multiplication statistics is worse than that of EL. Second, in this specific setup, the transfer gap is far from being a parallel plate configuration. Combining this with the shadowing effect of the wires, one should expect a reduction in resolution. In addition, the data points presented here were recorded at different PMT voltage to prevent signal saturation, however reduction in PMT voltage is known to adversely affect the energy resolution. A complete study to understand the behavior of the energy resolution has not been performed. Still, even if the energy resolution deteriorates at large transfer voltages, for a detector that is built for single photon/electron counting, one could compromise the energy resolution for an enhanced light output.

The pulses generated in the vicinity of the heating wires also hint towards interesting physics. In principle, when the pulses generated in the hole of the electrode and the pulse generated next to the heating wires are separated in time, the latter should not depend on the specific details of the electrode. This occurs at transfer field of ~4 kV/cm. At such conditions, if the pulses generated next the heating wire are different for the different electrodes, this may indicate on differences in the amount of charge transferred to the wire. Indeed, when computing the pulse-area only for the EL generated on the wires, the results are $120\ mV \cdot \mu s$ for the 125 µm SC-GEM and 57 for both the standard GEM and the 50 µm SC-GEM.

6.1.2.4 Estimation of absolute light yield

The effective EL yield of the LHM electrodes, i.e., the number of EL photons emitted per electron drifting in the liquid towards the electrode hole, over the full solid angle, can be estimated as follows. We denote by $N_e(E_d)$ the number of ionization electrons escaping recombination along the alpha-particle track, which depends on the drift field E_d. $\varepsilon_{col}(\Delta V_{LHM}, E_d, E_t)$ is the *collection efficiency* of electrons into the hole, which depends primarily on the voltage across the electrode ΔV_{LHM}, depends probably mildly on the drift field, on the transfer field, and could be affected by electron diffusion. We denote by $\varepsilon_{interface}$ the probability of an electron to hop from the liquid into the gas phase. $Y_{EL}(\Delta V_{LHM})$ is the number of photons emitted over 4π per electron *entering the bubble*, and is assumed to depend primarily on ΔV_{LHM} (the effect of E_d on Y_{EL} is assumed to be small and E_t at small values was measured to have negligible effect); $P_{LHM\rightarrow PMT}$ is the probability that an EL photon emitted in the bubble reaches the PMT (depending mainly on the geometry of the problem); QE_{PMT} is the quantum efficiency of the PMT at 175 nm, i.e. the average number of photoelectrons (PEs) emitted from the photocathode per photon hitting the PMT window. The number of PEs recorded by the PMT is given by:

$$N_{PE} = N_e \cdot \varepsilon_{col} \cdot \varepsilon_{interface} \cdot Y_{EL} \cdot P_{LHM\rightarrow PMT} \cdot QE_{PMT} \qquad \textit{Eqn. 4}$$

The effective EL yield is defined to be:

$$Y_{EL}^{eff} = Y_{EL} \cdot \varepsilon_{col} \cdot \varepsilon_{interface} = \frac{N_{PE}}{N_e \cdot P_{LHM\rightarrow PMT} \cdot QE_{PMT}} \qquad \textit{Eqn. 5}$$

N_{PE} in a given EL signal is the pulse area of the signal divided by the average pulse area of a single-PE event in that PMT. The single-PE spectrum of the PMT was measured at LXe temperature by setting a low trigger level on its dark count pulses. The average pulse area corresponding to the single-PE peak, was found to be $0.024\ \mathrm{mV} \cdot \mathrm{\mu s}$ for $V_{PMT} = -800\ \mathrm{V}$ (transferred through the Phillips 777 amplifier). Since all the data were typically acquired at $V_{PMT} = -600\ \mathrm{V}$, we further calibrated the PMT response at the different voltages. This was done by recording LHM signals in constant voltage setting but for different values of V_{PMT}. It was found that the mean value of the recalibrated S1' pulse area at $V_{PMT} = -600$ V is smaller by a factor of ~0.1 than that at $V_{PMT} = -800$ V; this factor represents the ratio between corresponding PMT gain values.

The QE of the bottom-PMT was measured using a vacuum UV monochromator, versus a calibrated (NIST-traceable) photodiode. It was found to be 34% at 175 nm (with a relative error of the order of 5%). The probability that a photon emitted from the bottom of the LHM reaches the PMT was calculated using a dedicated Monte-Carlo simulation (which included refraction and reflection on the bottom interface of the bubble, assuming photons are emitted from the bottom of the electrode), giving $P_{LHM\to PMT} = 0.32$.

We used the measured S2 signals in the setup described above (Figure 6) as a basis for calculating the EL photon yield. Adopting the data from [58], for $E_d = 0.5\ \mathrm{kV/cm}$ the charge yield of an alpha-particle track is 1.3 electrons/keV. Taking the average alpha-particle energy of the spectroscopic ^{241}Am source to be 5.48 MeV, this results in $N_e = 7.1 \times 10^3$ electrons. The maximum S2 pulse area of the thick SC-GEM at 1,800 V is $767\mathrm{mV}\cdot\mu\mathrm{s}$ for $V_{PMT} = -600$ V. Using the measured dependence of the PMT gain on its voltage and the single-PE response of the PMT at -800 V, we get: $N_{PE} = 767/(0.1\cdot 0.024) = 3.2\times 10^5$ PEs. From Eqn. 1 we get $Y_{EL}^{eff} = 410$ photons/e$^-$, over 4π. This value is noted in Figure 10, showing the maximal effective photon yield of a 125 µm SC-GEM.

6.1.3 Discussion

This section presents the results from a systematic study done, aiming at deeper understanding of bubble-assisted LHM detectors. The study was performed under "standard conditions" of assembly, of operation and of data recording and analysis. This enable the comparison of four type of electrodes as LHM elements: the THGEM, the GEM and SC-GEM of two different insulator thickness. The parameters in question in this study were mostly the achievable light yield, energy resolution and timing properties. Best results have so far been achieved with the 125 µm SC-GEM. It showed ~400 photons emitted per electron deposited in the liquid, with no amplification in the transfer gap. For a reasonable light collection efficiency and light detection efficiency of, say, a SiPM array recording the LHM output light, 400 photons are sufficient for detecting even single-electron pulses at practically 100% efficiency. Should one introduce amplification in the transfer gap, when up to ~2,000 photons are emitted per single electron, the structure could offer larger flexibility in designing the readout for accommodate different demands (possibly compromising other parameters such as energy and time resolutions etc.). In terms of energy resolution, $\sigma/E = 5.5\%$ is still not as good as the 3.8% achieved in XENON100 for alpha particles of the same energy [59] and the limit of 1.2% given by Poisson statistics on the number of primary electrons. The origins of this broadening of resolution is still not clear. Best timing resolution (~2 ns RMS for few thousands of photoelectrons) was achieved in a GEM due to its smallest dimensions.

While a large fraction of the physics involved in signal generation in an LHM detector is understood, there are still some effect presented in this part which lack satisfactory explanation. Most important is the difference in light yields of the different electrodes. Throughout the analysis of the results presented here, we have taken careful attention to mention that the issue of the probability of electron transfer from the upper side of the electrode hole into the bubble, through the liquid-to-vapor interface, $\varepsilon_{interface}$, is yet unresolved. The data presented in chapter discussing amplification in the transfer gap also hints towards difference in electron transmission between the different electrodes. A deeper understanding of the interface dynamics and electron transmission may explain the low energy resolution we see here compared to the one achieved in XENON100. Furthermore, the slight breathing of the bubble may also results in variations in signal magnitude, either due changes in bubble protrusion into the hole and/or due to change in the refractive interface for EL photons traveling towards the PMT. These matters will be discussed in length in the upcoming chapters as more data is presented.

6.2 Photon Detection Efficiency of LHM

6.2.1 Background

Quantum Efficiency (QE) is defined to be the average number of electrons extracted in vacuum from a photocathode (PC), per impinging photon of a given wavelength. However when a photocathode is immersed in a liquid (or placed in a gas), the resulting effective QE value (QE_{eff})varies [56]. The issue of QE_{eff} of CsI photocathodes immersed in LXe was addressed by Aprile et al. in a series of works; their results are summarized in their paper [56]. Two methods of measuring the effective QE in the noble liquid are presented here followed by their results.

The first one is by immersing a PC in LXe and placing an ^{214}Am alpha source in front of it. The 175nm VUV scintillation photons, induced by the alpha particles (non-spectroscopic source emitting alpha particles with an average energy of 2.9 MeV) stopped in the liquid ($1.6 \cdot 10^5$ photons/4π, calculated using Table 1 in [3]) interact with the CsI film, resulting in photoemission. The photoelectrons' induced current is recorded by a picoammeter. An effective QE value of 31% was calculated, in this work, by normalizing the signal to the solid angle, to the alpha emission rate and to the number of photons emitted by an alpha-particle event in the LXe.

A second method was based on measuring the photocurrent from the CsI photocathode using a mercury lamp in vacuum (185nm emission line), comparing it to the response of a calibrated photodiode - and then, measuring the CsI-photocathode photocurrent when immersed in LXe. In [56], vacuum measurements yielded QE=8%, and in LXe: QE=24%. This was explained in [56] by a change in the work function of the photocathode when immersed in LXe. Note that these photocurrent measurements were performed at 185nm, compared to that with alpha-particles with LXe scintillation occurring at 175 nm. According to [56], when multiplying this number by the ratio of photocurrents in vacuum for the corresponding wavelengths, one recovers the effective QE=31% value at 175nm.

6.2.2 Comparing photocurrent in vacuum and LXe

6.2.2.1 Setup and procedures

A THGEM electrode with vacuum-deposited CsI on one of its surfaces was placed in the LXe cryostat with the CsI facing downwards (see Figure 18). A 85% transparent electroformed mesh was placed underneath the THGEM. The voltage difference applied between the photocathode and the mesh determined the electrical field for electrons extraction. An external Hg lamp (flushed with N_2) was used to illuminate the CsI at 185nm wavelength. High voltage was applied to the mesh while the THGEM/CsI surface was kept at ground potential through a Keithley 610C picoammeter. Photocurrents where measured both in vacuum and in liquid, before during and after liquefaction.

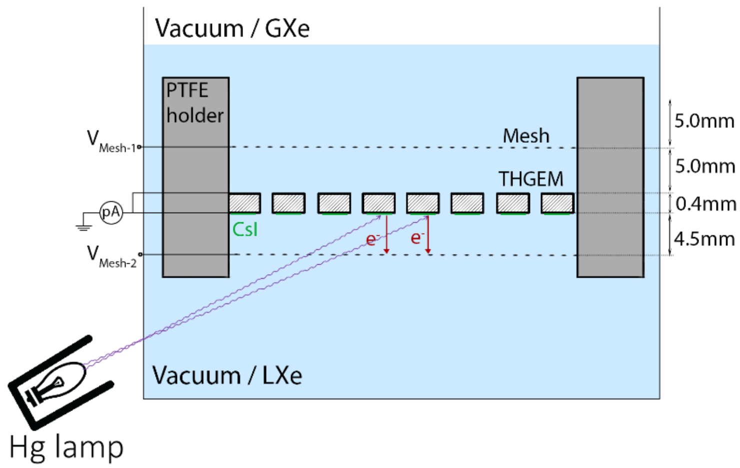

Figure 18 Setup for measuring photocurrent from a photocathode in vacuum and immersed in LXe.

6.2.2.2 Results

Before assembly in the cryostat, the QE of the PC was estimated to be 18%. The photocurrent as a function of the electric field was measured 4 times: (i) in vacuum before Xe liquefaction, (ii) immersed in LXe, (iii) in vacuum directly after LXe extraction (PC at ~250K), and (iv) in vacuum 12 hours after LXe extraction (PC at RT). One should however note that prior to this measurement, the same photocathode had undergone a cooling cycle, possibly compromising its overall QE.

The results are given in Figure 19. One clearly sees that the photocurrent in LXe is larger than that of vacuum for high enough field values. At the highest point (19 kV/cm), LXe photocurrent exceeds that of vacuum by a factor of 1.17. One should however notice that the photocurrent before the introduction of LXe and after its extraction has dropped by ~25%. Since this electrode had undergone a cooling cycle prior to this measurement, it is reasonable to assume that the photocurrent had dropped in this first cycle and the values measured in vacuum are due to a lower QE than that when the photocathode was first deposited. Still, the qualitative conclusion remains, that the ratio of vacuum-to-LXe currents is larger than one, showing an enhancement of the effective QE in LXe compared to QE in vacuum (as observed in [56]). This effect is explained in [56] by the polarizability of LXe, which generates a potential well for electrons, effectively lowering the work function of the PC in the liquid medium.

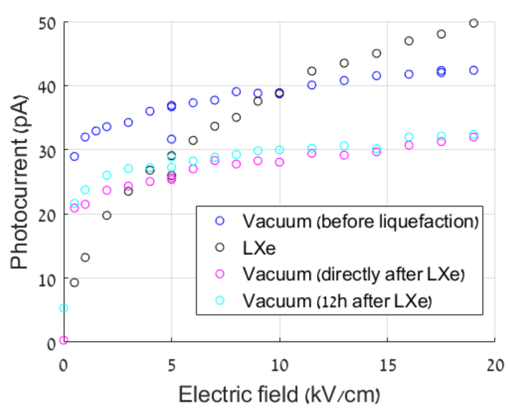

Figure 19 Photocurrent as a function of the electric field at the surface of the photocathode.

6.2.3 Measuring photocurrent with intense alpha source

6.2.3.1 Setup and procedures

A second method relied on recording photocurrent induced on a CsI photocathode by the scintillation in LXe, from alpha-particles of an intense ^{241}Am source immersed in LXe (Figure 20). The CsI photocathode, deposited on gold plated copper on an FR4 substrate, was placed below the source, with a 85% transparent woven stainless steel mesh separating them. The interaction of the alpha particles in LXe induces scintillation light; a fraction of which (depending on the solid angle) impinges on the photocathode, inducing photoelectron emission. The Pyrex cylinders in Figure 20 were placed to ensure measurement of photons emitted only within the defined solid angle (Pyrex is known not to transmit the VUV light). Upon application of an electric field between the photocathode and the mesh, a photocurrent is induced and measured on the photocathode using a Keithley 610C picoammeter.

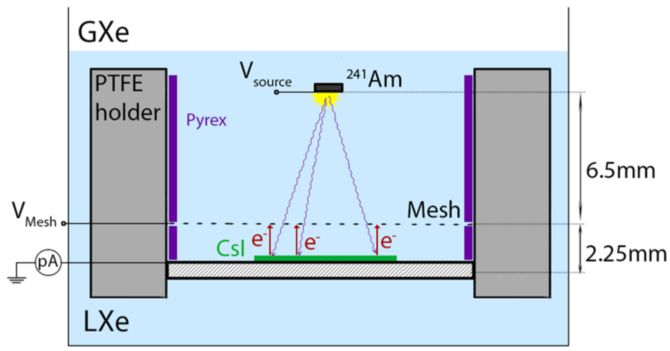

Figure 20 Setup used to measure the effective quantum efficiency for the extraction of a photoelectron from a CsI photocathode immersed in LXe. Scintillation photons from the interaction of 5.5 MeV alpha particles extract photoelectrons form a CsI photocathode. The photocurrent is directly proportional to the number of electrons emitted from the photocathode. The experiment was repeated with a PMT of known QE, replacing the CsI photocathode.

The photocurrent is given by the following formula:

$$I = \frac{E}{W_s} \cdot f \cdot \left(\frac{\Omega}{4\pi}\right) \cdot T \cdot e^- \cdot \ QE_{eff} \qquad \textit{Eqn. 6}$$

Where:

- E is the average energy of alpha particles emitted from the source. The average energy of the alpha particles of our non-spectroscopic source was measured to be 2.9 MeV (with a solid-state detector and by comparing scintillation pulses from this source to that of a spectroscopic one [60].
- W_s is the average amount of energy needed to generate a scintillation photon at zero electric field. Five different values for this parameter are found in [3], four are within close agreement ($17.9, 19.6 \pm 2.0, 16.3 \pm 0.3, 17.1 \pm 1.4$ eV); a fifth one is standing out, being 39.2 eV . For our purposes, the average of the first four was used.
- f is the emission rate of the source. It was measured using a PMT placed in front of the source by counting scintillation pulses in LXe. We have concluded a counting rate of 6.7 kHz
- $\left(\frac{\Omega}{4\pi}\right)$ is the solid angle of photons emitted from the source towards the CsI sensitive area It was computed from the geometry.

- T is the optical transparency of the mesh. Measured to be 85%.

Throughout the measurements, the source plate and the mesh were kept at equal electrical potentials to avoid electrons or ions from the interaction point to drift towards the photocathode and distort the photocurrent measurements.

6.2.3.2 Results

The electric field on the surface of the photocathode, in this simple configuration (Figure 20) is ratio of the voltage between the mesh and the photocathode divided by their distance. The photocurrent measured vs electric field is shown in Figure 21. At its maximum value (~14 kV/cm), the photocurrent of ~30 pA corresponds to the effective QE of ~30% and seems to grow mildly afterwards.

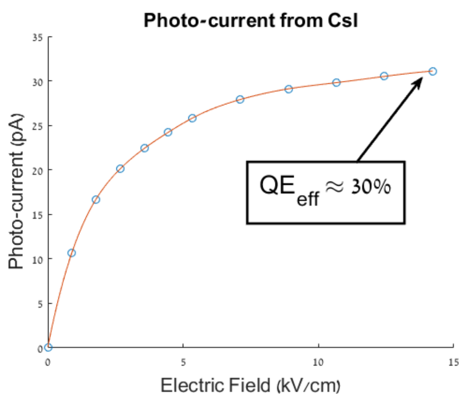

Figure 21 the photocurrent as a function of the electric field on the surface of the photocathode immersed in LXe. At its maximum, a QE of ~30% was calculated (see text).

6.2.3.3 Caveat – validation with PMT

In order to gain confidence in the systematics and reliability of the setup above (Figure 20), the CsI photocathode was replaced with a pre-calibrated PMT (Hamamatsu R8520-406 LV1626). The photocurrent recorded in this setup was ~2 fold larger than the one expected from the known QE of the PMT. The discrepancy suggests a systematic error, putting in doubt the effective QE=30% acquired previously with a simple flat CsI photocathode.

Two possible explanations have been raised to explain this discrepancy, both are still pending experimental proofs.

a. It is known that Pyrex (see location in Figure 20) does not transmit VUV light at 175nm. However, it is not exactly known what the index of refraction is at this specific wavelength. Should the index of refraction be much different than that of LXe, it is possible that photons at low grazing angles are not being absorbed in the bulk but rather reflected off the surface, thus contributing to the photocurrent.
b. It is known that some metals have non-vanishing reflection coefficients for photons at 175 nm. Stainless steel for example shows ~57% reflection, while copper reflects 22% or much less depending on its surface-oxidation state [3]. Reflection of photons off the alpha-source plate can therefore increase the amount of photons impinging on the photocathode per event, thus increasing the measured photocurrent.

6.2.4 Estimating LHM-PDE from CsI QE

Based on the measurement presented in Figure 21, one can calculate the field on the surface of a photocathode and assign a local QE_{eff} value for each point on the surface of the photocathode. Figure 22 presents such a computation of the electrical field on the surface of a photocathode for two different electrodes (a THGEM biased to 2.1 kV and a GEM biased to 1 kV). Similar computations were also performed for the two SC-GEMs. The expected QE_{eff} as a function of voltage across the electrode is presented in Figure 24 below for $E_d = 0.5\ kV/cm$ and $E_t = -1\ kV/cm$ (to accommodate the operation conditions of section 6.1).

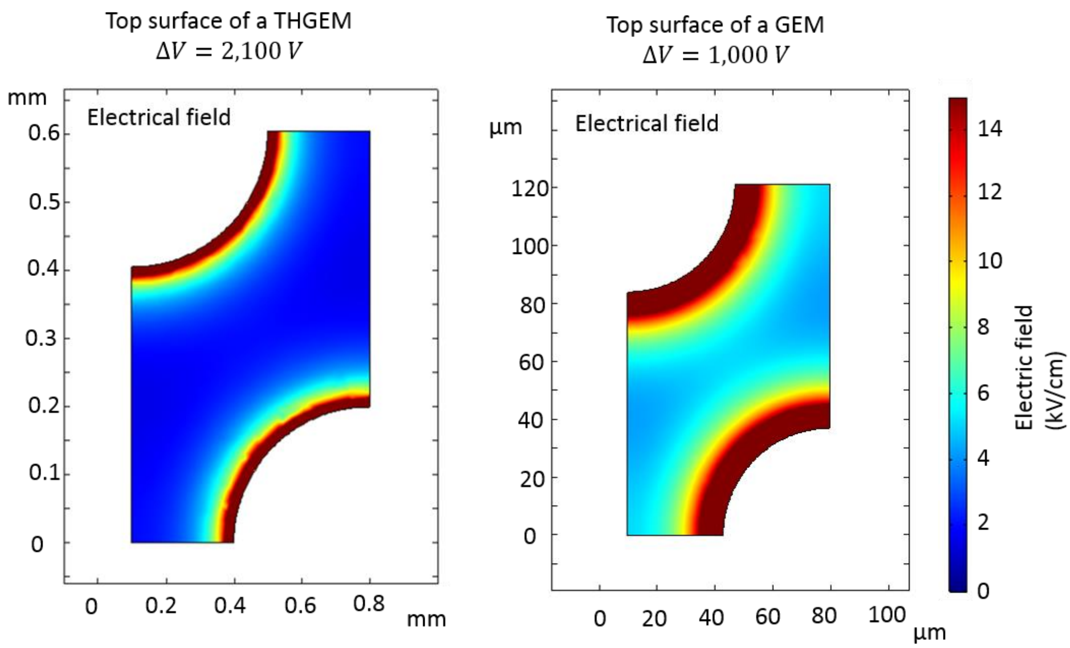

Figure 22 Electrical field on the surface for a unit cell of a THGEM electrode (left) biased to 2.1 kV and that of a standard GEM electrode (right) biased to 1 kV as simulated using COMSOL®.

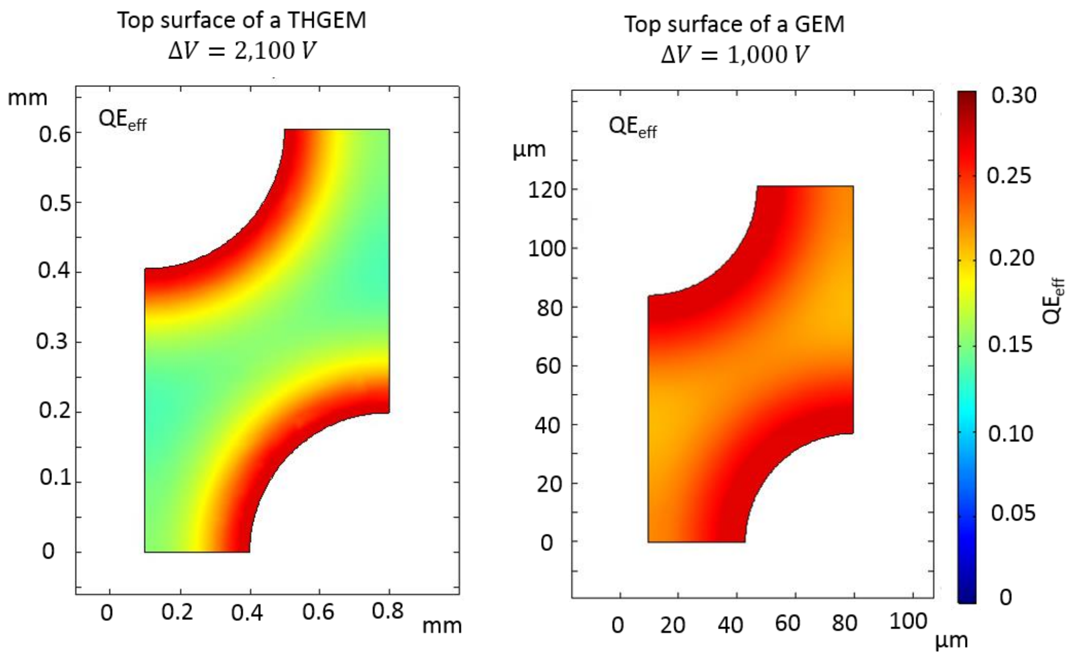

Figure 23 Local effective QE on the surface of a THGEM biased to 2.1 kV (left) and on a GEM biased to 1 kV (right).

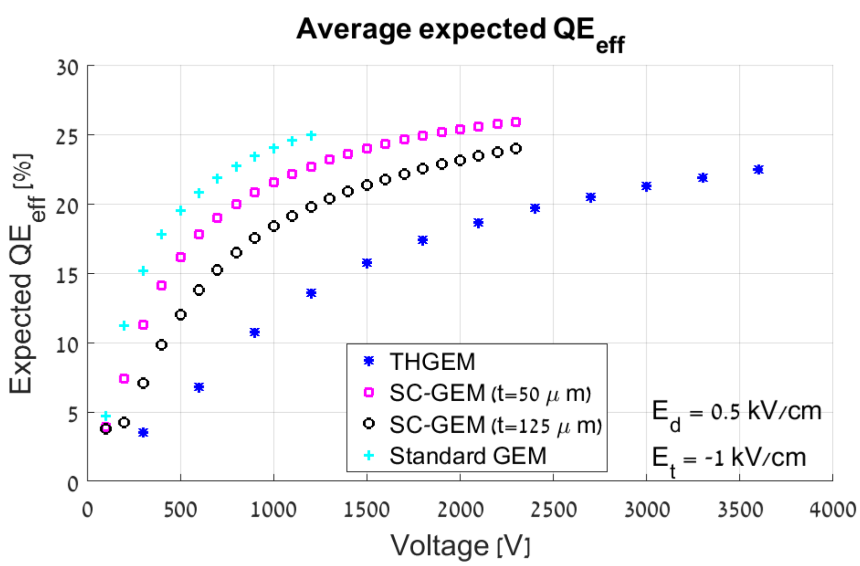

Figure 24 Expected average QE_{eff} across the entire surface of an electrode, as a function of voltage across the electrode. Computed for $E_d = 0.5\ kV/cm$ and $E_t = -1\ kV/cm$ using COMSOL®.

6.2.5 Estimating LHM PDE using S1'/S2

6.2.5.1 Experimental Setup and Methodology

In a setup where both light and charge are detected in an LHM element from the same event, it is possible to deduce the photodetection efficiency, PDE, value by comparing the photoelectron signal to the charge signal; i.e. S1'/S2 in Figure 10. The experimental setup is the one described in the comparative study section above and depicted in Figure 6.

As discussed in the above section on estimating the light yield of the different electrodes, the number of photoelectrons at the PMT is given by Eqn. 5.

The magnitude of the S1' signal is somewhat more complicated, as the EL photons are emitted in this case from holes across the entire active area of the LHM, rather than only its central 4 mm.

$$S1'(E_d, \Delta V_{LHM}) = N_{ph}(E_d) \cdot \int_{CsI\ area} P(src \to \vec{r}) \cdot QE_{rff} \cdot \varepsilon_{eff}(\vec{r};\ E_d, \Delta V_{LHM}) \cdot Y_{EL}(\vec{r}; E_d, \Delta V_{LHM}) \cdot P(\vec{r} \to PMT) \cdot dxdy \cdot QE_{PMT} \qquad \textit{Eqn. 7}$$

Here: $N_{ph}(E_d)$ is the average number of primary scintillation (S1) photons emitted into 4π from the alpha particle track; $P(src \to \vec{r})$ is the average probability for an S1 photon to reach a point on the LHM electrode at $\vec{r}$; $\varepsilon_{eff}(\vec{r};\ E_d, \Delta V_{LHM})$ is the probability that a photoelectron emitted from CsI at $\vec{r}$ will be successfully drifted into the bubble averaged over an LHM unit cell (the dependence on $\vec{r}$ is introduced because of the variation of the external field, defined by the source holder, field shaping ring and top LHM electrode); in $Y_{EL}(\vec{r}; E_d, \Delta V_{LHM})$ the variation in the external field may, in principle, affect the degree of bubble penetration into the hole, but this is likely a small effect; $P(\vec{r} \to PMT)$ is the probability that an EL photon emitted from the bubble at $\vec{r}$ will reach the PMT window.

While $P(\vec{r} \to PMT)$ is fairly easy to estimate form a simple self-written Monte Carlo simulation, $P(src \to \vec{r})$ is far more elaborate in the setup we have been working with. Specifically, the holders and spacers which are made of PTFE and the stainless steel field shaper all have a high reflectivity to VUV photons [3]. The accurate estimation of the probability of a photon to reach a certain point on the electrode is therefore a matter for an elaborate Monte Carlo simulation.

6.2.5.2 Results

All electrodes where placed in the same setup with the same distances to source and PMT. All electrode except for the THGME had an active area of 14mm in diameter, the THGEM had an active area of 20mm. In order to be able to compare the S1'/S2 ratio of the THGEM to that of the GEMs, resulting S1'/S2 data shown in Figure 25 were normalized to the solid angles according to

$$\frac{\frac{1}{2} \cdot (1 - \cos\theta_1)}{\frac{1}{2} \cdot (1 - \cos\theta_2)} = 0.66 \qquad \textit{Eqn. 8}$$

Where $\theta_{1/2}$ are the half-angles defining the cone in which scintillation photons are emitted towards the respective photocathodes.

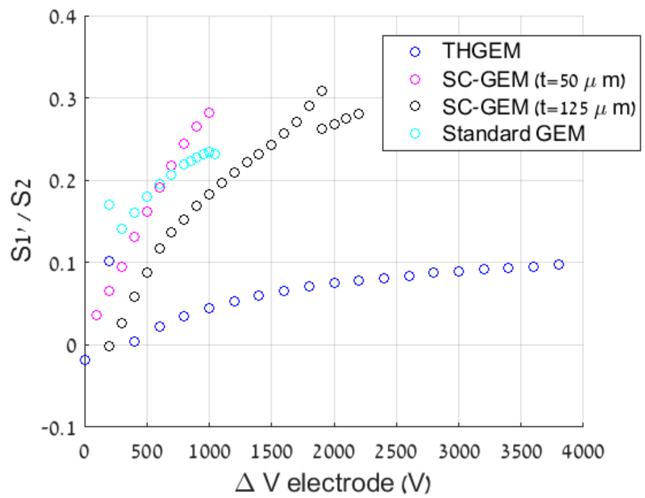

Figure 25 Ratio of photoelectrons signal to that of ionization electrons S1'/S2. THGEM datum was scaled according to the solid angle, to match the data of the other electrodes.

As discussed above, the complete evaluation of the PDE using this method relies on a few different assumptions (S2 charge collection into the holes) and a few photon-tracking simulations which haven't yet been carried out. We are therefore left here with a comparative figure of all electrodes. Knowing however the absolute PDE of any of these electrodes at even a single voltage configuration, will enable one to convert the S1'/S2 values to PDE values. The following third method explains how this is done using a single-photon source. This will later be compared to the results obtained using the discussed simulations once done.

It is however worth mentioning that previous naïve studies (where the geometry was less controlled than here and the light transport simulations have not been fully carried out) have shown with the same methodology a PDE of ~3% for a THGEM and ~5% for a standard GEM. Much less than expected from the integrating QE_{eff} according to the simulated electric field map on the top surface of the photocathode.

6.2.6 Measurement of LHM PDE with single-photon source

6.2.6.1 Methodology

A major difficulty in the measurements of single-photon response is the generation of a reliable single-photon source. The solution suggested here relies on inducing a small scintillation pulse in an enclosure immersed in LXe. A small pinhole is placed at a distance from the radiation-interaction site, and the solid angle is designed such that the probability of a photon, generated in a scintillation event, to pass through the pinhole will be small (usually P<10%). This way, the probability of two photons passing in a single event is even smaller ($\propto \mathrm{P}^2$). A PMT is placed inside the enclosure, registering the number of events. The total number of photons that have passed through the pinhole at a specific time interval is simply the product of the number of triggers recorded by the PMT and the probability of the photon to pass through the pinhole. The detector under test is placed in front of the pinhole. The number of events seen by the detector will be as follows:

$$\begin{aligned}&\#events\ in\ detector = \\ &= \#triggers\ in\ \mathrm{PMT} \times \mathrm{P}(photon\ passing\ pinhole) \times \mathrm{PDE_{detector}}\end{aligned} \quad \textit{Eqn. 9}$$

Counting the number of events on the detector, the number of triggers (PMT inside enclosure) and knowing the probability of a photon passing through the pinhole - determines the PDE of the detector.

In the schematic view of the "single photon source" (Figure 26), an ^{214}Am source with a 1mm thick stainless steel filter was placed inside the enclosure; it passes mostly 60 keV gamma through, to interact in the LXe, with an attenuation length of 0.4mm [61]. Pulse-area analysis was carried out from the top (trigger) PMT. Only events falling 2σ around the main 60 keV peak were considered in the data analysis. 60keV x-ray conversion in LXe result in ~4020 VUV photons emitted over 4π [3]. According to the geometrical dimensions, there is a chance of 5.7% for a single photon to pass through the pinhole per converted 60 keV event.

With the 1mm thick stainless steel filter, the rate of the source was estimated to be ~150 Hz. Each measurement consisted of recording ~90,000 waveforms during ~20 min.

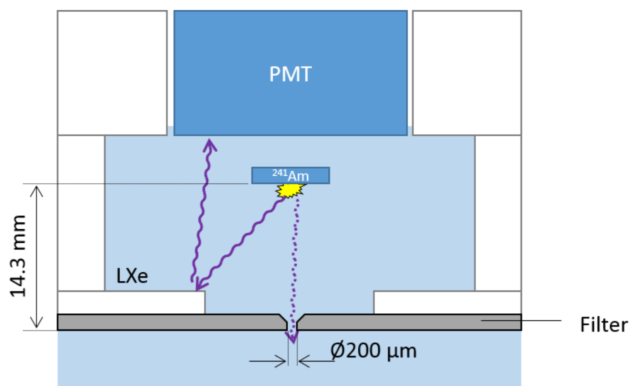

Figure 26 Schematic view of the "single-photon source". The probability of a photon resulting from the conversion in LXe of a 60 keV photon (from an ^{241}Am sources covered with 1mm thick stainless steel filter) to pass through the pinhole in this geometry is estimated to be 5.7%.

6.2.6.2 Validation of setup with known-QE PMT

Before the introduction of a "detector under test", a PMT (Hamamatsu R8520-406 LV1626) was placed after the pinhole (see setup in Figure 27). The PMT's QE of ~34% was measured in advance in a vacuum monochromator by comparing it to a NIST-traceable photodiode. This setup was used as a sanity check, as it allows comparing the photon transmission of the pinhole calculated from geometrical consideration to that measured by the photomultiplier.

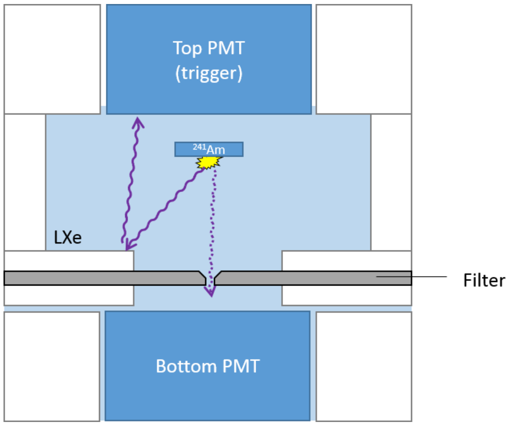

Figure 27 Setup for the validation of the "single-photon" source. The "detector under test" located in LXe was a PMT who's QE was measured in advance in comparison to a NIST-traceable photodiode.

The anode pulses of the PMTs where digitized using a Tektronix MSO-5204B oscilloscope. The typical pulses as seen by both PMTs are depicted in Figure 28. The orange pulse is that of the trigger PMT and the blue pulse is a single-photoelectron induced signal, seen by the bottom PMT. Analysis of the waveforms was done using dedicated Matlab scripts. An automatic peak finder algorithm was applied to the waveform of the bottom PMT investigated.

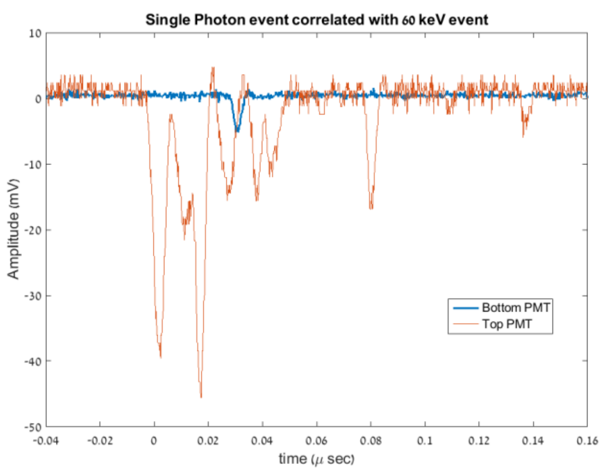

Figure 28 Typical pulses seen by the two photomultipliers. The orange line is a 60 keV gamma event in LXe, as seen by the trigger PMT. The blue line is a single-photon response of the bottom PMT, which is the detector under test.

When using the bottom PMT as a calibration device, there are two subtleties that needs to be taken into account. The first being the dark pulse rate. In order to estimate the dark counts, the peak finder algorithm was applied twice, once on the real time window and once on the time window preceding the trigger. The latter gives an estimation of the randomly-occurring pulses. The dark-pulse rate was estimated to be $1 \cdot 10^{-5}$ per 200 ns, which is the time window during which a single-photon pulse is expected.

The second point is the difference between the single-photon detection efficiency of the PMT and its QE. At large photon energy, the bi-alkali photocathode has a probability of emitting two electrons per event. The effect was reported in [62] and was easily measurable in our setup. The single-photon spectrum derived from the measurements (Figure 29) was fitted with two Gaussians where the mean of the second one was forced to be twice that of the first. The ratio of their heights gave an estimate for the probability of a two-electron process. Therefore, since the QE is the average of number of electrons emitted per incoming photon, the QE and the PDE are connected via $\mathrm{QE} = \mathrm{PDE} \cdot (1 \cdot (1 - \mathrm{P_{2e}}) + 2 \cdot \mathrm{P_{2e}}) = \mathrm{PDE} \cdot (1 + \mathrm{P_{2e}})$ where $\mathrm{P_{2e}}$ is the probability of two-electron process. From the fit of the spectra we derived $\mathrm{P_{2e}} = 19.8\%$.

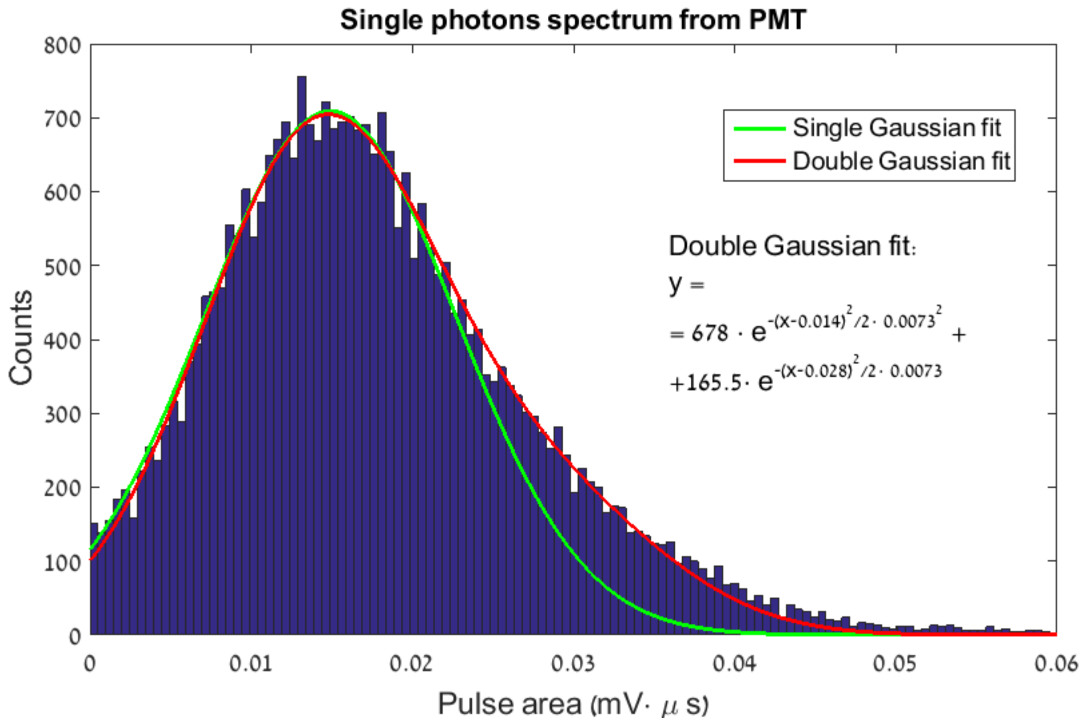

Figure 29 Single-photon spectrum with a double-Gaussian fit. The probability of double photon process is the ratio of the two photon peak amplitude to the sum of the amplitudes.

A set of 90,000 events triggered by the top PMT were recorded, digitized and processed. Out of the total, events were selected to be within $\pm 2\sigma$ around the mean value of the 60 keV peak. The transmittance of the pinhole can therefore be extracted from the following relation:

$$\begin{aligned} &\#\text{events in detector} = \\ &\quad = \#\text{triggers in PMT} \\ &\quad \times \left(\mathrm{P(photon\ passing\ the\ pinhole)} \times \frac{\mathrm{QE}}{(1+\mathrm{p})} - \#\text{expected dark pulses}\right. \end{aligned} \qquad \textit{Eqn. 10}$$

Plugging in the measured numbers, one concludes that the geometrically-computed 5.7% probability for a photon to pass through the pinhole in a 60 keV event is reliable and can be used to estimate the PDE of an LHM setup.

6.2.6.3 Experimental Setup with an LHM detector

After validating the reliability of the “single-photon” source, an LHM element was placed in front of the pinhole. The setup is shown in Figure 30. The LHM consisted of a THGEM electrode (a=0.7, d=0.3, t=0.4, h=0.01mm). Underneath the electrode, two sets of resistive wires where placed (55 microns diameter, 2mm spacing). The bottom set of wires was used to generate the bubble. The top set was used to generate high transfer field in the gap below the electrode. Two sets of wires were used in this setup in order to make sure that the top wires set is completely surrounded by the bubble such that the high field region in the vicinity of the wire can be fully exploited for EL generation. Note that since the wires are 55 microns in diameter, spaced 2mm apart and the distance between the bottom of the electrode and the wire is 1.5mm, the field changes substantially over the transfer gap. Therefore the values quoted here are that of the voltage differences between the bottom of the electrode and the wires.

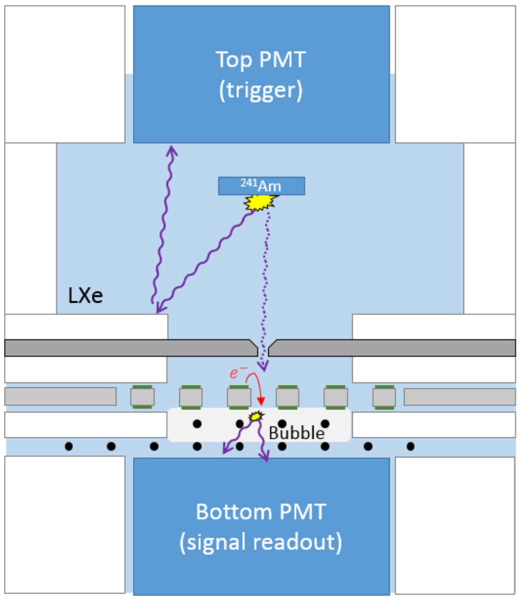

Figure 30 Schematic view of setup for measurement of PDE of LHM with single photons.

A PMT (Hamamatsu R8520-406 LV1626, the same as used in the experiment of the single-photon source validation) was placed 2 mm underneath the bottom array of wires. It recorded the pulses resulting from the LHM element. The PMT anode signal was directly digitized using a Tektronix MSO 5204B oscilloscope. Waveforms from this PMT were recorded in correlation with the waveforms of the single-photon source ("trigger") PMT and saved. Data analysis was done offline using dedicated Matlab scripts.

The CsI photocathode was evaporated on the THGEM in a vacuum deposition setup. The QE in vacuum of the CsI was measured by comparison to a NIST-traceable photodiode (Ball Aerospace photodiode, serial no. 1-926) to be 18.5%. The setup was installed in a dry nitrogen glove box and transferred, with minimal exposure (few seconds) to atmosphere, into the Ar-flushed cryostat. The chamber was then evacuated using a turbo-molecular pump and a cold finger dipped in LN_2 to remove water pressure to be below $1 \cdot 10^{-6}\ mbar$. Gaseous Xenon was then introduced into the chamber and circulated through the purifier for ~2 days. After Xe liquefaction, the liquid was circulated through the purifier for two more days, after which the bubble under the electrode was formed. The bubble was left for two hours to stabilize before starting an experiment.

6.2.6.4 Results

The recorded waveforms from both the trigger PMT and bottom PMT reading the LHM element were processed offline. The top PMT waveform was used to determine whether the event was within $\pm 2\sigma$ around the 60 keV line. A peak-finder algorithm was applied to the waveform of the bottom PMT. Figure 31 depicts such a waveform recorded with 2kV across the THGEM and 5 kV in the transfer gap (i.e. between the bottom of the THGEM and the top-wires array). The orange trace is the trigger pulse, the blue trace is the bottom PMT signal and the circles are the peaks detected by the peak finder algorithm. The time difference between the trigger and the LHM response is due to the time it takes the photoelectron to travel from the photocathode, through the LXe and into the EL region in the bubble.

In order to understand the background for this experiment, data was recorded also with zero voltage with respect to ground on all electrodes. However since the PMTs were both biased to -800V, data was also taken when all electrodes where biased to -800V, thus minimizing the electric fields in the structure.

A histogram of the number of peaks (i.e. number of photoelectrons in the PMT) within a time window of 4 µs after the trigger pulse was plotted. Figure 32 shows three histograms in 3 different voltage configurations. In Yellow are the histograms recorded where all the voltages on the electrodes where at ground potential. In blue are the histograms with minimal electric fields, namely when all the electrodes are biased to the PMT voltage of -800V. In Cyan, green and red are the histograms with 2 kV across the THGEM and with increasing transfer fields of 1.5, 3.5 and 5.0 kV.

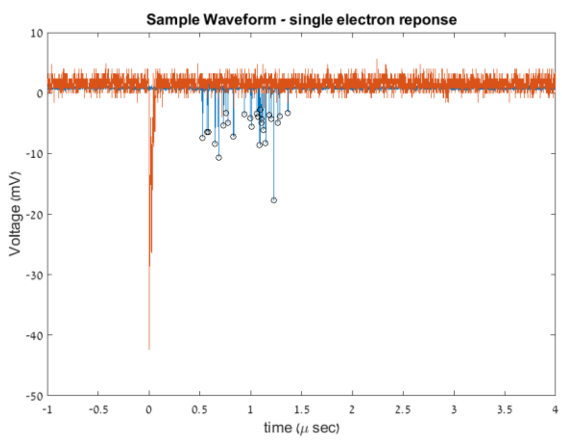

Figure 31 Waveforms of a single-photon response of the LHM element. Recorded at 2kV across the THGEM and a transfer voltage of 5 kV. The orange trace is the trigger PMT pulse. The blue trace is the signal from the PMT below the LHM element. Circles are the single-photo-electron pulses detected by the peak finder.

By looking at the spectra on the left side, one clearly sees that turning on the voltage across the THGEM (even with very low transfer field) results in an increase in the number of events showing a few photoelectrons in the histogram. However, since the increase in the number of events is very small compared to the number of background events (note the logarithmic scale), the error on the number of "real" events would be very large. By increasing the transfer field (middle and right spectra), one sees that the added events drift towards the right and are clearly separated from the background events. Counting these events and normalizing to the total number of triggers and to the probability of photons to pass through the pinhole, one concludes that the PDE derived from this data set is 0.93% (with 10% error - originating mainly from the Poisson statistics on the number of events). If we use this data to "normalize" the S1'/S2 data given in Figure 25, at best, the thick SC-GEM shows a maximal PDE of 3.5% at 1,900V across its faces.

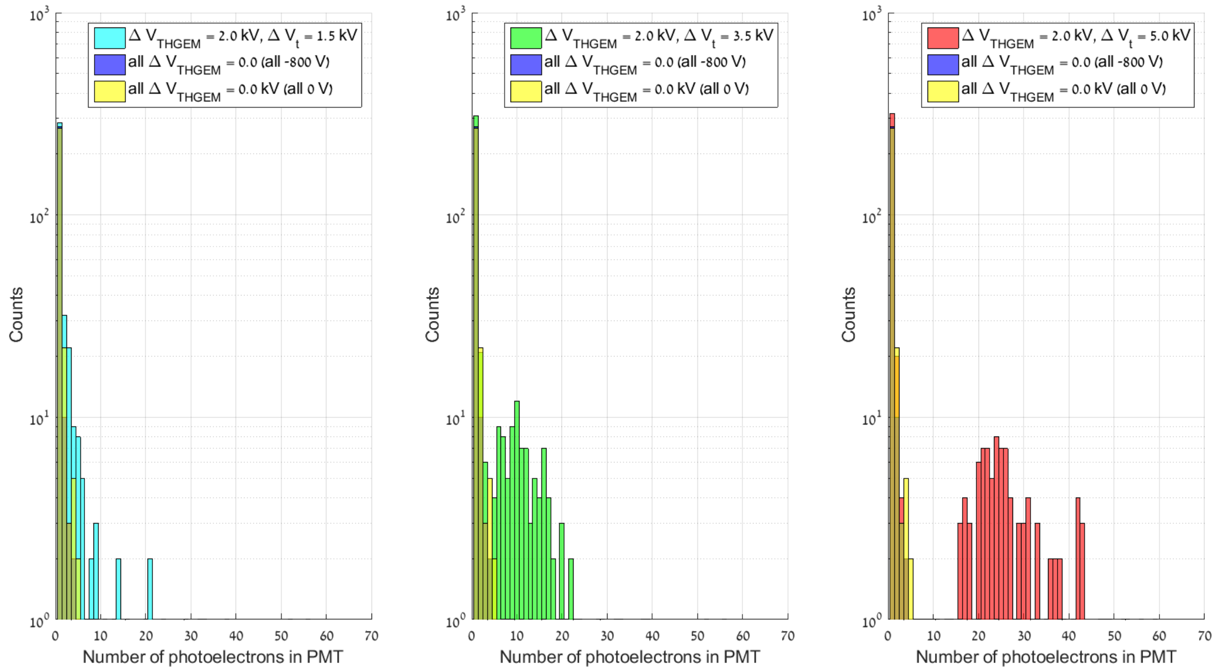

Figure 32 Histograms of the number of photoelectrons detected at the bottom PMT. Each figure depicts three histograms. Yellow: zero-voltage on all electrodes. Blue: minimal electric field (all electrodes at -800V). Cyan, green, red: 2kV across the THGEM and 1.5, 3.5, 5.0 kV/cm across the transfer gap.

6.2.7 Verifying possible wavelength shifting in LXe

6.2.7.1 2.2.6.1 Using Pyrex to block VUV

In an attempt to understand why the PDE of the electrodes measured using single photons and S1'/S2 is much lower than expected from the effective QE values, a suspicion has been raised that impurities in LXe may shift a fraction of the VUV light to the visible spectrum. Assume this indeed is the case, the CsI photocathode (having a cutoff at 210 nm [51]) will not respond to such longer-wavelength photons, however this will be measurable with the PMT - sensitive from the VUV range to the visible range. A setup was therefore designed to understand whether there is wavelength shifting in the LXe. A Pyrex window was placed between the ^{241}Am alpha source and a PMT. A second PMT was placed above the source (not blinded by the Pyrex) to provide the trigger. Schematics is shown in Figure 33. The Pyrex window was measured in advance in a vacuum monochromator. Its transmission as a function of wavelength is shown in Figure 34.

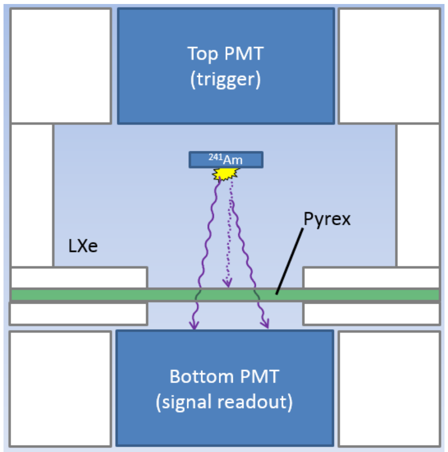

Figure 33 Schematic view of the setup to determine a possible wavelength shifting to above 280 nm in the LXe.

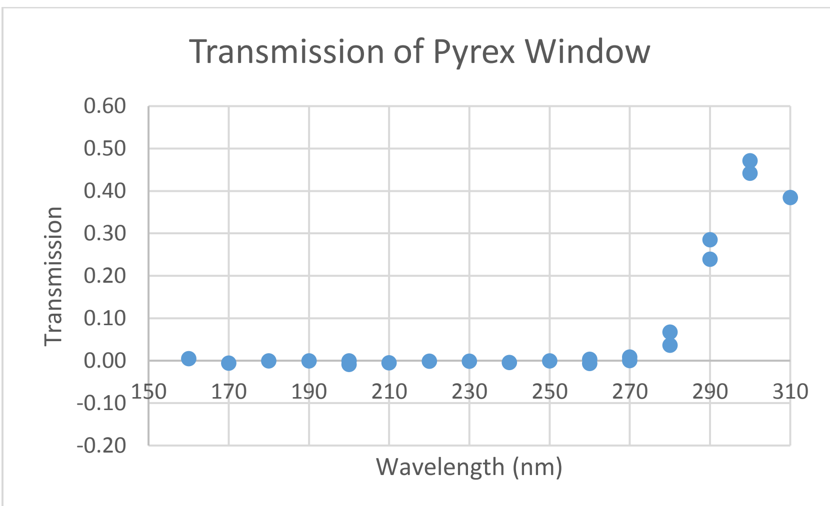

Figure 34 Transmission of Pyrex as measured by the vacuum monochromator. Data is shown here until 310 nm due to the cutoff of the monochromator, but Pyrex is well known for its transmission in the visible. The range of wavelengths was scanned twice, upwards and downwards to avoid equipment hysteresis effects.

A sample waveform is shown in Figure 35 below. The magenta trace is the trigger PMT that records the reflected scintillation light. The yellow trace is the bottom PMT which is behind the Pyrex filter, thus blind to VUV photons. One can clearly see that while most of the light comes promptly on the top PMT, it does not show on the bottom one. There are however some delayed components that are able to pass through the Pyrex window. These are also shown on the top PMT. Note that there could still be wavelength shifting from 175 nm to anything between 210 nm (cutoff of CsI) and 280 nm (cutoff of Pyrex) which this experiment is not sensitive to. This very small amount of wavelength shifting could result from fluorescence of the PTFE structure, but cannot explain the PDE discrepancy [63].

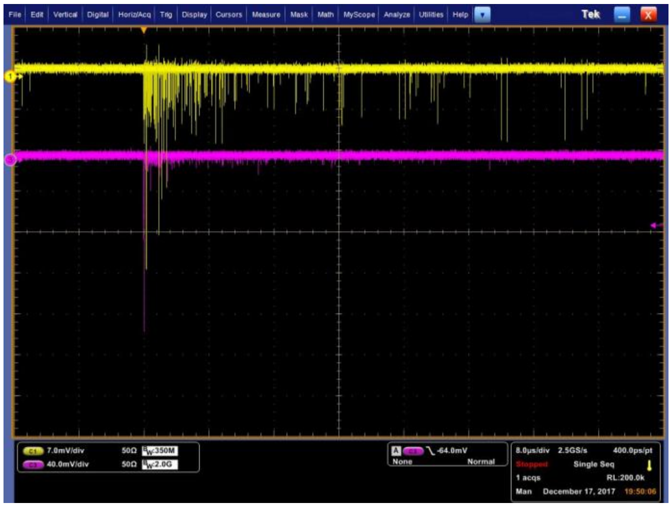

Figure 35 Oscilloscope snapshot of both waveforms as seen by the top and bottom PMT. The magenta trace is the top ("trigger") PMT while the bottom one is the PMT behind the Pyrex window.

6.2.7.2 2.2.6.2 Using VUV narrow band filter

For a final proof that most of the light is due to 175nm scintillation, a narrow-band filter (eSource optics P/N 12172FNB) with peak wavelength at 172.0 nm and FWHM 20.0 nm was placed instead of the Pyrex window shown in Figure 33. The Ø12.7mm filter was placed with its active side facing upwards. The filter's transmission as a function of the wavelength as measured at room temperature in the vacuum monochromator is shown in Figure 36. The transmission was measured before introduction into the LXe and again after its extraction from the cryostat. The transmission has not shown any noticeable change, suggesting the thin layer survives cool down to LXe temperatures and warm up.

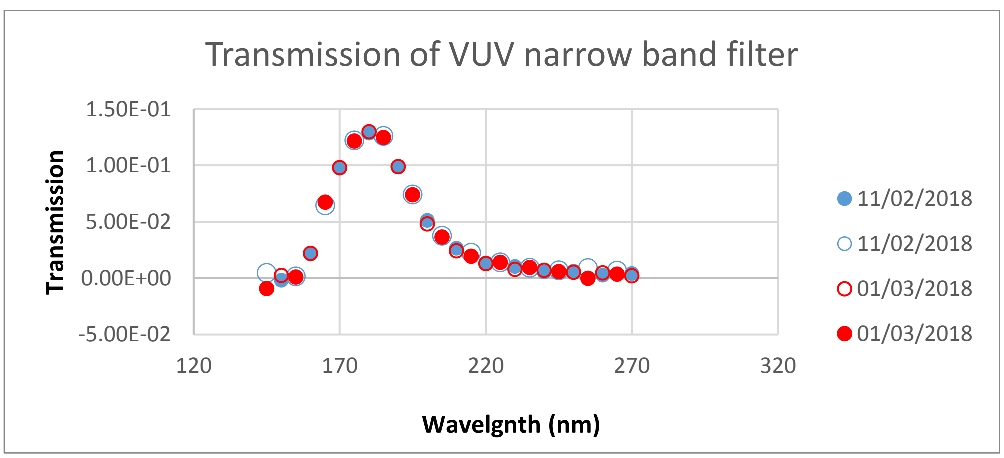

Figure 36 Transmission of narrow-band VUV filter as measured at room temperature as a function of wavelength. The two first data series (blue) are before introduction into LXe, the two other sets (red) are after introduction and extraction from LXe.

By normalizing the spectrum of S1 pulses to that of single electrons of the PMT, one can calculate the amount of photons impinging on the PMT (~480 photoelectrons / pulse). By assuming the alpha-source energy of 2.9 MeV, 17.7 eV/scintillation photon (table 1 in [3]), computing the solid angle, assuming 13% transmission of the VUV NB filter and PMT's QE=34%, one computes ~420 photons. We thus conclude that most of the scintillation light arriving to the bottom PMT and, in other experiments, to the CsI photocathode are indeed VUV photons (no significant wavelength shifting).

6.2.8 Summary and discussion

Presented in the table below, is a collection of data regarding the expected and measured PDE, of the LHM detector. The expected PDE is based on averaging QE_{eff} across the area of the electrode (using the surface field as calculated using COMSOL). The measured PDE of the THGEM is based on the measurements with the single photon source as described above. The measured PDE of the rest of the electrode is achieved by scaling the ratio of S1'/S2 (Figure 25) with respect to the measured THGEM PDE.

Electrode	Bias voltage (V)	Expected PDE	Measured PDE
THGEM	2 kV	~18%	0.93%
GEM	1 kV	~24%	2.9%
SC-GEM (50 μm)	1 kV	~22%	3.5%
SC-GEM (125 μm)	1.9 kV	~25%	3.5%

The data presented in this table tell *an important story* regarding our understanding of the LHM detector. While we expect ~25% of the photoelectrons to be detected in the best SC-GEM, only 3.5% of them finally show. This factor ~7 reduction in efficiency hints that electrons are lost somewhere on their way from the PC to the bubble underneath.

It has been suggested that electron diffusion may play a role, as electrons emitted from the PC may be lost by transverse diffusion to the hole's insulating wall. The transverse diffusion coefficient D_T of electrons in LXe varies between ~100 to 50 cm^2/s for fields in the range 4-9 kV/cm (decreasing with the field) ([2] and references therein); these characteristic values correspond to the field along typical photoelectron trajectories for both the GEM and thin SC-GEM. For a typical drift time $t_d \sim 50\ \mathrm{ns}$ for electrons starting halfway between GEM holes and a typical transverse diffusion coefficient $D_T \sim 70\ \mathrm{cm}^2/\mathrm{s}$, the RMS diffusional spread is $\sigma = \sqrt{2 D_T t_d} \sim 30\ \mu\mathrm{m}$. Since the inner diameter of the bi-conical GEM hole is 50 μm, considerable loss of electrons to the wall seems plausible (especially on the top conical part of the hole). However this does not seem to be the main cause degrading the PDE as increasing the hole diameter to 300 μm (both SC-GEMs and THGEM) should have solved this issue.

With no better hypothesis at hand, the issue of electron transfer efficiency into the bubble seems to naturally reveal itself again as the main suspect. The discussion section at the ends of this thesis suggests a possible explanation and future directions to look into.

In a more general view, the PDE of the detector plays a critical role for its potential introduction into large-scale experiments. As discussed in [22] and will be discussed further in this thesis, an LHM with PDE~15% would be able to greatly improve photon-detection sensitivity in future multi-ton Dark Matter experiments. A low PDE on the other hand, may impair it from being a viable photon-detector candidate for this type of experiments.

6.3 Position reconstruction

For the first demonstration of LHM position sensitivity we opted for the Hamamatsu quad Silicon Photomultiplier (SiPM) unit (type VUV4 S13371-6050cq-02, PDE=24% @ 175nm [64]) as light readout. The schematic view is shown in Figure 37. However, prior to experiments, analytical calculations [65] and Monte Carlo simulations have been carried out to understand the theoretical limitations and expected properties of the position resolution of an LHM element coupled to a SiPM readout.

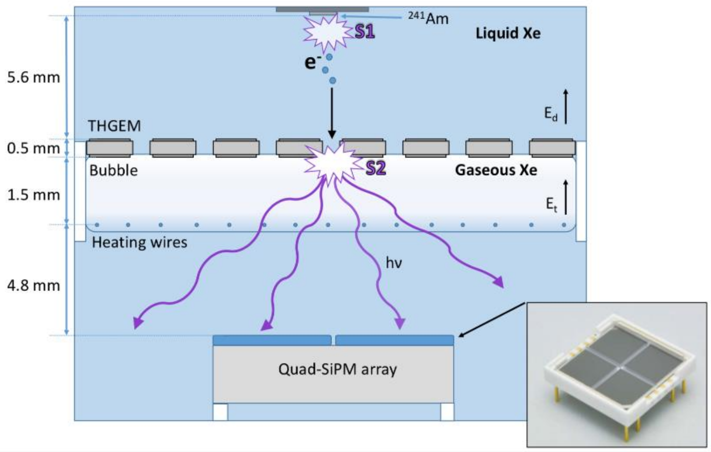

Figure 37 The Quad-SiPM LHM detector scheme (not to scale). A 0.4 mm thick THGEM electrode (with 0.3 mm in diameter holes spaced by 0.7 mm) is immersed in LXe; the gas bubble underneath is formed by a grid of heating wires, spaced 2 mm apart, located 1.5 mm below the electrode; the Quad-SiPM array is located at 4.8 mm under the wire grid. Ionization electrons focused into the holes induce EL light (S2) in the bubble; a fraction of the primary scintillation S1 flash traverses the holes. Both photon signals are detected by the SiPMs, yielding the event's energy signal and location. The 12 x 12 mm2 Quad-SiPM detector is shown on the right.

6.3.1 Simulation

6.3.1.1 Simulation methodology

The MC simulations were carried out for an array of SiPMs located below an LHM electrode Figure 37. The SiPM array was assumed to be either within the bubble or in the liquid below the bubble, in which case the effect of photon refraction was taken into account. The number of photons emitted from the holes of the electrode per event was assumed to originate from the charge of an alpha particle (mathematically assuming $\varepsilon_{col} \cdot \varepsilon_{interface} = 1$), with a light yield of 50 photons/e$^-$/4π (indeed, our best reported above photon yield is ~ 420 photons/e$^-$/4π) and a probability of 10% for the photons to be detected in the SiPM. The photons were assumed to be emitted isotropically. The number of hits on each of the pads in the readout array was counted and used to compute the center of gravity (COG) according to:

$$\vec{X}_{COG} = \frac{1}{N}\sum_{i} n_i \vec{X}_i \qquad \textit{Eqn. 11}$$

Where N is the total number of photons hitting all the pads, $\overrightarrow{X_\iota}$ are the coordinates of the pad's center and n_i is the number of hits on each pad. Figure 38 shows an example of such hit pattern and the computed COG. This process was repeated for 2,000 events, serving to construct a distribution of X_{COG}, to which a Gaussian was fitted (Figure 39). The mean value and the resolution (σ) was extracted from the fit.

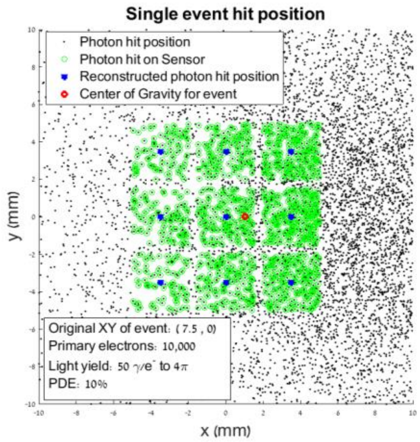

Figure 38 Example of an event generated by the MC simulation at original position (7.5,0). Here, we used a 3x3 SiPM array of 3x3mm² each to detect the signal, located 10 mm below the electrode. One can clearly see that while the distribution of the impinging photons is centered around (7.5,0), the center of gravity as computed from the hit pattern is only slightly shifter to the right with respect to the center.

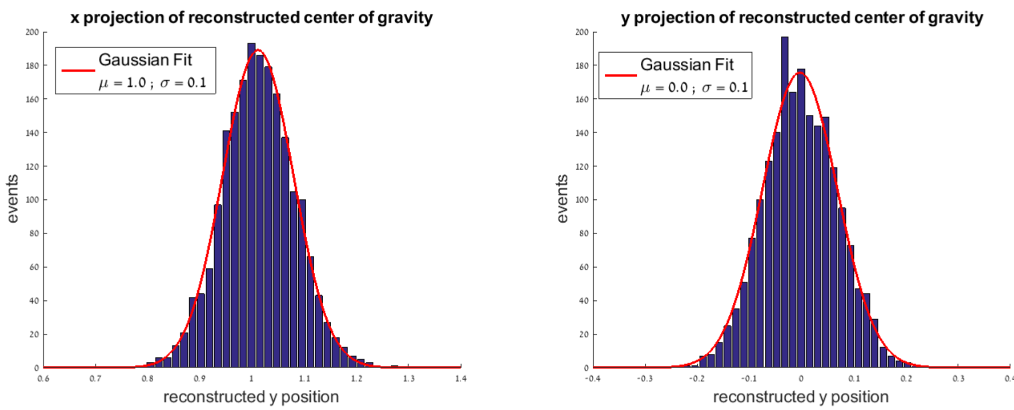

Figure 39 Center of gravity histogram. The photon were generated at the original location of (7.5,0) as seen also in the above picture, the center of gravity was computed for the above 3x3 array of 3x3mm² each.

The same procedure was repeated for varying locations of the initial light pulse (denoted X_{real}). This served to establish the relation between the center of gravity and the actual location from which the light was emitted, mathematically: $X_{COG}(X_{real})$. This connection can be inverted to $X_{real}(X_{COG})$. Therefore, if one measures the X_{COG} one can reconstruct the original location of the event by using $X_{recon} = X_{real}(X_{COG})$. The error on this value, which is the certainty at which we know the actual starting position of the pulse, is given by:

$$\Delta X_{recon} = \frac{dX_{real}}{dX_{COG}} \cdot \Delta X_{COG} \qquad \text{Eqn. 12}$$

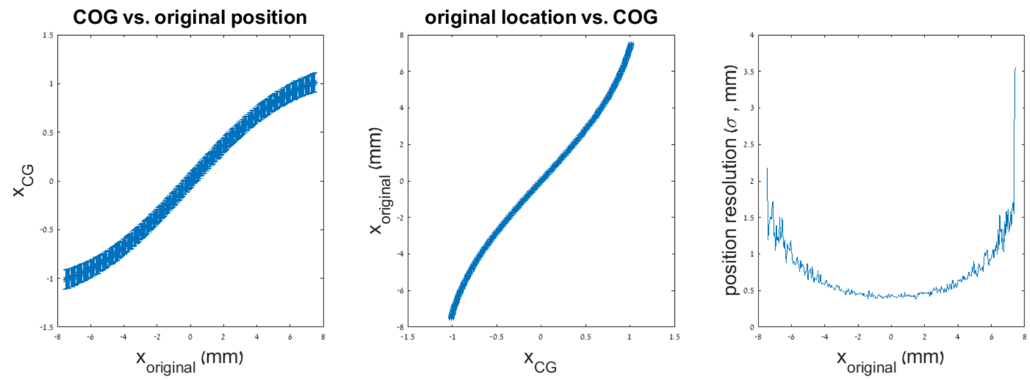

Figure 40 Left: X_{COG} as a function of the original location. Middle: the inverted connection (real position as a function of the center of gravity). Right: position resolution as a function of location.

Where, as noted earlier, ΔX_{COG} is taken from the width of the Gaussian fit. This location resolution as a function of the real hit location is given in Figure 40 (right).

6.3.1.2 Different readout arrays

Figure 41 presents the position resolution simulated for different arrays of readout differing in the number of pads and the inter-pad spacing. The different colors in the figure indicated different pixel sizes. The shapes of the markers indicate the spacing. Finally, the black curve is the only 3x3 readout array. Once can clearly observe that the apparent improvement in the readout resolution is due to the pixel size. This however can be explained (as will be shown next) due to an increase in the number of detected photons. Finally, this was used to set a green light towards the use of a 2x2 pixel array of 6x6 mm² each spaced 0.5 mm apart as a preliminary readout for the following experiments.

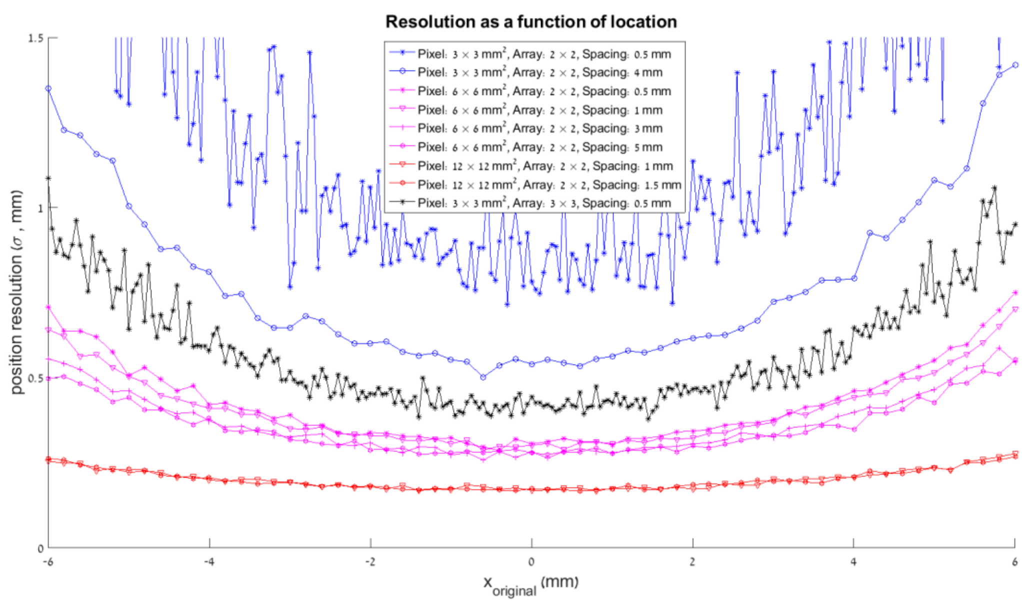

Figure 41 Position resolution as a function of location of the original event for different arrays of SiPM, with different inter-diode spacing. All simulations performed with 10,000 primary photons, 50 photons/electron and assuming PDE=10%. The readout was located 10 mm below the electrode and was assumed to reside in the gas.

6.3.1.3 Effects of refraction gas to liquid

When the readout array is located in the liquid below the bubble, photons emitted in the gas undergo refraction when passing from the gas phase into the liquid. This results in a focusing effect of the photons directed towards the readout array. Thus, the resolution is also expected to improve. Photon transmission and position reconstruction has been simulated in three different conditions: (a) readout in LXe (n=1.69 [19]), (b) readout in the bubble (n = 1) and (c) an intermediate value (n=1.3). Physical dimensions are as given in Figure 37. The results are shown in Figure 42.

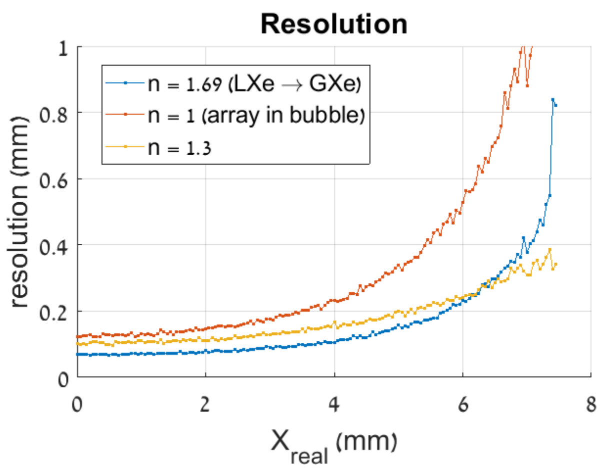

Figure 42 Position reconstruction resolution as a function of location for different diffraction coefficients for the photons. Physical dimensions as given in Figure 37.

6.3.1.4 Distance of the readout array

Figure 43 presents the COG as a function of the location of the event for different distances of the readout array from the bottom of the electrode. For simplicity, it was assumed here that the readout is in the gas and therefore no refraction of photons was taken into account. A few important conclusions can be drawn from this figure. First, the closer the array is to the emission point, the shorter is the range of linearity of the COG method is. Second, the farther away the readout array is, the smaller the slope at the linear regime is and therefore the worse the achievable position resolution. Finally, the fact that the slope changes with depth, points to a major complication of the COG reconstruction method. As will be discussed later in the experimental section, there is good reason to generate EL not only in the holes of the electrode but also along their trajectory from the hole towards the heating wire. However, as the different slopes suggest, EL emitted closer to the readout array (e.g. on the heating wire) will require a different normalization factor than EL emitted further away (e.g. from the hole of the electrode). Although mathematically correctable, this significantly complicates the reconstruction algorithms.

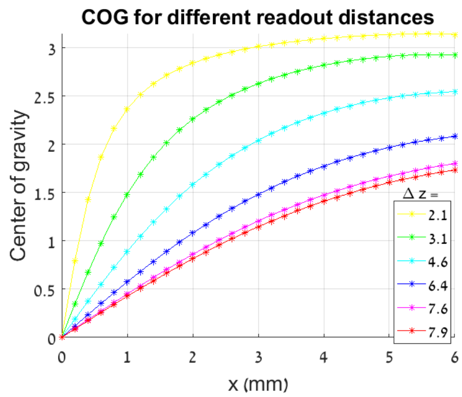

Figure 43 Center of gravity (in arbitrary units) of light emission as a function of the distance from the center, computed for different distances of the readout array from the light emission point.

6.3.1.5 Effect of light yield

Figure 44 presents the effect of the amount of light emitted from the bottom of the hole on the resolution. The simulation has been performed with physical dimensions as in Figure 37, n = 1.69, PDE=10% of light readout, and with varying amounts of photons emitted as mentioned in the legend. Experimentally, the amount of light is product of the primary charge and the effective light yield of the detector. Figure 44 clearly shows the expected improvement in the resolution when the light yield increases.

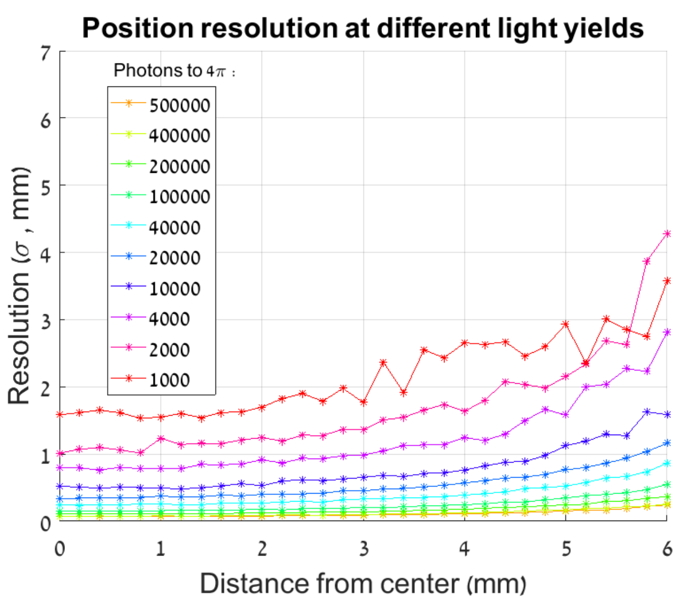

Figure 44 Position reconstruction resolution as a function of the distance from the center for different photon yields emitted to 4π.

6.3.2 Imaging using LHM

6.3.2.1 Experimental setup & methodology

The experiments were carried out in our MiniX LXe cryostat. The LHM detector (Figure 37) had a 0.4 mm thick THGEM electrode with a hexagonal holes' pattern (0.3 mm in diameter holes, spaced by 0.7 mm), without a photocathode; therefore, the detector was sensitive only to ionization electrons. The latter were deposited by alpha particles from a ^{241}Am source (activity of ~190 Bq); it had a ~0.5 mm broad annular shape, of ~3.9 mm in diameter (see source image in the results section below). A grid of parallel heating wires (Ni-Fe, 55 µm in diameter, 2 mm spacing) was placed 1.5 mm below the electrode, generating the bubble. Polarized at an adequate potential, the wire-grid established an electric field across the bubble (transfer field, E_t); its intensity permitted the generation of EL signals close to the liquid-gas interface at the hole's bottom, across the bubble (in the transfer gap) and at the vicinity of the wires.

The EL signals were recorded with a quad-SiPM array located in the liquid, 6.3 mm under the THGEM electrode's bottom face. This Hamamatsu Quad VUV4 MPPC (model S13371-6186) is suitable for operation at cryogenic temperatures; with its quartz window, it is sensitive to the Xe VUV excimer photons (175 nm). Each SiPM segment has an area of 6x6 mm^2, with a 0.5 mm gap between segments; it has 13,923 pixels per segment and a geometrical fill-factor of ~60%. It was mounted on a printed board, with an R-C supply circuitry (Figure 45). The operation voltage was maintained at -57 V; at RT, its photon detection efficiency (PDE) is ~15% at 175 nm, as stated in [66].

Electroluminescence-induced signals from each segment were digitized with a Tektronix digital oscilloscope (MSO 5204B) and recorded for offline post-processing using dedicated Matlab scripts. The trigger was provided by primary-scintillation (S1) photons reflected off PTFE spacers (not shown; located above and around the source holder) and detected by a PMT located above the ^{241}Am source (not shown). The choice of S1 as a trigger is natural in this specific setup for two technical reasons (a) primary scintillation from 5.5 MeV alpha particles generates a large prompt flash of light (~10^5 photons/4π) and (b) the fixed drift distance of electrons from the interaction point to the detector facilitates analyzing the time structure of their induced pulse shape.

Ionization electrons deposited by the 5.5 MeV alpha articles (40 µm range in LXe), were drifted under E_d towards the THGEM-electrode and focused into its holes. The EL induced at the bottom of each hole permitted imaging the holes' pattern and to determine the position resolution of the reconstruction technique. Event position reconstruction was done by a simple center-of-gravity (COG) method, followed by calibrating the distances according to the electrode's holes pattern. Mathematically:

$$\vec{R}_i = A \cdot \frac{\sum_j \vec{r}_j L_{ij}}{\sum_j L_{ij}} \qquad \text{Eqn. 13}$$

Where $\vec{R}_i$ is the reconstructed location of event i, L_{ij} is the light intensity (i.e. the integral under the recorded pulse) on pad j at event-number i, $\vec{r}_j$ is the location of the center of the j's pad and A is a global scaling factor. The latter was used for maintaining the 0.7 mm spacing between the hole centers. Finally, a 2D histogram of the reconstructed locations was plotted.

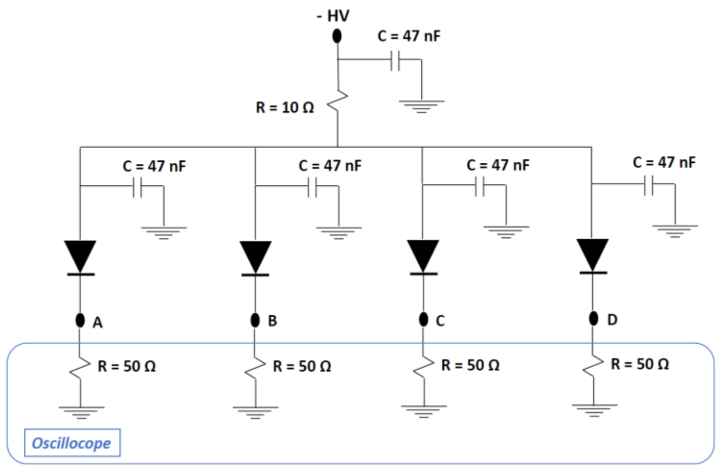

Figure 45 Electrical diagram of the Quad SiPM supply board and readout (50 Ω at the oscilloscope input).

6.3.2.2 Results

6.3.2.2.1 Analysis of SiPM signals

A typical few-photons spectrum, recorded in LXe (T~173 K) on a single SiPM segment is shown in Fig. 4. The waveforms were recorded by setting a low trigger on the SiPM output; the signals are due to dark pulses originating from the SiPM with some contribution by pixel-cross talk.

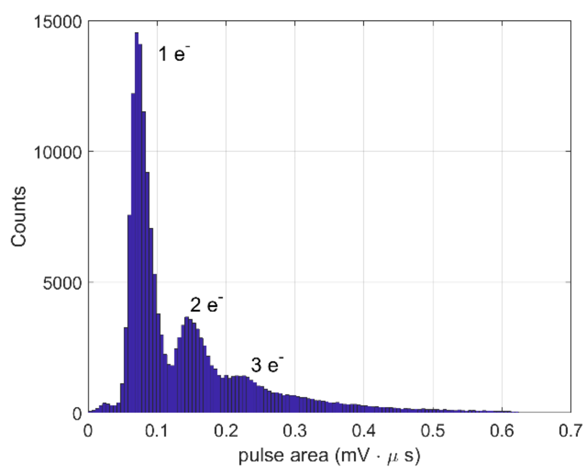

Figure 46 A dark-noise spectrum recorded in LXe, on a single SiPM segment, showing the response to one or a few electrons.

An example of typical alpha-particle waveforms recorded (in the detector shown in Figure 37) from each of the four Quad-SiPM channels is shown in Figure 47. One can observe a small fraction of the primary-scintillation S1 photons that traversed the THGEM holes, and the S2 EL signals. The waveforms shown in Figure 47a were recorded at a voltage applied across the THGEM electrode $\Delta V_{THGEM} = 2.1\ \mathrm{kV}$, with $E_t = 0$ and $E_d = 0.5\ \mathrm{kV/cm}$; they correspond to EL produced close to the hole's bottom; the total pulse width at the base is ~0.5 microseconds. The ones shown in Figure 47b were recorded at the same ΔV_{THGEM} and E_d values but with $E_t = 12\ \mathrm{kV/cm}$; their shape is due to EL photons generated at the hole's bottom (first peak), along the electrons' path across the bubble (middle dip) and in the high-field region approaching the grid-wires (second peak); the total pulse width at the base ~2 µs.

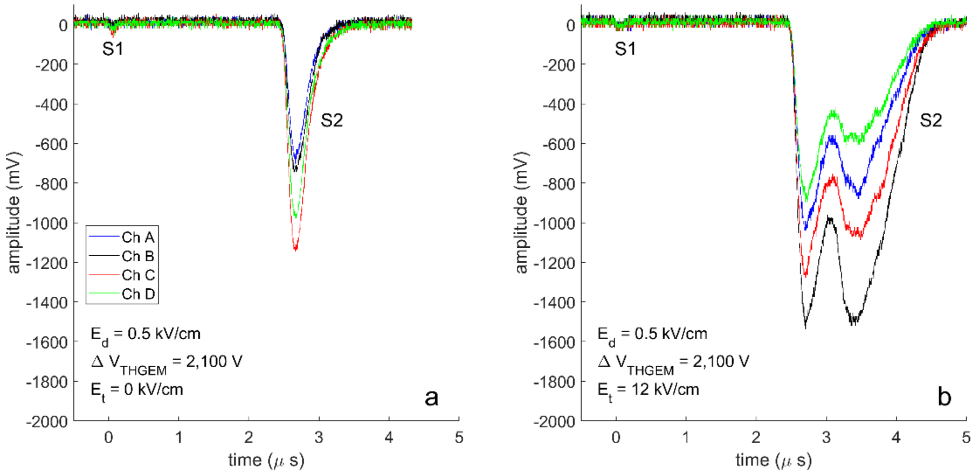

Figure 47 a) Typical waveforms recorded on the four SiPM pads (A-D) with no transfer field ($E_t = 0$) showing residual S1 pulses and S2 EL pulses generated at the vicinity of the liquid-bubble interface at the bottom of the hole. b) Waveforms recorded under a relatively high transfer field ($E_t = 12\ kV/cm$), showing S1 pulses and S2 EL pulses from the vicinity of the liquid-bubble interface, along the transfer gap and close to the heating wires.

The S2 energy resolution of the present SiPM-LHM setup was derived from the distribution of the number of photoelectrons recorded by the SiPM - computing the area under each waveform, normalized to that of a single photoelectron. An example of a pulse-area spectrum is shown Figure 48, for LHM voltage settings: $\Delta V_{THGEM} = 3.6\ \mathrm{kV}$, $E_d = 0.5\ \mathrm{kV/cm}$ and $E_t = 0$; this distribution, induced by alpha particles, was recorded from the four SiPM segments. A Gaussian fit provides the distribution mean (μ) and resolution. Similar to previous S2 resolution (~7% RMS) obtained with a THGEM-LHM and a PMT readout, the energy resolution obtained here with the SiPMs is 6.6% RMS. Note that the addition of a transfer field resulted in a slight degradation of the energy resolution (to 9% RMS); this however may be improved by optimizing the detector operation parameters, as discussed below. The low-energy tail of the distribution in Figure 48 is attributed to alpha particles leaving a fraction of their energy in the source's matrix, while the excess of events at the right of the peak corresponds to the coincidence of 5.48 MeV alphas with the source's 60 keV gammas (as discussed in [52]).

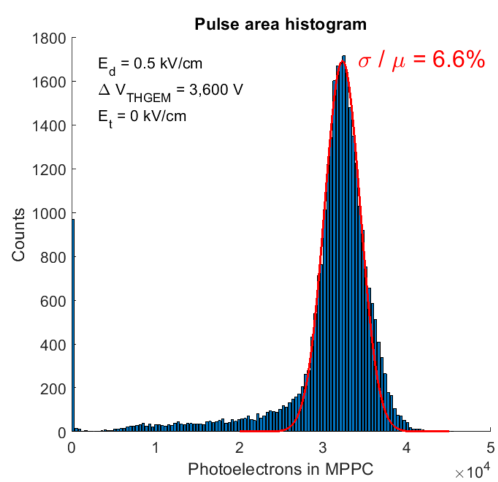

Figure 48 Energy spectrum (pulse-area distribution) obtained by summing the Alpha particles' EL-induced charge, recorded on all four SiPM pads.

6.3.2.2.2 Imaging of ^{241}Am with the Quad-SiPM array

In the detector geometry shown in figure 2, electrons are deposited within a few tens of µm from the surface of the alpha source; each event-induced electron-swarm drifts along the field lines (under E_d) towards the nearest hole (and splits rarely into two or three holes). The expansion of the electron swarm due to diffusion during its drift from the interaction point to the LHM electrode is negligible (in this particular setup) as the RMS deviation is 80 µm [3]. Longitudinal diffusion is one order of magnitude smaller. Therefore we expect obtaining an image of the hole pattern with a general shape of the ring-shaped alpha source (shown in Figure 50a). The EL occurs along the entire electrons' drift path in the bubble. At zero transfer field, the electrons' trajectories, after crossing the liquid-gas interface at the bottom of hole, are deviated along the field lines towards the electrode's bottom face. This lateral movement causes EL-photons emission along their entire path, thus somewhat blurring the holes' image.

Therefore, to obtain a well-resolved image, we have proceeded as follows: a) an intense transfer field was applied, causing the electrons to drift within the bubble towards the wires grid and enhancing the photoemission along the entire trajectory, and b) performing the COG computation only for the first part of the EL emission, that originating from the vicinity of the liquid-bubble interface. This trajectory is best depicted in the results presented in Figure 49. The figure presents six different time slots along the trajectory of the electrons from the hole bottom to the wires. The right part of each time slot presents the averaged pulse shape, the black strip represents the time slot on which the integration (i.e. the area under the curve) was computed and to which the COG distribution was computed. The left part represents the histogram of the center of gravities. Image (a) is obtained when the electrons have just passed through the hole. The slightly worse position resolution (comparing to the next two) is probably due low amount of light detected at this stage. The next two images (b and c), clearly present the hole pattern and the ring shape of the source. In part (d), one can already observe that the ring structure starts to deform into strips, which are caused by the heating wires; indeed the integrated area is already in the "secondary pulse", i.e. the pulse created near the wires. Pictures (e) and (f) are only due to EL generated on near the wires, showing straight lines as expected. When comparing (d), (e) and (f), one can also observe the magnification of the COG image as the electrons travel closer to the readout array. Reconstruction of the image at the correct length scale would require calibration and scaling of the COG images accordingly.

The best hole pattern we could achieve is shown in Figure 50b, and is a result of computing the COG over the first 450 ns (hole-bottom vicinity) of the pulses shown in Figure 47b. It reproduces well, qualitatively, the shape and some details of auto-radiographic source image (Figure 50a) recorded by a Fuji phosphor-imager scanner (model FLA-9000, plate model BAS-TR2040S). The 4.5 x 10^5 waveforms forming our SiPM-LHM image were recorded (over ~5 hours) with $E_d = 0.5\,\mathrm{kV/cm}$, $\Delta V_{THGEM} = 2.1\,\mathrm{kV}$ and $E_t = 12\,\mathrm{kV/cm}$. The THGEM-electrode holes are clearly apparent, with their reconstructed locations of 0.7 mm spacing between their centers.

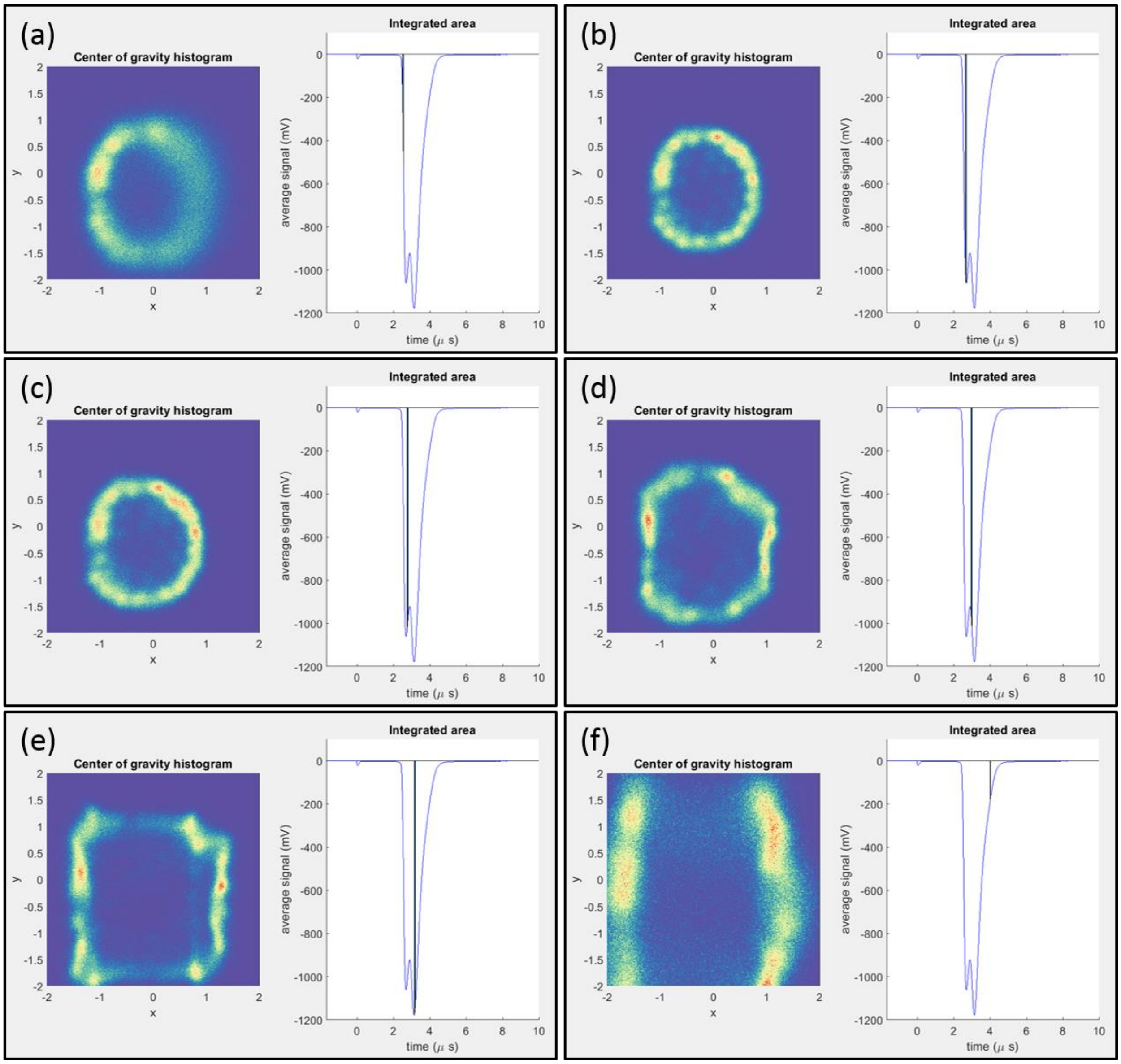

Figure 49 In each box, right presents (as a black strip) the time slot of the pulse which was integrated. Left presents a histogram of the resultant COGs. Data recorded with: $E_d = 0.5\ kV/cm$, $\Delta V_{THGEM} = 2.1\ kV$ and $E_t = 12\ kV/cm$. Each time slot is 50 ns long.

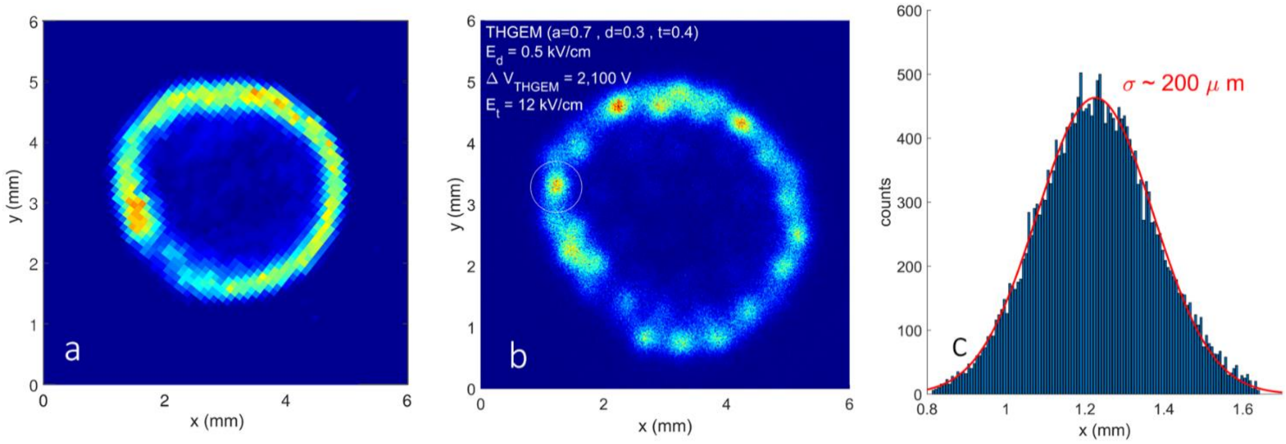

Figure 50 (a) the auto-radiographic Alpha-source image, recorded with a Fuji phosphor-imaging plate; (b) 2D histogram of the EL photons emitted at the vicinity of the liquid-gas interface, recorded with the Quad-SiPM LHM detector; the holes' pattern of the THGEM electrode is well resolved; (c) projected COG distribution across the x-axis, of the encircled hole in b), with a Gaussian fit to the data.

As explained above, the overall image granularity is dictated by the holes spacing and their diameter, however the resolution of the COG position reconstruction can be determined by observing the light distribution within an individual hole. We consider for the purpose of this analysis the light of a single hole as a point source, which will give an upper bound on the distribution width. More advanced analysis methods are the subject of further systematic studies. The projected COG distribution across the x-axis of the encircled hole in Figure 50b is depicted in Figure 50c. This hole was chosen, being well separated from the neighboring ones (probably due to the interplay between the hole pattern and the activity pattern of the source). The COG distribution was fitted with a Gaussian, yielding a resolution of ~200 µm RMS.

6.3.2.2.3 Imaging of 5.9 keV X-ray source

The study presented above was done with 5.5 MeV alpha particles. However, imaging studies of low-ionizaion events (e.g. few-keV DM-induced recoils in LXe) are of high relevance for evaluating the SiPM-LHM applicability in future large-volume rare-event experiments .Therefore, we demonstrated briefly the localization properties with a lower-ionization source – 5.9 keV X-rays from ^{55}Fe. As opposed to the ^{241}Am imaging, we had no a priori knowledge of the source's activity pattern apart from the containment of the activity to ~4.5 mm diameter, with no information about the activity distribution. The results shown in Figure 51, thus suggest position resolution in the few mm scale.

The pulses from the four SiPM units were added, the area under the pulse was computed and was normalized to the area of a single photoelectron signal in the SiPM. The resultant spectrum is shown in Figure 52. A Gaussian fit was applied to the peak, from which the energy resolution was derived. It is interesting to observe that while the ^{241}Am alpha particles energy resolution was ~6%, here, with ~45 times less charge we observe a resolution which is only a factor ~2 worse. The bump to the right of the main peak is probably due to pile-up events as the source's activity is very high. Further studies are needed to verify this assumption.

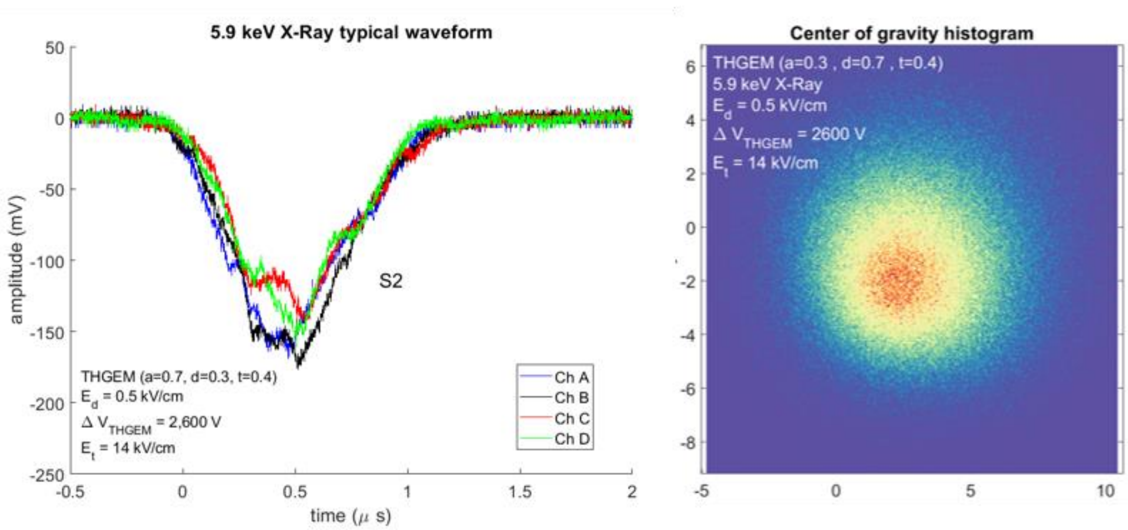

Figure 51 Left: typical waveforms of 6 keV X-ray photons as recorded from the four SiPM pads. Right: Event position reconstruction histogram.

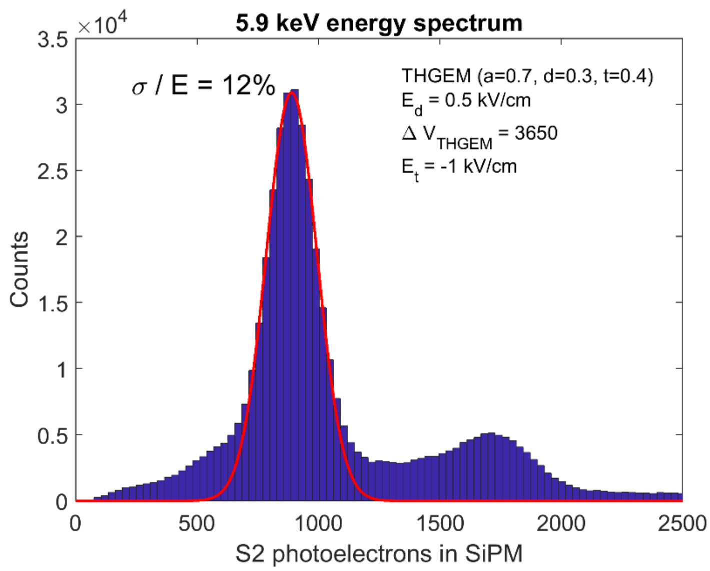

Figure 52 Energy spectrum for 5.9 keV X-rays.

6.3.2.2.4 Discussion

These first encouraging results call for further investigations of the electrodes geometry and that of SiPM elements, operation parameters, and COG-derivation algorithms.

As stated above, the overall image granularity depends on the hole pattern, which acted here as a "lens" for the source-induced ionization electrons in LXe. In this particular setup, with 200 µm resolution, it seems to be the largest factor affecting overall imaging resolution. Thus, the use of electrodes with finer hole diameter and pitch (e.g. GEM-LHM [52]) would result in smaller deviation of the event-deposited electrons from their original location; this will naturally enhance the event's location reconstruction. Also, since the wire grid generates a non-uniform field below the electrode, a better image resolution could perhaps benefit form replacing the wire grid with a uniform electrode (e.g. quartz plated with a thin transparent metal layer). This could better direct electrons downwards, prevent lateral movement around the wire and avoid the shadowing effect that the wire has on part of the EL pulse. Eventually, demands on imaging resolution could be relaxed when comparing the readout resolution to the smearing of the signal expected from electron diffusion. For 2.7 m drift in LXe (which is expected for the DARWIN observatory [22]) and for 12 m drift in LAr (expected in some detectors in DUNE [14]), electron diffusion is expected to be of the order of $\sigma \sim 3\ mm$.

Finally, the simple COG method employed here, is far from being ideal for event-location reconstruction. It is quasi-linear at the center of the present small-area Quad-SiPM array, up to half the size of an individual segment, distorting the image at larger distances. Other methods such as iterative position weighed COG algorithms [67, 68] or statistical methods, such as Maximum Likelihood or Least Squares algorithms [68, 69] are expected to provide better linearity and a more robust position reconstruction. These will be part of future studies (out of our current scope), with a larger detector and SiPM array and optimized inter-element spacing.

6.4 Design, manufacturing and commissioning of WISArD LAr cryostat

In order to investigate the LHM detector in LAr and in order to investigate the idea of a cryogenic RPWELL in the vapor phase of a LAr (see Appendix), a new LAr cryostat has been designed, constructed and commissioned during the course of this work.

The cryostat is shown in Figure 53. It is a custom made double walled, vacuum-insulated, chamber (100 mm in diameter, 150 mm tall) with three welded viewports. One allows for horizontal view on the setup, the other two are tilted by 30° with respect to the horizon.

Similarly to MiniX, the system can accommodate a variety of detector assemblies both immersed in the liquid and in the vapor phase above the liquid. Schematic representations of the RPWELL assembly is shown in Figure 53. It is able to accommodate detector prototypes up to 35 mm in diameter. A method was developed (Figure 54) for detectors requiring precise control over the liquid level (such as classical dual-phase TPC or vapor-phase RPWELL). This includes a Pyrex cup into which the liquefied Ar drips from the condenser, and in which the detector assembly is placed. The cup has a hole on its side, such that the liquid level is kept constant at the bottom part of the hole. The excess liquid is pumped out for purification after it has spilled off the Pyrex cup. The height of the cup with the respect to the detector is set by two threaded rods onto which the cup is fastened. This mechanism allows to practically control the height of the liquid level with respect to the detector (see Figure 54).

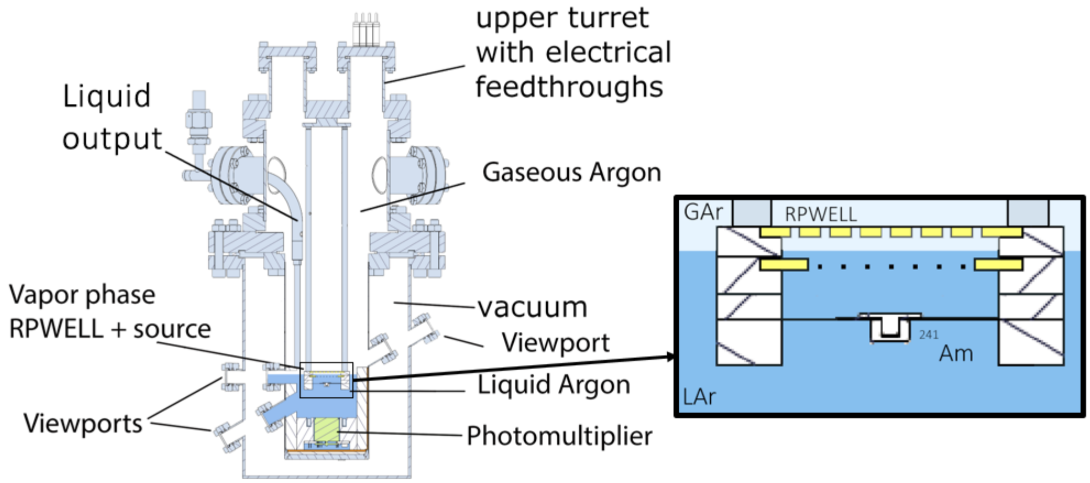

Figure 53 Schematic sketch of WISArD LAr facility. Three viewports allow better visual inspection and control over the experiment. Vapor phase RPWELL and source (enlarged on the right side) are shown here as an example for a detector hanging from above.

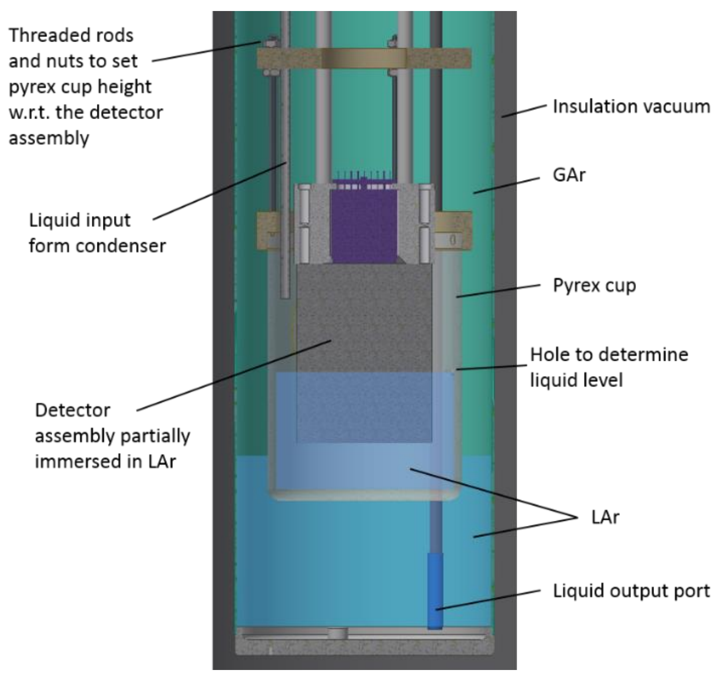

Figure 54 Schematic view of Pyrex cup to set the liquid level with respect to the detector.

Argon liquefaction is done on cooling fins cooled by a Cryomech PT90 pulse tube refrigerator. The design of the condenser (shown in Figure 55) is an adaption of the blue prints shared with us by Dr. Hanguo Wang from UCLA. It consists of copper cooling fins, attached to a block of copper, whose temperature is maintained constant on one hand by the pulse tube refrigerator and on the other hand by two 50Ω resistor, one with constant adjustable bias and one biased via a closed-loop feedback using a CryoCon temperature controller (Model 24).

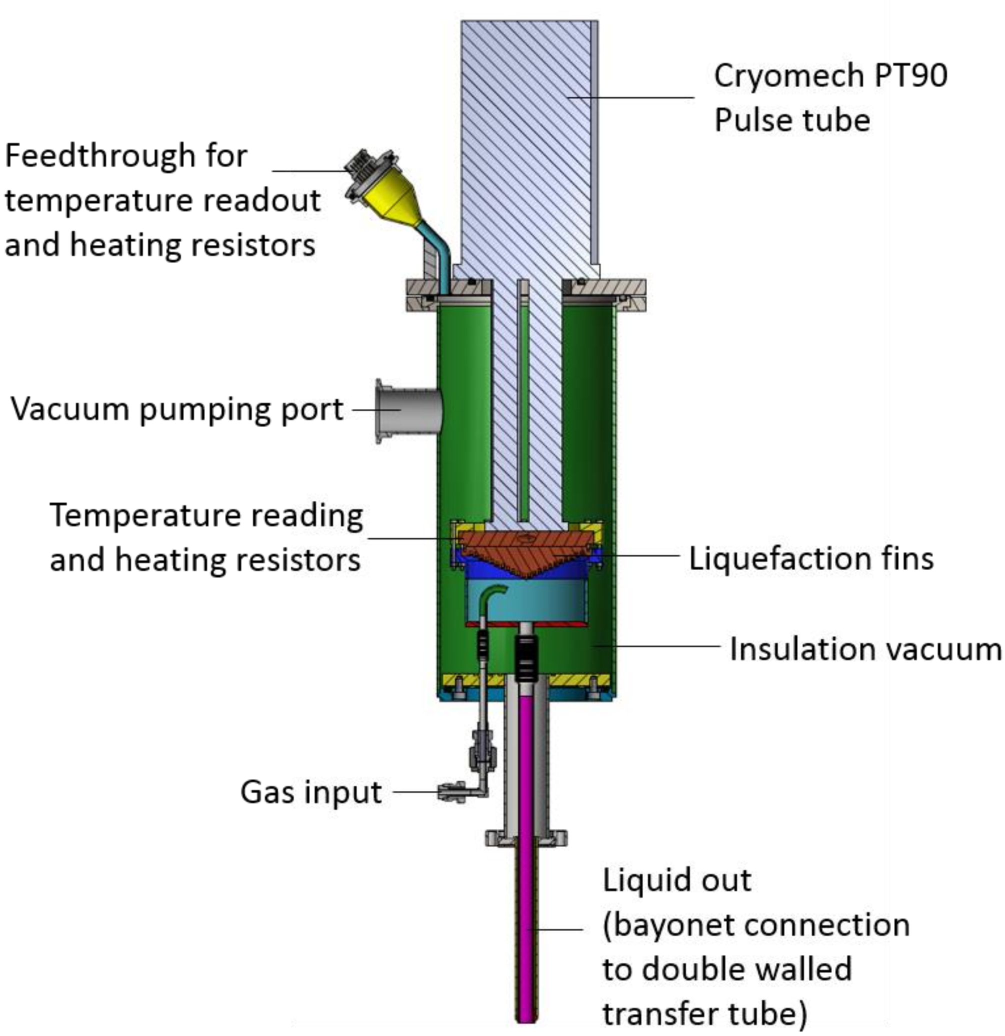

Figure 55 Sketch of the cross section of the condenser assembly.

The liquefied argon flows from the condenser through a 1.5 m long double-wall, vacuum-insulated transfer tube into the chamber. During operation, LAr is continuously extracted through a tube immersed within the liquid, evaporated in the stainless steel tubes and circulated using a double diaphragm recirculation pump (KNF N143) through an SAES hot getter (PS3-MT3-R) at 0-5 standard liters per minute. Flow rate is read and controlled by a mass flow controller (Aalborg GFC17S-VCL2-AO). The purified Ar gas returns to the liquefaction fins where it is liquefied and is let to flow back into the chamber. A complete sketch of the gas handling system is depicted in Figure 56. The figure shows as an example the valves configuration for liquid recirculation (white – open valve, black – closed valve) and the red arrows indicate gas flow through the tubes.

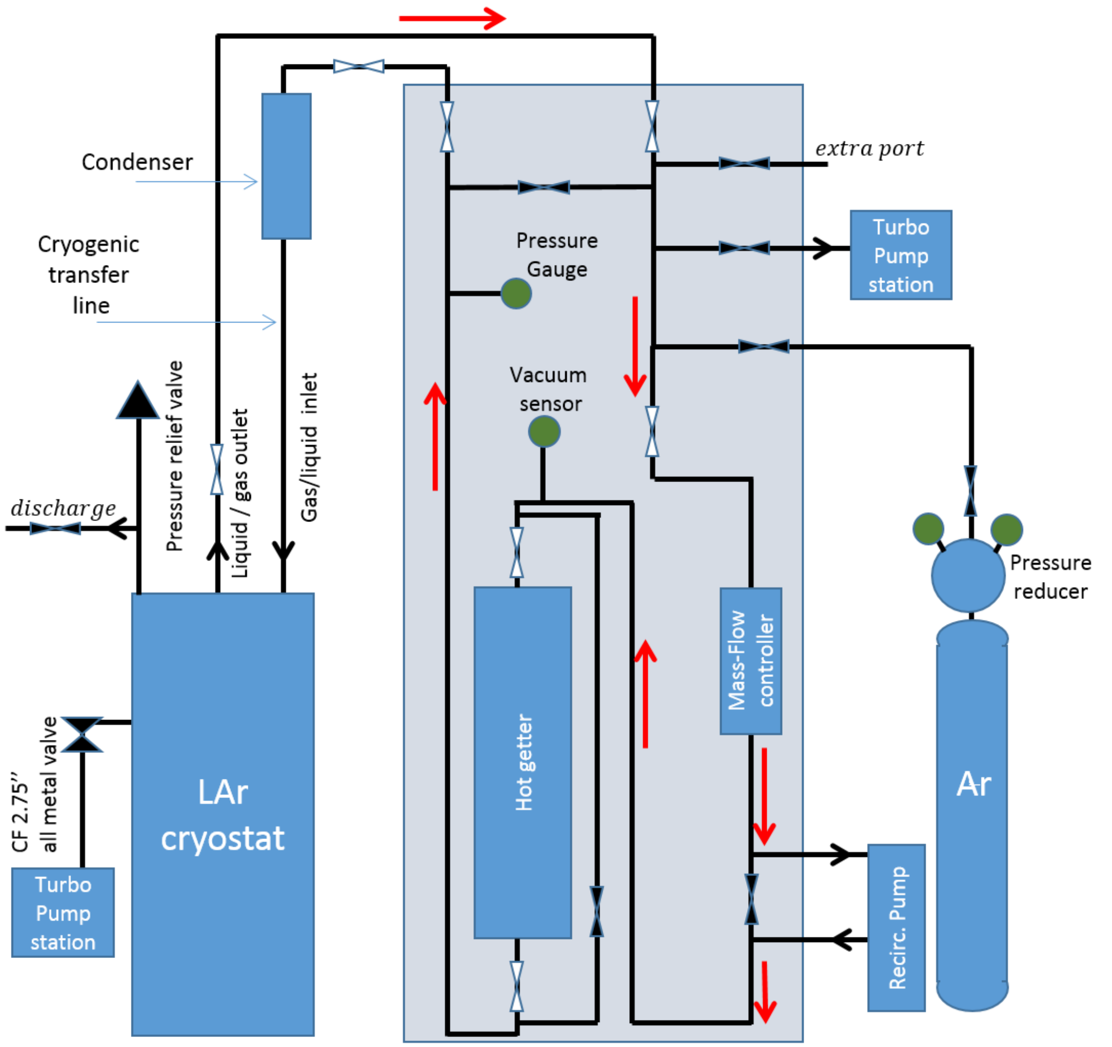

Figure 56 Schematic view of the gas handling system for WISArD. Valves are set up as an example for liquid/gas recirculation (white valve – open, black valve – closed) and red arrows indicate flow of gas in the tubes.

6.5 First demonstration of LHM in LAr

6.5.1 Experimental setup and methodology

The experiments were conducted in the WISArD cryostat described above. The LHM detector assembly is shown in Figure 57. It consists of a 0.4 mm thick THGEM electrode (hexagonal holes pattern 0.3mm in diameter, 0.7 mm apart). In this proof-of-principle study, the THGEM electrode was not coated with CsI, making the detector sensitive only to ionization electrons. Note that although a THGEM is not the best electrode in terms of light yield and of photon detection efficiency (as described in details in [52]), it was chosen for this first demonstration for its mechanical and electrical robustness. A ^{241}Am alpha source was placed 4.7 mm above the THGEM electrode. The source had an activity pattern of an annulus ~0.5 mm broad and ~3.9 mm in diameter with total activity of ~190 Bq (see [70] for details). A grid of heating wires (Ni-Fe, 55 µm in diameter, 2 mm spacing) was placed 1.6 mm below the THGEM. It was used to generate the bubble and to define the "transfer field" (E_t), i.e. the field between the bottom face of the THGEM and the wires. For convenience, we will quote the values of the transfer field as if it was a parallel plate between the bottom face of the electrode and the heating wires; this is only indicative, as the actual electric field is non uniform, being high close to the bottom part of the THGEM hole and next to the wires [52] and lower in the gap between them.

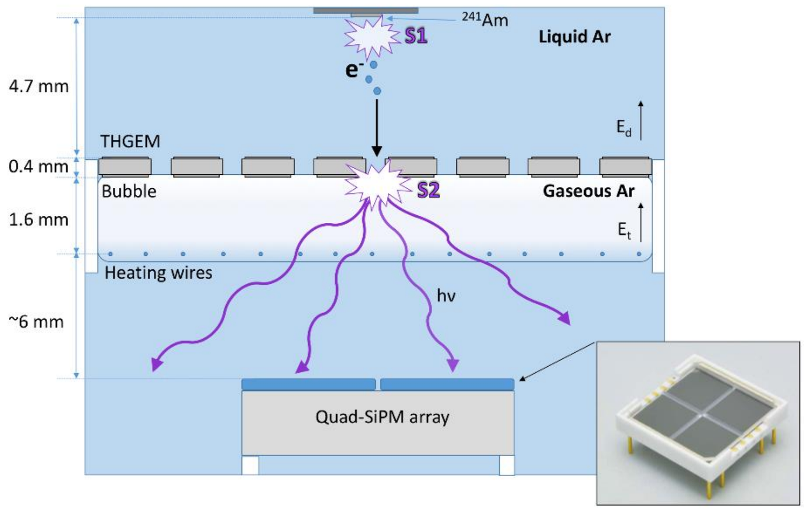

Figure 57 Schematic view of the experimental setup. A 0.4 mm thick THGEM electrode (with 0.3 mm in diameter holes spaced by 0.7 mm) is immersed in LAr; the gas bubble underneath is formed by a grid of heating wires, spaced 2 mm apart, located 1.5 mm below the electrode. Photons were recorded either by a PMT or by a Quad-SiPM array (shown here), located at ~6 mm under the wire grid. Ionization electrons focused into the holes induce EL light (S2) in the bubble; a fraction of the primary scintillation photons (S1) traverses the holes and is detected as well. In a second experiment, the SiPM array is replaced by a PMT.

The experimental setup was assembled on the suspension from the top flange, following which it was carefully introduced into the cryostat. The chamber was pumped down using a turbo-molecular pump to a pressure $< 10^{-4}\ mbar$. It was then filled with GAr through the hot getter. Liquefaction and filling of the chamber takes ~8 hours. After the filling, the LAr was circulated through the hot getter for more than one day before measurements started. In this setup, the bubbles under the electrode were generated spontaneously due to heat leaks (see [53]) and therefore did not require using the resistive wires.

Readout of the prompt alpha-induced scintillation photons and that of the electron-induced EL photons (WL~128nm) was done by direct digitization of the signals from the photosensors, located below the wire grid, using a Tektronix (MSO 5204B) oscilloscope. Two photosensors were used for recording the EL photons : (1) a PMT (Hamamatsu R8520-506) vacuum-coated with ~300 µg/cm² of TPB (Tetraphenyl butadiene) wavelength shifter and operated at -800 V. The PMT has a fast response and therefore allows for signal shape reconstruction. It was placed ~4 mm below the wire grid. (2) A four-elements windowless SiPM (Hamamatsu VUV4 MPPC S13371-6050CQ-02, 2x2 array of 6x6 mm² each spaced 0.5 mm appart); the quad-SiPM permitted 2D event-position reconstruction. It was located ~6 mm below the wire grid. The SiPM was operated at -46V as per the manufacturer's recommendation. However a full study of its operation at cryogenic temperatures has not yet been performed. Therefore, the resolutions quoted here are preliminary and may improve in future work.

The recorded waveforms were analyzed using dedicated Matlab scripts. Position of the event was reconstructed by a center-of-gravity technique as described earlier and in [70].

6.5.2 Results

As previously shown in LXe [46], also in this LAr setup, the EL signals disappeared upon sudden rise in the pressure and reappeared immediately after its sharp decrease. While not being able to visually see the bubble in the present setup, this confirms its existence and the generation of EL in it. All measurements were conducted at a liquid temperature of 90K, corresponding to a pressure of 1365 mbar [18].

6.5.2.1 Typical signals

With the LHM detector polarized to $\Delta V_{THGEM} = 3{,}000V$ (keeping $E_d = 1\ kV/cm$ and $E_t = 0\ kV/cm$), typical signals as recorded with the TPB-coated PMT are shown in Figure 58; Figure 59 depicts signals recorded from the four SiPMs' pads. The green marked pulses are that of the fraction of primary scintillation light infiltrating through the THGEM holes (S1); the red ones originate from the EL photons generated within the bubble (S2). One can observe a longer S2 decay constant (3-4 µs) compared to that in LXe (e.g. see Figure 8). This is explained by the long decay time of the triplet states GAr-EL as reported in [71]. The observed difference in S1 height with respect to S2 is due to the single electron response of the SiPM, being exponential with some ~200 ns decay time, compared to the PMT which has a sharper (~10 ns) Gaussian-like response.

6.5.2.2 Energy resolution

For each event, the pulse area under each waveform was computed and a pulse-area histogram was plotted. An example recorded with $\Delta V_{THGEM} = 3{,}000\ V\ E_d = 1\ kV/cm$ and $E_t = 0\ kV/cm$, recorded with the PMT at liquid temperature of 90° K is shown in Figure 60. A Gaussian fit was applied for deriving the resolution and the mean value.

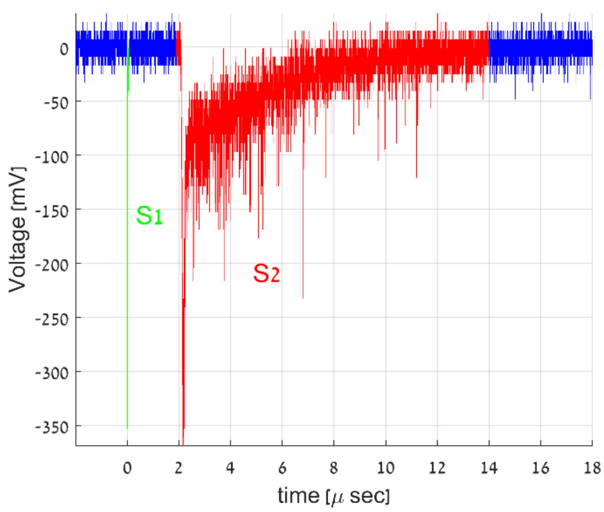

Figure 58 Example of alpha-particle induced single-event waveform, recorded by the TPB-coated PMT.

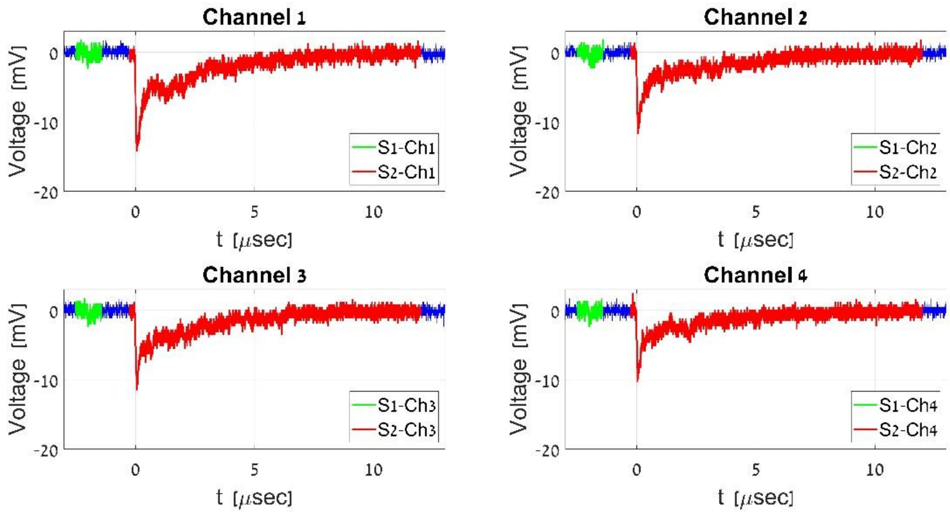

Figure 59 Example of alpha-particle induced single-event waveforms, recorded in the LAr-LHM setup of Fig. 2, by the four SiPM pads. V_{SiPM}=-46V

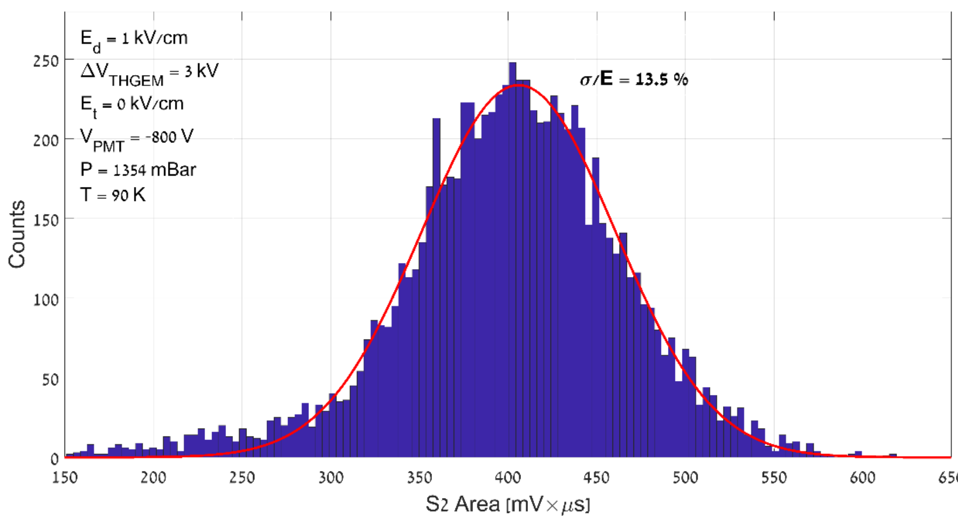

Figure 60 Area distribution of alpha-particle induced EL pulses recorded with the PMT, in the LAr-LHM setup at $\Delta V_{THGEM} = 3{,}000\ V$ $E_d = 1\ kV/cm$ and $E_t = 0\ kV/cm$, at temperature of 90°K. A Gaussian fit was applied to the data, for deriving the mean value and the RMS resolution.

Figure 61a shows the pulse-area as a function of the voltage across the THGEM electrode (keeping $E_d = 1\ kV/cm$ and $E_t = 0\ kV/cm$) and Figure 61b shows the RMS resolution as recorded with a PMT. Figure 62 presents the same configuration as recorded with SiPM pads. The linear trend shown in Figure 61a indicates EL without charge gain [3]. The RMS resolution was measured to be 13.5%. This value is ~2-fold worse than the one achieved in LXe; it should be considered preliminary and requires additional studies. Similar response (linear trend and resolution) to that measured with the TPB-coated PMT was confirmed with the windowless quad-SiPM.

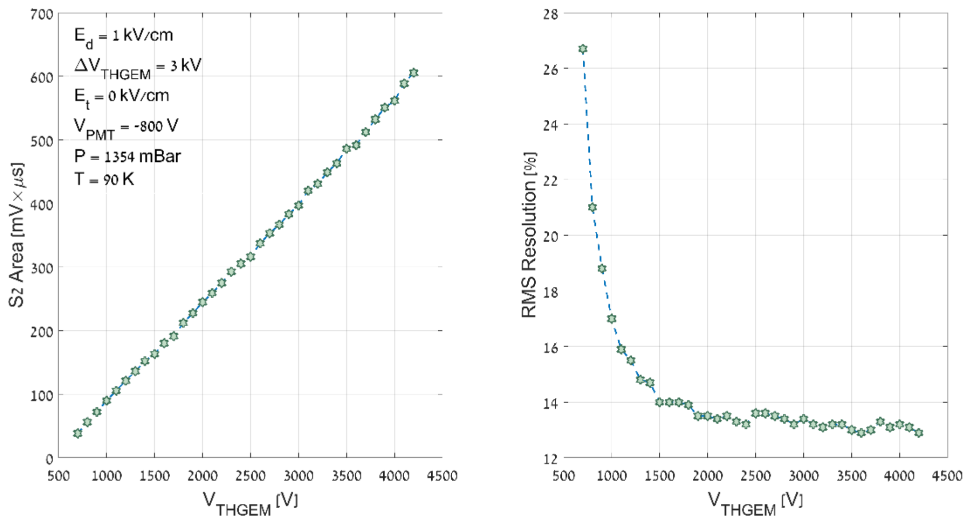

Figure 61 Response of the PMT to alpha particles, of the LAr-LHM detector. a) S2 mean area as a function of the voltage across the THGEM electrode. (b) RMS resolution of the area distribution.

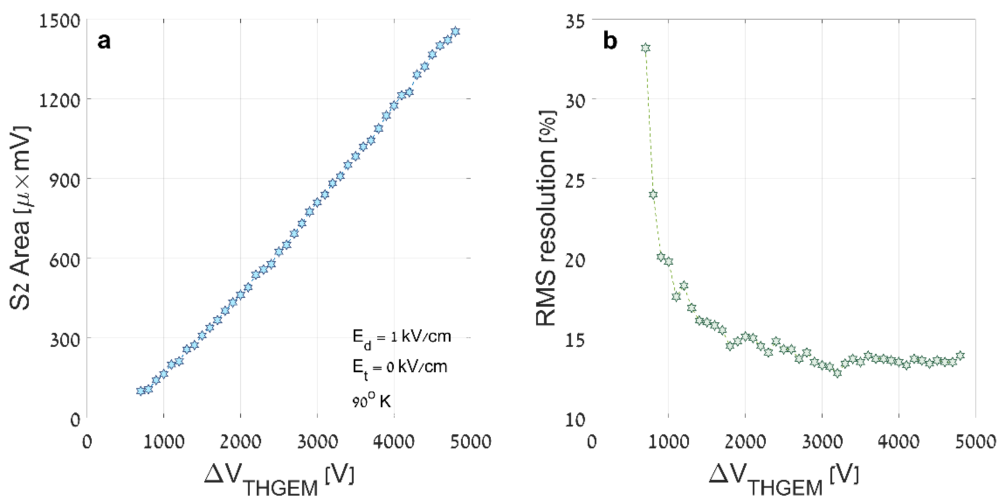

Figure 62 Response of the addition of the four SiPM pads to alpha particles, of the LAr-LHM detector. a) S2 mean area as a function of the voltage across the THGEM electrode. (b) RMS resolution of the area distribution.

6.5.2.3 Amplification in the transfer gap

As discussed earlier here and in details in [46] and in [52], the light yield can be boosted by increasing the electric field between the bottom of the THGEM electrode and the heating wires beneath (E_t). At moderate values of E_t (~2 kV/cm), this results in EL generated at the vicinity of the heating wires in addition to the one occurring mainly at the bottom of the holes as is explained in detail in section 6.1.2.3. At more intense fields, the electrons generate EL all along their path within the bubble: from the bottom of the hole to the wires. Figure 63 shows the average pulse-shape obtained at different E_t values. One can clearly see the addition of a second EL pulse, occurring ~0.5 µsec after that originating from the vicinity of the THGEM hole; it results in a significant increase in signal magnitude.

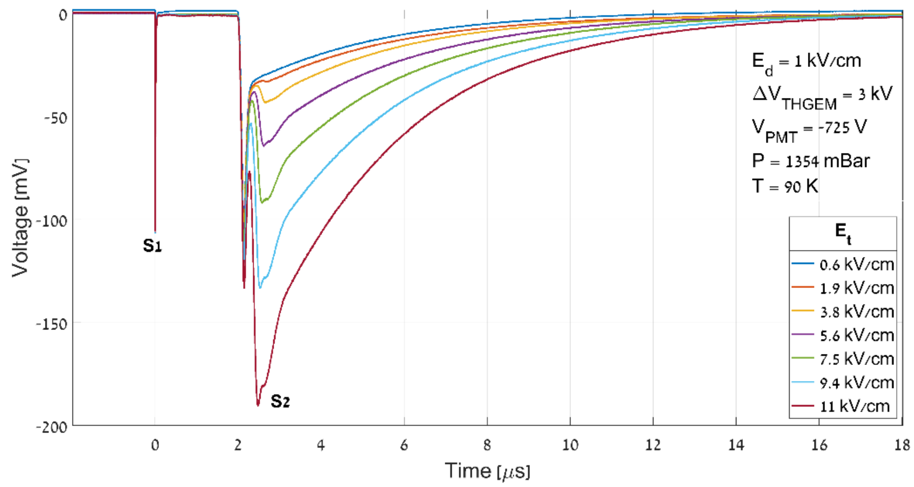

Figure 63 Average pulse shape recorded by the PMT from the LAr-LHM detector, at different values of the transfer field, E_t. $\Delta V_{THGEM} = 3{,}000\ V$ and $E_d = 1\ kV/cm$.

An example of the resulting pulse-area spectrum recorded with the PMT with E_t = 15 kV/cm is shown in Figure 64. It is interesting to observe that at such high E_t value, since the photon sensors here are self-triggered (as opposed to LXe experiments, where a second PMT was used to trigger only on alpha particles events) pulses resulting from the 59.5 keV gamma particles (emitted by the ^{241}Am) become visible. The data were recorded here with $V_{PMT} = -725\ V$ to avoid signal saturation. One should notice that although the gamma- and the alpha-particles differ in their energy by almost two orders of magnitude, their response in the LAr-LHM detector differ only by a factor ~4.5. This is due to the known different recombination probabilities of the ionization electrons, between the dense alpha-induced ionization and sparse density of electrons induced by the gamma-rays [2, 3].

The peak position of the Gaussian fit is depicted in Figure 65, as a function of E_t. One can clearly see that above ~4 kV/cm, the pulse-area grows exponentially, indicating upon modest (~10-fold) charge-avalanche multiplication at the vicinity of the wires. As in LXe, the resolution here is immediately deteriorated with increasing transfer field. Possible explanation to this are similar to that offered for the results in LXe, namely avalanche statistics deteriorating resolution, electron trajectories differences and wire shadowing. Also, the relative instability of the spontaneously bubbles in the particular setup may contribute to worsening in the resolution. Further studies are needed to verify these hypotheses.

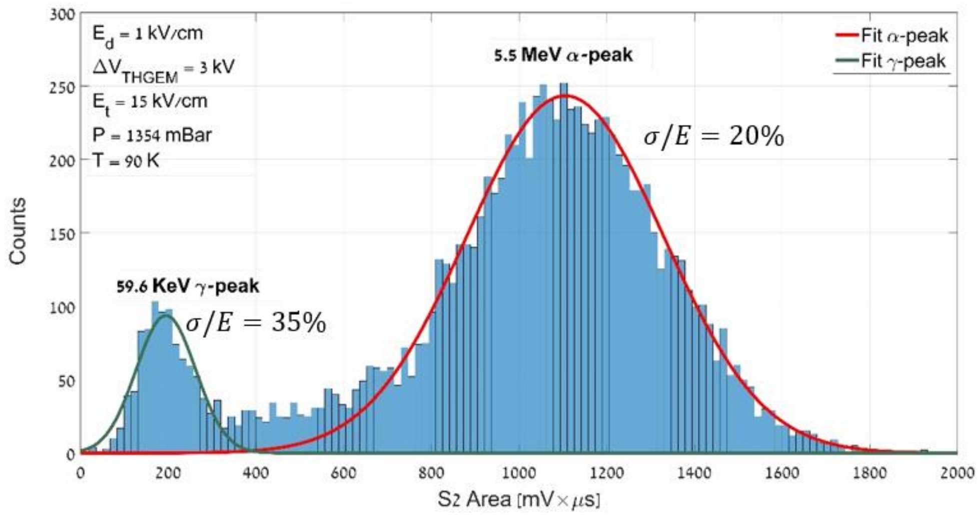

Figure 64 Pulse-area spectrum recorded by the PMT from the LAr-LHM detector with EL occurring in the THGEM holes, in the transfer gap and near the heating wires. One Gaussian fit (red) corresponds to the 5.5 MeV alpha particles and the second one (green), to the 59.5 keV gamma interactions in LAr.

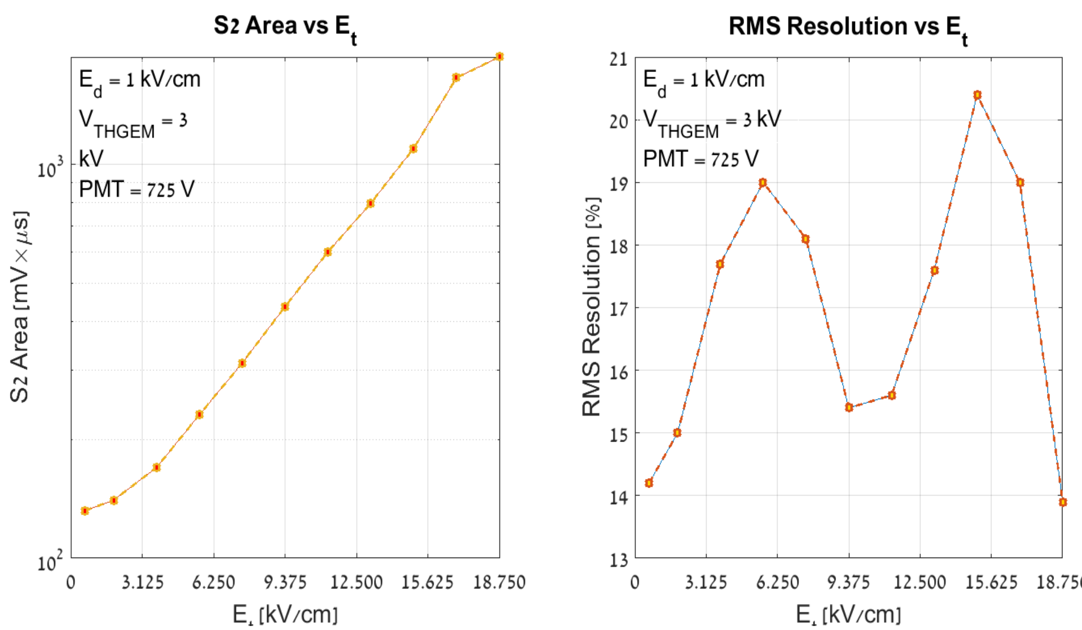

Figure 65 Signal magnitude of the alpha particle peak as a function of the transfer field. The exponential behavior indicates upon modest charge multiplication above E=~4kV/cm.

6.5.2.4 Position reconstruction

Similar to the methodology presented in [70], the integral of the pulse from each of the four SiPM pads was computed for each event. The event position was then reconstructed by a center-of-gravity method. An auto-radiographic image (using a Fuji phosphor-imager scanner model FLA-9000, plate model BAS-TR2040S) of the ^{241}Am alpha source used in our experiments is shown in Figure 66a. The 2D histogram of the derived event positions, recorded in LAr with the LHM (of Figure 2), is shown in Figure 66b. This very preliminary qualitative image reproduces the annular shape of the alpha source. However, the reconstruction resolution is, at this point, poorer in comparison to the ~200 µm RMS one (see Figure 50 above), recorded with LXe-LHM [70], calling for further investigations.

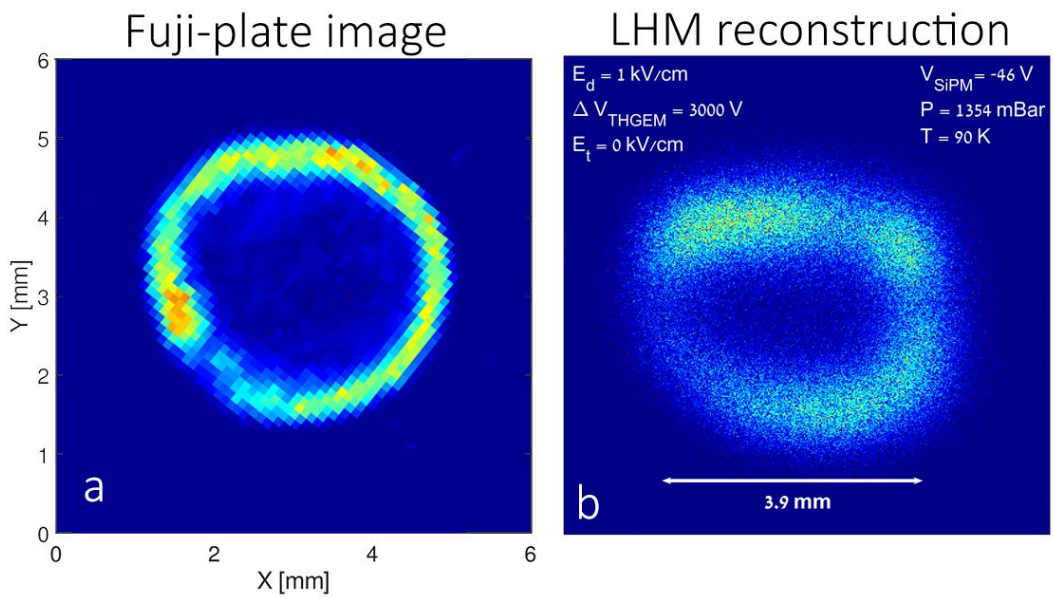

Figure 66 (a) The auto-radiographic Alpha-source image, recorded with a Fuji phosphor-imaging plate. (b) 2D histogram of the EL photons emitted at the vicinity of the liquid-gas interface, recorded with the Quad-SiPM LAr-LHM detector.

6.5.2.5 Estimation of light yield

Estimating light yield in LAr is not as straight forwards as it was in LXe. Both the SiPM array and the TPB-coated PMT where not thoroughly tested for their QE (or PDE). Therefore, calculations here rely on typical values as reported in literature. We therefore present both calculations which, as will be shown, agree within ~8%, detailing their weak points.

In order to estimate the effective light yield, one has to consider equation 6 given above in chapter 6.1.2.4 and adapt it to our case:

$$Y_{EL}^{eff} = Y_{EL} \cdot \varepsilon_{col} \cdot \varepsilon_{interface} = \frac{N_{PE}}{N_e \cdot P_{LHM \to SiPM} \cdot QE_{SiPM}} \qquad \text{Eqn. 14}$$

In order to compute N_{PE} one needs to normalize the pulse area of the detector to that of a single electron. Unfortunately, in this setup, we could not find a suitable voltage that would show single-electron pulses. The matter will be part of future investigation. For a first crude estimation, one could use the single-photon spectrum as measured in LXe (Figure 46). The error on the value is difficult to estimate.

Next, in order to estimate $P_{LHM \to SiPM}$, a MC simulation was written (similar to the one described in section 6.3.1). It was found to be $P_{LHM \to SiPM} = 0.2$ using the dimensions in Figure 57. For this computation, $n = 1.36$ was used as the diffraction coefficient [20].

The QE of the SiPM units was also not measured. We are therefore left to rely on the QE value provided by the producer: for 128 nm $QE = 14\%$. However at this short wavelength, surface contaminations may affect QE substantially. Also, the reported value has been measured at room temperature, with little knowledge of whether it remains so at 90° K [64].

N_e was estimated by taking into account the average energy needed to generate an electron-ion pair in LAr $W = 23.6\ eV$ [2] and taking into account the probability of an electron to escape recombination at 1 kV/cm $p = 0.02\%$ [2], resulting in $N_e = 4.8 \cdot 10^3\ e^-$. Finally, with all due prudency regarding the above discussed unknowns, we could compute $Y_{EL}^{eff} = \sim 160\ \ photons/e^-/4\pi$.

Similar computation can be done for the PMT signals. It results in an equation similar to Eqn. 14, with the slight addition of ε_{TPB} which is the efficiency for the wavelengthshifting of the TBP layer. With lack of any measured number for our evaporated PMTs, we assume here full shifting efficiency [72], and a factor 0.5 because photons are emitted isotropically from the TPB layer, thus $\varepsilon_{TPB} = 0.5$.

$$Y_{EL}^{eff} = Y_{EL} \cdot \varepsilon_{col} \cdot \varepsilon_{interface} = \frac{N_{PE}}{N_e \cdot P_{LHM \to PMT} \cdot \varepsilon_{TPB} \cdot QE_{PMT}} \qquad \text{Eqn. 15}$$

For the single-photon response of the PMT we can use the numbers quoted in section 6.2.6.2: $single\ photon\ area = \ 0.014\ mV \cdot \mu s$. From MC simulation, $P_{LHM \to PMT} = 0.4$.

$$Y_{EL}^{eff} \approx \frac{\frac{600}{0.014}}{4.8 \cdot 10^3 \cdot 0.4 \cdot 0.5 \cdot 0.3} = 148\ photons/e^-/4\pi \qquad \text{Eqn. 16}$$

6.5.3 Summary and discussion

Here, we have demonstrated, for the first time, the operation of an LHM detector in LAr. We have shown that similar to LXe, a bubble can be sustained for a long period under a THGEM perforated electrode immersed in LAr. EL within the Ar bubble, induced by ionization electrons deposited by alpha particles in LAr and collected into the electrode's holes, shows a linear response with the applied voltage, as expected in such process. Similar to results in LXe, electrons drifting within the bubble towards the heating-wires grid undergo modest charge-avalanche multiplication. Imaging of the alpha-particle induced EL photons was demonstrated, qualitatively, with the quad-SiPM.

It is clear from the above figures that the alpha-particle induced energy resolution on the LHM in LAr, is ~two-fold worse compared to that achieved in LXe. There are many parameters which may have contributed to that. First, ionization-electron yield in LAr is ~2-fold smaller than that in LXe [2]. This automatically means a reduction in total signal magnitude. Secondly the EL yield is known to be smaller in GAr than in GXe for a given field [3]. Also, the QE of the photosensors is ~twice lower at 128 nm compared to 175 nm, thus lowering the eventual statistics of detected photons. These are however still hypotheses pending further experimental validation. Of course, here again, the issue of electron transmission through the bubble interface is yet unknown and might have affected the detector performance.

It is also clear that the position resolution is far worse (estimated here to be in the mm scale) than in LXe (~200 µm). The reduction in signal magnitude as discussed above is one parameter which has an immediate effect on position resolution as discussed in section 6.3.1.5. To that, we should add that the fact that some electrons hop across the liquid to gas interface with a long timescale combined with the integration scheme we apply (only on the first part of the signal), may explain a further reduction in the "usable" fraction of the light signal. The latter effect could probably be improved by using more sophisticated position reconstruction algorithms. Finally, photons generated in the gas are refracted in when crossing the interface into the liquid before reaching the SiPM. Therefore, instabilities of the gas-to-liquid interface could affect photon refraction, thus effectively a widening the distribution resolution and contributing to smearing of the image. This could be solved by placing the SiPM array in the gas phase.

This preliminary demonstration paves ways towards a more elaborate and quantitative study of the bubble-assisted LHM detector in Ar. It would encompass the optimization of the perforated electrode geometry, study of the physical processes governing electron transfer through the liquid-gas interface, optimization of the readout (SiPM, PMT etc.) and of other parameters. We thus expect enhancing the (so far poorly calibrated) EL light yield and improving the energy resolution and localization resolution in LAr-LHM over a broader ionization range.

6.6 Double-Stage LHM in LXe

A first proof-of-principle of the cascaded LHM concept [45] is presented here. A double-stage detector was investigated in LXe, shown in Figure 67, incorporating two LHM elements, each having a bubble underneath to generate EL signals. In the spirit of the original LHM concept, radiation-induced EL photons from the first stage impinge on a VUV-sensitive photocathode deposited on the second hole-electrode – generating additional EL signals. This concept is similar to the "photon-assisted" cascaded detector developed for ion blocking in gas-avalanche detectors [28, 73]; it has the potential of reaching higher total photon yields ("gains") compared to that of a single-stage LHM. As previously suggested and demonstrated in the gas phase [74], such cascaded multipliers can also allow for gating the detector with an external trigger, on events of interest. We report here on preliminary results obtained with a double-stage LHM comprising two SC-GEM elements, with a CsI photocathode deposited on top of the second one.

6.6.1 Experimental Setup

The cascaded LHM setup (Figure 67) comprised two SC-GEM electrodes (a=300 um, d=150, t=50 um, note that they have different dimensions than the ones use in all above experiments); bubbles were formed underneath, generated by resistive wires located below each electrode. We refer to the inter-electrode gap and the gap between the second electrode to the wire-plane below as transfer gaps 1 and 2, respectively, with their associated nominal transfer fields E_{t1} and E_{t2}. As in the horizontal LHM setup (Section 6.1), the ^{241}Am spectroscopic alpha-particle source was located 5 mm above the first LHM electrode, and triggering on reflected S1 light was done by the top PMT; all EL signals were recorded by the bottom PMT, placed below the second SC-GEM electrode.

As depicted in Figure 67, following alpha emission from the source into the liquid, a fraction of the S1 photons are reflected off the PTFE walls, reaching the top PMT. A small fraction of the S1 light penetrates through both SC-GEMs, reaching the bottom PMT. Another fraction reaches the bottom, CsI-coated, SC-GEM2 electrode; the resulting emitted photoelectrons generate an S1' EL signal. The radiation-induced ionization electrons are focused into the holes of SC-GEM1, inducing an S2 EL signal. A large fraction of the resulting photons impinge on the photocathode of SC-GEM2; they extract photoelectrons that, in turn, generate another EL signal in the bubble underneath (S2'). A small fraction of the S2 photons emitted in the direction of the second electrodes (~18%) pass through the holes of SC-GEM2, reaching directly the bottom PMT. If a transfer field is applied between the two LHM elements, after generating the S2 signal, the ionization electrons drift to the SC-GEM2 element where they generate another EL signal (S3).

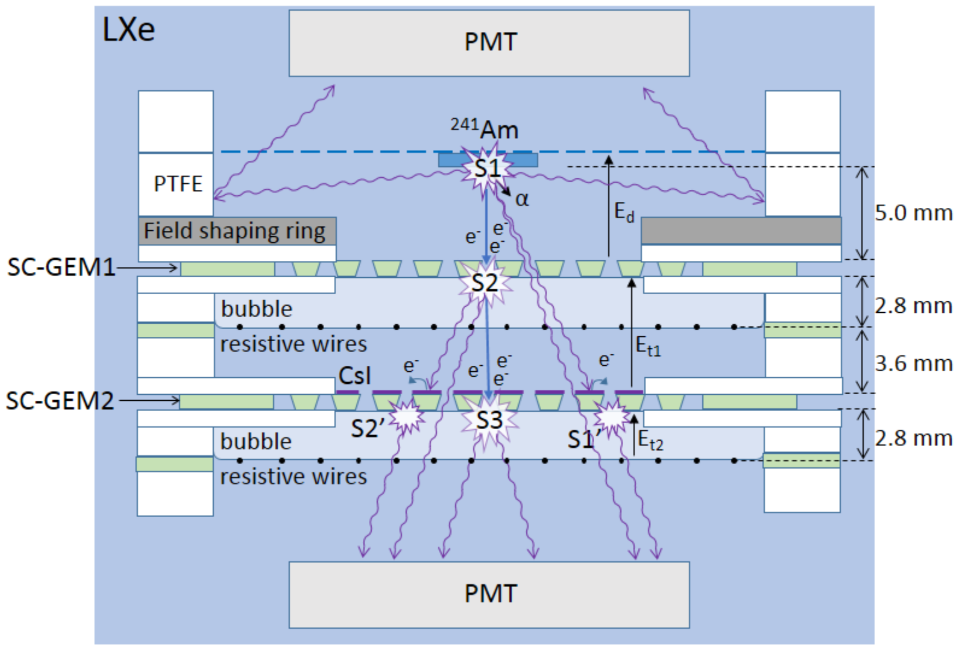

Figure 67 Schematic drawing of the double-stage bubble-assisted LHM setup and its operation principle. Two SC-GEMs have heating wire planes underneath, generating independent bubbles under each hole-electrode. Radiation-induced S1 photons are reflected off the PTFE walls, reaching the top PMT to provide a trigger signal. A small fraction of S1 photons penetrate through both SC-GEMs, reaching the bottom PMT. Another fraction reaches the CsI-coated SC-GEM2 electrode; the resulting emitted photoelectrons generate the S1' EL signal. The radiation-induced ionization electrons are focused into the holes of SC GEM1, inducing the S2 EL signal. A large fraction of the resulting photons impinge on the photocathode of SC-GEM2; they extract photoelectrons that generate another EL signal in the bubble underneath (S2'). A small fraction of the S2 photons emitted in the direction of the second electrodes pass through the holes of SC-GEM2 and reach directly the bottom PMT. If a transfer field is applied between the two LHM elements, after generating the S2 signal the ionization electrons drift to SC-GEM2, where they generate the S3 EL signal.

During the measurements it was noted that, in the current setup, after an occasional discharge in an SC-GEM electrode, its maximal achievable voltage dropped significantly. Despite initially-reachable values of 1300 V across an SC-GEM (in the single-stage measurements, Section 2.1), the maximal voltage per element along this preliminary double-stage study was limited to ~750 V – calling for a more careful detector polarization in future experiments.

6.6.2 Results

In the first set of measurements of the double-stage SC-GEM LHM, we studied the dependence of the light output of the structure on the voltage across the second electrode $\Delta V_{SC-GEM2}$, for a fixed voltage across the first stage $\Delta V_{SC-GEM1} = 700\ \mathrm{V}$, a fixed drift field $E_d = 1\ \mathrm{kV/cm}$ and transfer fields $E_{t1} = E_{t2} = 0$. Figure 68 shows an average of 10,000 waveforms recorded by the bottom PMT at $V_{PMT} = -700\ \mathrm{V}$, for several values of ΔV_{SC-GEM_2}. A small fraction of prompt scintillation photons (S1) traversing both electrodes reach the bottom PMT. The S1' signal is due to photons that passed through the first electrode, extracting photoelectrons from the CsI on the second stage and inducing EL in the second bubble. The S2 signal resulting from electron-induced EL photons in the first bubble is followed by S2' EL, due to S2 photons extracting photoelectrons from the CsI that induce further EL signals in the second bubble.

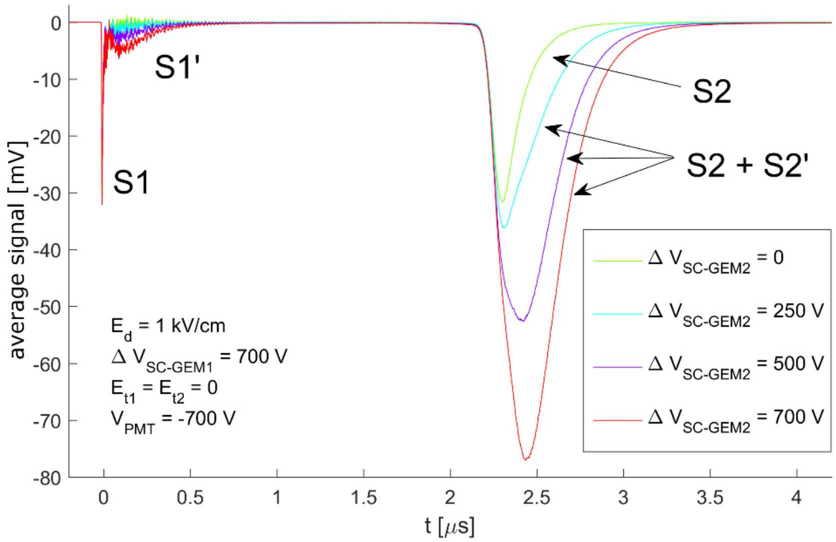

Figure 68 Averaged alpha-particle waveforms recorded by the bottom PMT in the double-stage, SC-GEM LHM setup (of Figure 5). Different colors correspond to different voltages applied across the second stage. EL S2 photons from the first stage induce the emission of further photoelectrons in the second stage. These generate additional EL S2' photons – thus amplifying the original signal.

For each waveform, the integral of the S2+S2' pulse was computed, deriving pulse-area histograms. An example is shown in Figure 69. A Gaussian fit was applied to the S2+S2' spectra, for which the mean and the RMS resolution are shown in Figure 70 as a function of $\Delta V_{SC-GEM2}$. At high voltages the behavior is linear; the curved response at lower voltages is due to increasing photoelectron extraction efficiency from CsI with increasing electric field at the LHM surface (as discussed in the PDE study and in [56]).

The effective gain of the second stage is defined to be the ratio between the combined S2+S2' pulse area and that of the first stage only (i.e., of a single-stage LHM configuration). When normalized correctly, we could compute the effective gain of the second stage to be ~1. When extrapolating the results of Figure 70A to $\Delta V_{SC-GEM2} = 1400\ \mathrm{V}$, one could potentially reach gains of ~2. This gain in light yield is much smaller than that obtained by applying an intense transfer field. However, the S2 RMS resolution appears to be better in the double-stage configuration: ~6% (and improving with $\Delta V_{SC-GEM2}$) compared to $> 9\%$ with transfer-gap amplification as seen in Figure 17. It is worth mentioning that maintaining the signal resolution of an optically-coupled two-stage gas-avalanche detector was also observed previously [73].

Under a transfer field applied between both stages, electrons drift from the holes of the first electrode to that of the second one, where they induce an additional S3 EL signal. Figure 19 shows an average of 10,000 waveforms recorded at different voltage values of the first stage. In addition to the S2+S2' signals which obviously increase in amplitude with the voltage applied to the first electrode, the S3 signal is clearly apparent. The energy resolution of S2 in these conditions is 10-11% for all voltages above 200V.

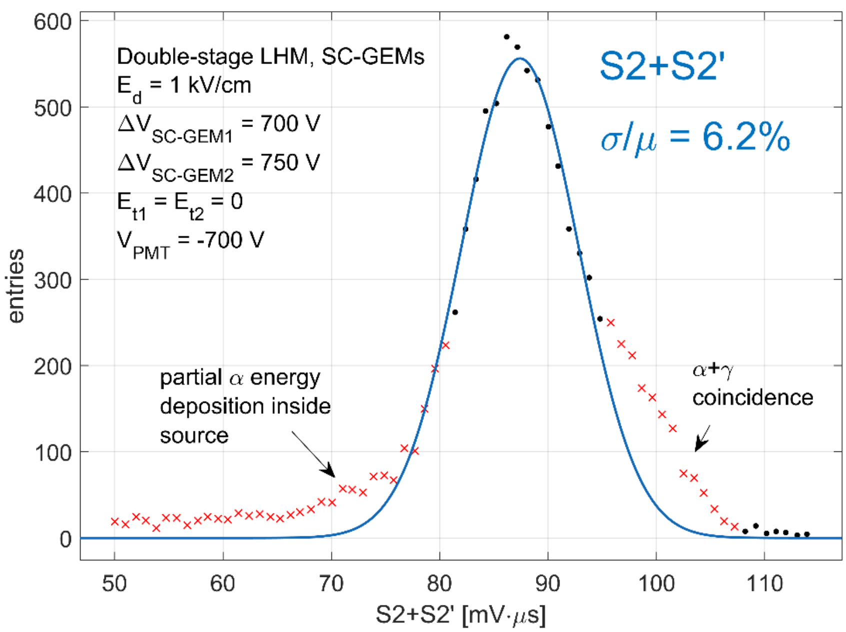

Figure 69 Double-stage SC-GEM LHM spectrum of S2+S2'. Data points in red were excluded from the Gaussian fit. The excess of events left of the peak is attributed to partial energy deposition by the alpha particle inside the source substrate, and that right of the S2 peak - to coincident emission of alpha particles and 59.5 keV gammas. The estimated number of ionization electrons entering the first LHM electrode is ~10,000

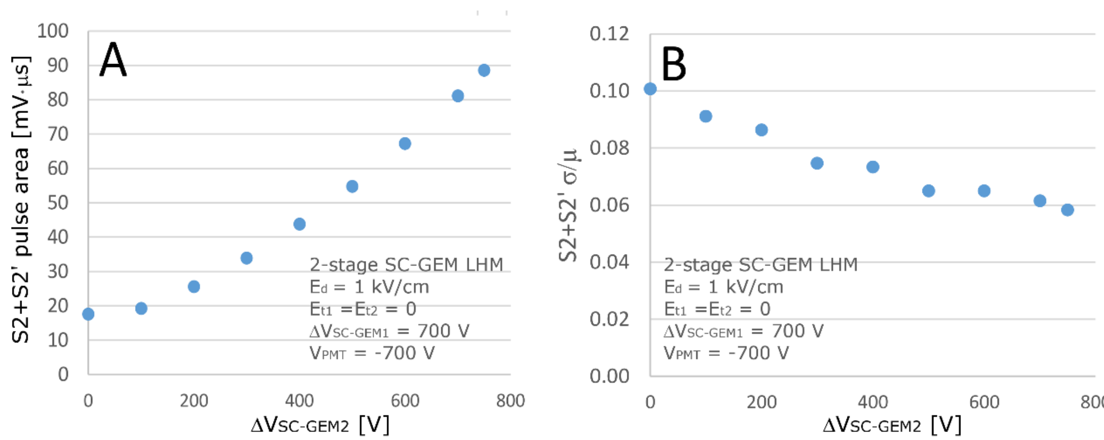

Figure 70 S2 + S2' pulse area and RMS resolution as a function of the voltage across the second amplification stage.

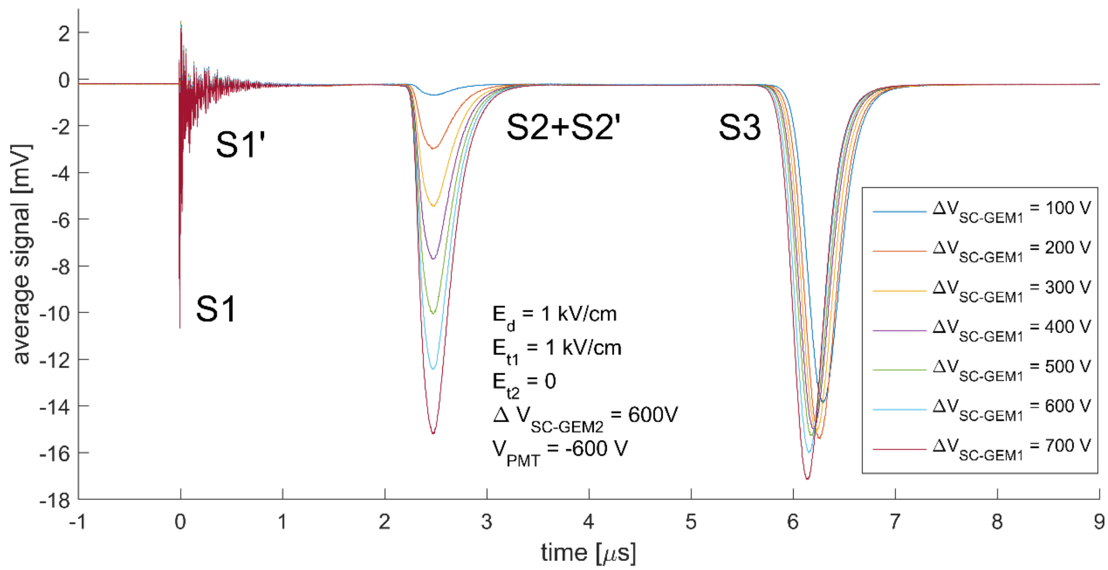

Figure 71 Average waveforms of pulses measured by the bottom PMT from the double-stage LHM, with electrons drifting all the way to the second SC-GEM electrode (under $E_{t1} = 1kV/cm$). The S1 and S1' scintillation signals are followed by ionization-electron-induced ones, giving rise to the S2+S2' signal; S3 signals, due to electrons reaching stage 2, show a small increase in the pulse-area with $\Delta V_{SC-GEM1}$; it could originate from small avalanche multiplication (~1.1) in the first LHM stage.

6.6.3 Discussion

While the results on the double-stage configuration are very preliminary, they provide a first demonstration that a cascaded structure with independent bubbles is indeed feasible. Although the present double-stage configuration is apparently limited to an overall EL amplification of ~2 compared to a single element - considerably lower than possible with a single-stage LHM with EL amplification in the transfer gap - it does show a very good (and possibly better) energy resolution. Furthermore, the overall EL yield can be in principle enhanced by the addition of one or more stages. A potentially useful feature of the cascaded structure is the possibility of gating its response – for example by momentarily reversing the transfer field between the first and second electrode. This can add a new degree of freedom to LHM structures, enabling selective switching between 'on' and 'off' states to detect desirable events and be 'blind' to others.

6.7 Vertical LHM

The basic concept of the bubble-assisted LHM relies on the ability to confine a bubble in contact with a hole-electrode such that electrons deposited and drifting in the liquid are efficiently focused into the bubble. This concept could in principle be realized not only by supporting the bubble underneath a horizontal electrode, as discussed above, but also by confining a bubble in a vertical "cage", of which one side consists of a hole-electrode and the other - of a fine mesh or transparent plate.

6.7.1 Experimental setup

The vertical LHM setup, shown in Figure 72, consisted of the spectroscopic ^{241}Am alpha-particle source positioned behind a bubble-confinement cage, comprising PTFE spacers, a GEM/THGEM and a fine-pitch electroformed Cu mesh (Precision Eforming MC-32; opening: 112 µm). A resistive heating wire was introduced through two small holes at the bottom of one of the PTFE spacers, to form the bubble on demand. The setup was placed inside the liquid volume, where the bubble could be observed at 60° with respect to the vertical axis of the cryostat through the window. Once the bubble formed, it displayed periodic dynamics of abrupt partial shrinking followed by gradual growth over the entire field of view, with a period of ~20 s. EL signals from the bubble were recorded by a PMT which was placed outside of the vessel at a distance of ~20 cm from the LHM, resulting in low light collection and thus in poor photon statistics. To obtain sufficiently large S2 EL signals, an intense transfer field was applied across the bubble.

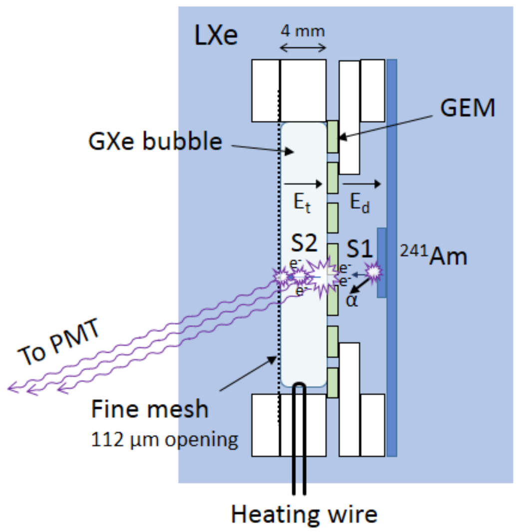

Figure 72 The vertical-LHM assembly for the confinement of a bubble between a vertical GEM electrode and a fine-pitch mesh (not to scale). PTFE spacers define a closed "cage" between the electrode and the mesh. A thin resistive heating wire is introduced through small apertures into the cage, to generate the bubble. To overcome the low light collection efficiency, S2 EL signals were amplified in the transfer gap by applying an intense transfer field across the bubble.

6.7.2 Results

Figure 73 shows a typical waveform recorded with $\Delta V_{GEM} = 900$ V, $E_d = 1$ kV/cm, $E_t = 15.5$ kV/cm and $V_{PMT} = -900$ V.

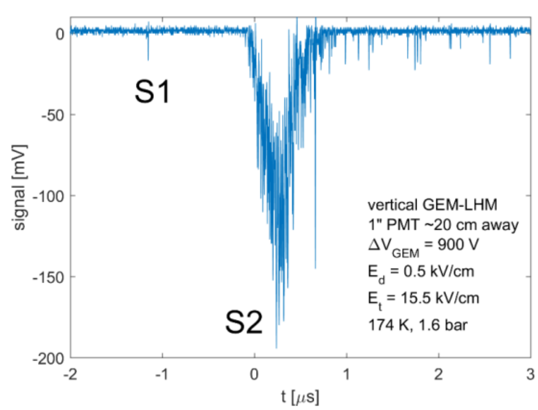

Figure 73 Single-event EL signal from the holes of a vertical bare standard-GEM electrode (without CsI) with a bubble sustained between the GEM and a fine-pitch mesh. Photon statistics are low because of geometrical constraints which forced placing the 1" PMT outside of the vessel ~20 cm away from the LHM.

Figure 74 shows the average pulse area and RMS resolution of the S2 signals as a function of E_t; for each value of E_t, 10,000 waveforms were digitized and processed. At the highest light yield recorded under these non-optimal conditions, the resulting RMS resolution of 11% is ~ 2-fold worse than that achieved with the horizontal LHM, however this is probably mainly due to the low light collection into the PMT at this specific setup.

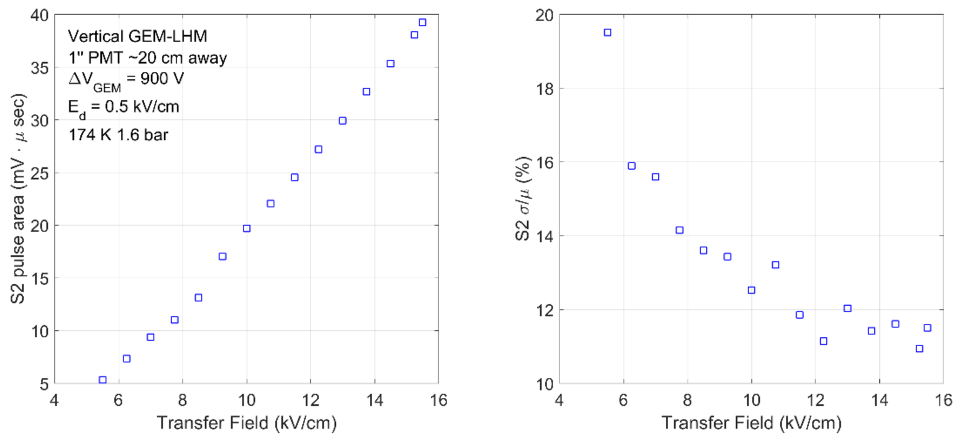

Figure 74 Vertical LHM with a standard-GEM. Relative S2 magnitude (A) and energy resolution (B) resulting from EL signals recorded from the vertical bubble confined between the GEM electrode and a fine mesh. The EL photons originate from the high electric field applied across the transfer gap.

6.8 Bubble between two meshes

6.8.1 Experimental setup

Another setup devoted to experiments of trapping a bubble between two parallel meshes was installed inside MiniX as depicted in Figure 75. Two PMTs recorded the alpha-induced signals, the top one was used for trigger and the bottom one for the signal recording. The wire biasing the bottom mesh was soldered to the upper side of its frame. The wire conducts heat form the flange above and boils locally the liquid at its tip (as is explained in [53]), where the wire insulation is removed. Though usually undesired, this mechanism is used here to generate the bubble between the meshes.

Two different sets of meshes were used in this study. One set consisted of two woven stainless steel meshes with 50µm diameter wires spaced 0.5 mm apart. A second setup used a fine formed copper mesh (Precision E-Forming, MC-32) 15 µm wire width spaced 112 µm apart (78% maximal optical transparency) as the upper electrode and the previously used stainless steel electrode as the bottom mesh.

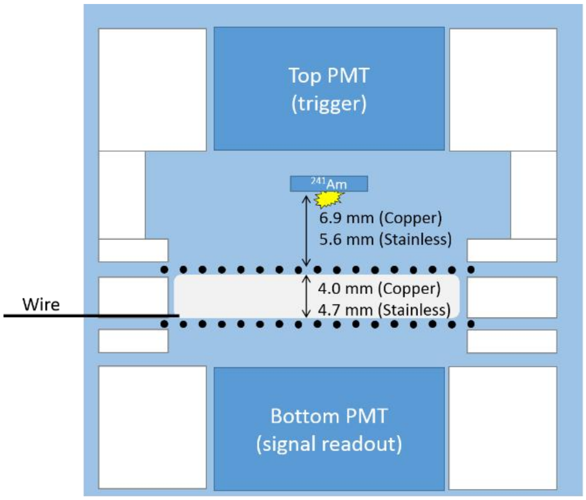

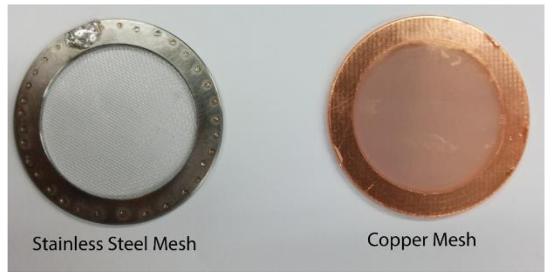

Figure 75 Left: experimental setup to confine bubble between two meshes. The wire biasing the electrode was used also as a heat source to inflate the bubble. Right: a picture of the two kinds of meshes used. The solder point on the stainless steel mesh is where the bias wire was soldered and where the bubbles were generated.

6.8.2 Results: bubble trapped below a woven stainless steel mesh

After the system has cooled down and temperatures have stabilized, bubbles from the tip of the wire started to form and raise towards the upper mesh. Sticking to the upper mesh, they coalesced into one large bubble (process taking ~20-30 seconds until covering the entire surface of the electrode). After ~30 seconds the bubble abruptly disappeared. This is probably caused due to eruption through the upper mesh. It is important to mention that this was already observed in the past where the bottom PMT was covered with a mesh and the wire biasing it conducted heat. The bubbles probably coalesced under it and then erupted suddenly. This is also probably the explanation for the “non-stable” and “super-stable” conditions which we have observed when LHM experiments as published in [46].

S2 signals were present whenever the bubbles reached below the active area of the source. Voltages applied were $V_{source} = -2800\,V$, $V_{top} = -2500\,V$, $V_{bottom} = +2500\,V$ corresponding to $E_{drift} = 0.5\,kV/cm$ and $E_{EL} = 10\,kV/cm$. However, since the bubble was constantly changing, there was no uniformity and no sensible energy spectrum could be recorded. Also the areas ratio $S2/S1 \sim 1$ seems to indicate a very poor EL magnitude.

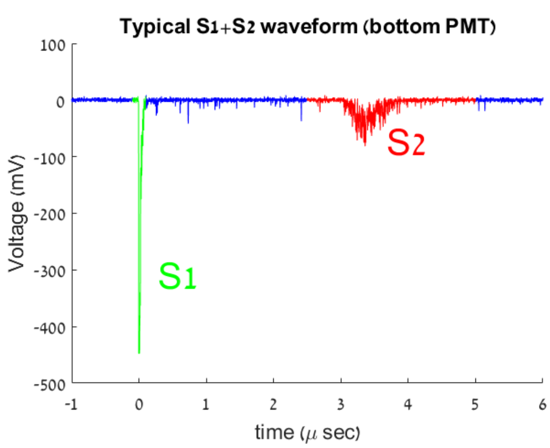

Figure 76 S1 and S2 signals from a bubble contained between two stainless steel meshes.

6.8.3 Results: bubble trapped below a formed copper mesh

In terms of bubble containment, the finer-pitch mesh showed much more stable operation. Here again, one could observe the appearance of a bubble under the electrode. The bubble grew to its final size and did not seem to change during some minutes of observation (specifically, it did not erupt though the mesh). Observing the bubble for a longer time was not possible since another bubble was forming under the bottom mesh (probably due to some residual boiling from the bottom of the vessel), thus hiding the area of interest.

S2 signals started appearing when applying voltage between the meshes ($V_{source} = -2800\, V$, $V_{top} = -2500\, V$, $V_{bottom} = +2500\, V$ corresponding to $E_{drift} = 0.4\, kV/cm$ and $E_{EL} = 13\, kV/cm$), however they were extremely low and very rare (< 1%). We attribute this, as will be discussed later, to the poor transmission of electrons form the liquid phase to the vapor phase which is located in the mesh holes. Note that the field between the electrodes is higher than the field required for reported full extraction of electrons from liquid to the gaseous phase (10 kV/cm [3], see Figure 1).

7 Summary, Discussion and Outlook

The LHM was conceived as a possible single-element sensor for combined detection of radiation-induced ionization charges and scintillation light in a noble liquid detection medium [45]. The original concept suggested detecting EL photons generated by ionization electrons and UV-induced photoelectrons in a CsI-coated micro pattern gas detector (MPGD) electrode immersed in the noble liquid. First results have shown copious photon yields emitted from the holes of a THGEM electrode immersed in LXe [47], however the low voltage onset threshold and the dependence on abrupt pressure changes led to the conclusion of EL emission from a gas bubble trapped underneath the electrode [46]. This was confirmed by a direct observation of a bubble with an external camera [53].

The work done during the course of this Ph.D. work aimed at deeper understanding of the mechanisms governing the performance of an LHM detector as well as demonstrating, for the first time, different properties and capabilities. The results presented in the above sections thus serve as a first basis of knowledge, but also open many new questions and investigation pathways.

When compiling the data throughout this thesis, measurements have consistently challenged the naïve assumption of 100% transmission of electrons form the liquid into the gas phase. It first appeared in the different light yields of the different electrode geometries and in the section 6.1.2.3, discussing EL photon generation on the heating wires. Then, in the most pronounced way, it appeared as a ~5 fold discrepancy between expected and measured PDE and the lower-then-expected energy resolution. Eventually, the inability of transferring electrons through a mesh supporting a bubble (as opposed to a hole-electrode supporting it) also indicated similar issues.

One mechanism proposed here to explain this effect, is as follows. As mentioned in the introduction, electrons experience a potential barrier when traversing from LXe to GXe (0.69V [3]). By carefully looking into the electrostatic simulations of the fields in the vicinity of a possible liquid-bubble interface (Figure 77), one notices a small component of the electric field which is tangent to the interface. An electron reaching this interface may be stopped when facing this potential barrier and start “gliding” over the liquid-to-bubble interface towards the bottom face of the electrode - getting absorbed either in the metallic part or on the insulating substrate. This mechanism may lead to loss of electrons, which is dependent on geometry, electric fields and bubble shape.

However, in order to experimentally tackle such a problem, it is first important to understand the exact shape of the phases interface. Such preliminary modeling and experimental, efforts have already started in our group, however have not yet produced conclusive results. The geometry of the liquid-gas interface depends on many parameters: the pressure differences in the bubble, the geometry of the hole, the surface tensions and the wetting angle of the liquid and the hole walls. The last two are important parameters which are currently not known to the desired accuracy (both in LXe and in LAr). Attempts to either measure all physical parameters or directly measure the liquid-gas interface are on-going. Eventually, since EL is produced only in the gas phase, the geometry of the interface has direct effect on EL yields and resolutions, both due to the geometry and due to the electric field configuration it imposes. A careful study of the bubble shape under these intense electric fields and the quantum processes involved in overcoming this potential barrier may shed light on the different processes and may lead to a successful design and operation of novel superior LHM electrodes.

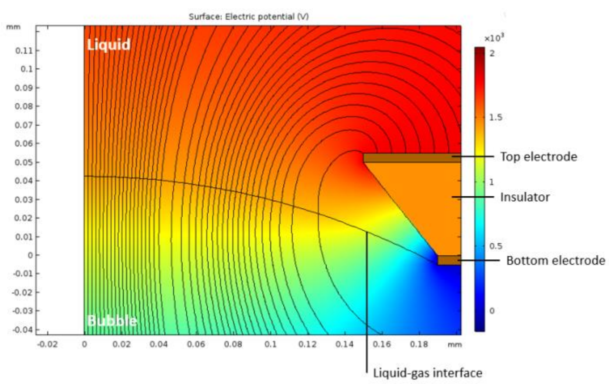

Figure 77 Finite element simulation of the potentials and electric-field lines of a 125µm SC-GEM with a spherical bubble penetrating ¼ hole-diameter up. The color field represents the potential. Simulation done at $E_d = 0.5\ kV/cm$, $\Delta V = 1{,}800V$, $E_t = -1kV/cm$. One can clearly see gliding down the bubble from the apex towards the bottom side of the electrode the potential drops. By carefully looking on the field lines, it is clear that there is a component of the electric field tangent to the bubble interface.

Following that, the question whether electrons do "glide" on the surface of the liquid before hopping to the gas needs to be addressed. In Figure 78 is a preliminary setup suggested to study the theory of charge "gliding" along the liquid-vapor interface. By comparing two situations, charge transport across the interface when the electric field is perpendicular to the phases interface and when it is tilted, one could understand how much charge is drifting away from the original position before tunneling across the interface. Such study requires however, high-precision measurements in a novel dedicated setup.

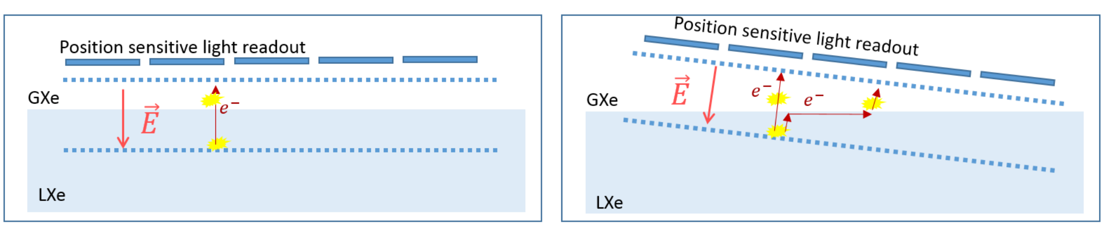

Figure 78 A suggestion on how to measure charge transport along and across liquid-vapor interface. Ionization charge is generated inside the liquid, electric field is generated between a mesh inside the liquid and an anode in the vapor. EL light is generated in the position in which the charge crosses into the gas phase. By comparing the tilted meshes configuration (right) to the horizontal orientation (left), one could understand whether the charge glides along the interface before crossing into the vapor.

Eventually, a serious improvement of the PDE value of the LXe-LHM (e.g. >15%) would permit conceiving large-volume local dual-phase LHM-based TPCs, e.g. for future dark-matter searches. A potential scheme, proposed within the DARWIN experiment R&D program [22] is shown in Figure 79. It consists of covering the TPC bottom with LHM modules. Preliminary GEANT4 simulations have shown that such a design may improve scintillation light collection, thus improving the sensitivity to low-energy WIMP-induced recoils [22].

Nevertheless, if low PDE values persist, the LHM could still be employed as ionization-charge detector. In such a case, the upper face of the electrode, instead of being covered with a photocathode, could be turned into a reflector. Imagining a DARWIN-like detector with reflective LHM electrode at the bottom of the cryostat (such as the one presented in Figure 79 below), may show superior energy resolution in charge detection due to precise control over the liquid-to-vapor interface while possibly maintaining overall light yield.

Last but not least, the LHM detector was so far examined only on ~30mm diameter prototypes, at shallow depth. For any future use, it is crucial to evaluate the operation of larger-area LHM detectors and at greater depth, where new problems maintaining stable bubbles may occur. The former is planned to be performed in collaboration with our colleagues at Ben-Gurion University and the latter is currently planned to be performed using the 2.7m deep LXe demonstrator (at University of Zurich) of the DARWIN experiment.

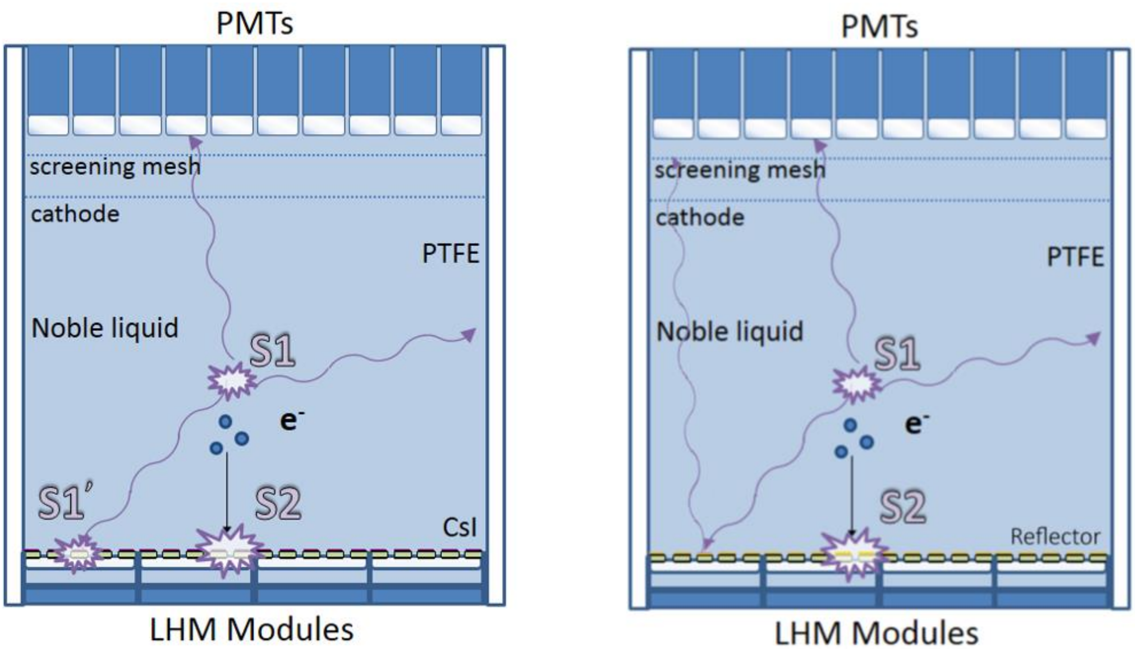

Figure 79 Left: Conceptual scheme of a large-scale single-phase noble-liquid TPC employing CsI-coated bubble-assisted LHM modules, as in Figure 1. The LHM modules constitute the anode plane and are sensitive to both the ionization electrons (which, in this scheme, drift downward) and S1 scintillation photons. There is no need for additional grids between the LHM modules and the TPC drift volume; only two grids are required – the cathode and a screening mesh protecting the top array of photon detectors (e.g., PMTs). Such a scheme can potentially have a more uniform S2 response than 'conventional' dual-phase TPCs, as well as an improved light collection ('light yield') efficiency, due to the reduced number of reflections (with the liquid-gas interface outside of the sensitive volume) and due to the reduced number of photon-absorbing mesh electrodes (two instead of five). Right: One could replace the CsI by a reflector, potentially enhancing the light collection to the top array of photomultipliers.

8 Appendix – First attempts towards a cryogenic RPWELL

8.1 Introduction

The Resistive Plate WELL detector (see Figure 80) [75] is a single-stage gas avalanche multiplier combining a single sided THGEM electrode coupled to the readout anode via a resistive layer, in a "well" configuration (the holes closed by the resistive plate form "wells"). Primary ionization charges drift from the ionization volume into the THGEM electrode's holes, where they undergo avalanche multiplication in the high field region. The charge generated in the holes induces a current on the anode and on the resistive layer. As this current reaches high values, the resistance causes a momentary voltage drop at the "head" of the avalanche, thus quenching further multiplication. The RPWELL has been developed in our group as a potential particle tracking detector; the focus is on its potential application as sampling element for future digital hadronic calorimeters [76]. Extensive laboratory and in-beam accelerator studies have been conducted at room temperature in a variety of gases and detector configurations [75, 77-80]. They showed a discharge-free operation at high charge gains (in Ne/5%CH4 and Ar/5%CO_2) even when exposed to highly ionization events and stable operation at counting rates reaching ~$\mathrm{kHz/mm^2}$ scale[75, 76]. Several resistive materials and detector configurations have been investigated at RT, the most successful Semitron ESD225 polymer (bulk resistivity $\rho \sim 10^9\ \Omega \cdot cm$) and doped silica glass (bulk resistivity $\rho \sim 10^8 - 10^9\ \Omega \cdot cm$) – both at RT.

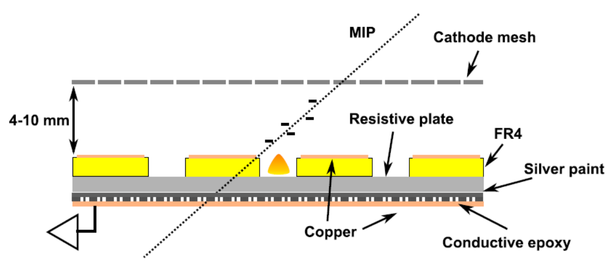

Figure 80 Schematic view of an RPWELL detector. A single sided THGEM is coupled to the anode via a resistive plate. Primary ionization electrons deposited in the drift gap are multiplied in the holes of the THGEM electrode. Spark damping is obtained by using a material with high enough bulk resistivity. Figure taken from [75].

The stability and discharge immunity of the RPWELL depends primarily on the resistivity of the plate screening the top THGEM electrode form the anode. A material with too low resistance would exhibit quenching of the discharge's energy but will not prevent it and a material with too high resistivity will result in charging up of the detector leading to significant rate-dependent gain variations.

The studies of RPWELL detectors as possible charge-amplifying elements in dual-phase Ar TPCs (~83K) aim at validating the possibility of reaching more stable, higher-gain operation in Ar vapor phase – compared to presently employed THGEM (LEM) elements; the avalanche gain in the latter is limited to ~10, for ~3,000 primary electrons reaching a single hole [38]. RPWELL operating at the vapor phase of dual-phase TPCs, at higher gains compared to that currently reachable with THGEM detectors, could make impact on future neutrino experiments. By generating higher charge-gain values with "resistive detectors", one could overcome charge attenuation over large drift paths and thus detect also lower-energy depositing particles, e.g., originating from supernovae neutrinos. Generating high avalanche gains in a pure noble gas is a long-standing unresolved issue. There are a few mechanisms limiting the gain, however to the best of our understanding, there has not been yet a proof as for which is the limiting factor. Specifically, the RPWELL addresses the issue of avoidance of the typical Reather limit of electron avalanches [81] in gas-avalanche detectors, by quenching the amount of charge generated in an avalanche and reducing the discharge energy.

The greatest challenge faced during the Ph.D. period was finding suitable resistive materials, of adequate ($10^9 - 10^{12}\Omega \cdot cm$) resistivity at low temperatures (down to 83K of LAr), for a cryogenic RPWELL detector. Most known materials show exponential temperature dependence (such as Semitron, Ceramic, Resistive glass), while a few others, of stable response over the above T range, do not have the right range of resistivity.

Extensive search for resistive materials with the right resistivity ($10^9 - 10^{12}\ \Omega \cdot cm$ [75]) at cryogenic temperatures yielded, so far, a Ferrite ceramic material (produced at collaborators in Instituto de Cerámica de Galicia) with $\sim 10^7\ \Omega \cdot \mathrm{cm}$ at RT, increasing with decreasing temperature to $\sim 10^{11}\ \Omega \cdot cm$ at LXe temperature (163 K). An RPWELL detector using this material has proved to quench sparks effectively when operated at LXe temperature with Ne/5%CH_4 [31]. It is though inappropriate at LAr temperature.

The search for material of correct resistivity at 83K, with the group of Instituto de Cerámica de Galicia, has also led to some ferrite ceramics with $\rho \sim 10^8\ \Omega \cdot cm$, increasing with temperature, to $\sim 10^{11}\ \Omega \cdot cm$ at LAr temperatures. So far only a single sample was provided for evaluation. Resistivity measurements as a function of temperature were carried out; however, due to poorly designed experiments results were not reproducible.

First preliminary measurements of an RPWELL in LAr, did not show high enough gain to overcome electronic noise. However, measurements of breakdown voltage as a function of the temperature with and without the resistive material clearly indicated a certain avalanche-quenching effect as discussed below.

8.2 Results - Discharge quenching in RPWELL structure

The Paschen [82] breakdown voltage is the minimal voltage necessary to start a discharge between two electrodes. The law states that at higher pressures (above a few mbar) the breakdown characteristics of a gap are a function (generally not linear) of the product of the gas pressure (p) and the gap length (d), usually written as $V_B = f(pd)$, where V_B is the breakdown voltage. Indeed, at room temperature, we could apply higher voltage in the RPWELL detector relative to the one we could apply for "standard" WELL (single-faced electrode directly coupled to a conductive anode, without resistive plate) [75]. This allowed us to reach higher avalanche gain when using RPWELL [75]. A key to the success of the Cryo-RPWELL to outperform regular THGEM/LEM-like configurations is the ability to reach higher breakdown voltages also at LAr temperature.

First measurements comparing the breakdown-voltage values of standard WELL and RPWELL detectors (Fe-doped ceramics with $10^6-10^7\ \Omega cm$ bulk resistivity at room temperature), as a function of the temperature, is shown in Figure 82; the pressure was kept constant ~1100 mbar. At room temperature, the breakdown voltage of the standard WELL and RPWELL is similar. This is explained by the fact that at room temperature the bulk resistivity of the resistive plate is too low and does not quench breakdowns. However, at lower temperatures, the resistivity increases and its effect on the breakdown voltage becomes pronounced. Similarly to room temperature, these preliminary measurements prove that also at cryogenic temperatures the resistive plate could play a role in discharge quenching. It is therefore a first indication for the possibility of operating an RPWELL detector in the vapor phase of LAr and it is suggested to pursue in this direction in the future.

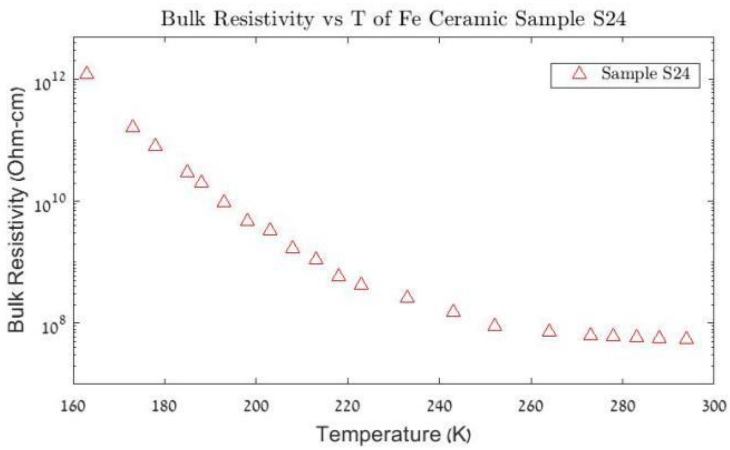

Figure 81 The bulk resistivity as a function of temperature of one sample of Fe-doped ceramic material produced by our collaborator at the Instituto de Cerámica de Galicia (Spain).

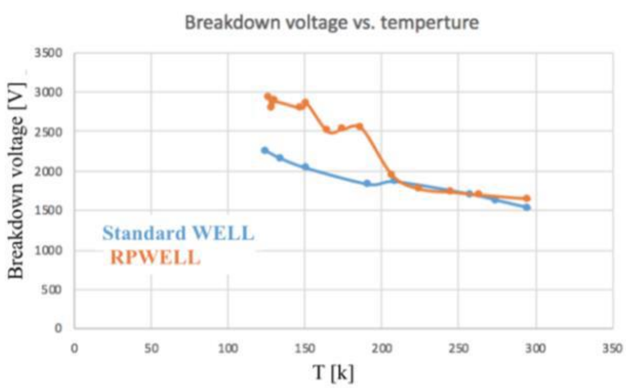

Figure 82 The Paschen breakdown voltage of an RPWELL (Fe-doped ceramic Resistive Plate with bulk resistivity at the order of 106−107 Ωcm at room temperature.

9 List of Publications

Within this Ph.D. work

1. Erdal, E., et al., Bubble-assisted Liquid Hole Multipliers in LXe and LAr: towards "local dual-phase TPCs". Conference proceedings of *JINST*, 2019. **15**(04): p. C04002.
2. Erdal, E., et al., *First demonstration of a bubble-assisted Liquid Hole Multiplier operation in liquid argon. JINST*, 2019. **14**(11): p. P11021.
3. Erdal, E., et al., *First imaging results of a bubble-assisted Liquid Hole Multiplier with SiPM readout in liquid xenon. JINST*, 2019. **14**(01): p. P01028.
4. Erdal, E., et al., *Recent advances in bubble-assisted Liquid Hole-Multipliers in liquid xenon. JINST*, 2018. **13**(12): p. P12008.
5. Erdal, E., et al., *First demonstration of VUV-photon detection in liquid xenon with THGEM and GEM-based Liquid Hole Multipliers. Nucl. Instrum. Meth. A* **845**(2017) 218.
6. Erdal, E., et al., *Direct observation of bubble-assisted electroluminescence in liquid xenon. JINST*, 2015. **10**(11): p. P11002.
7. Aalbers, J., et al. (incl. E. Erdal), DARWIN: towards the ultimate dark matter detector. *Journal of Cosmology and Astroparticle Physics*, 2016. 2016(11): p. 017.

Within the M.Sc. work

1. Arazi, L., Erdal, E.*, et al., *Liquid Hole Multipliers: bubble-assisted electroluminescence in liquid xenon. JINST*, 2015. **10**(08): p. P08015. (*equal contribution)

10 List of abbreviations

APD	avalanche photodiode
COG	center of gravity
DM	Dark Matter
EL	electroluminescence
GEM	Gaseous electron multiplier
GPM	Gaseous photon multiplier
LAr	liquid argon
LEM	Large electron multiplier
LHM	Liquid Hole Mulitiplier
LN2	liquid nitrogen
LXe	liquid xenon
MPGD	Micro pattern gaseous detector
MPPC	Multi pixel photon counter
PC	photocathode
PDE	photon detection efficiency
PE	photoelectron
PMT	photomultiplier tube
PTFE	polytetrafluoroethylene (Teflon)
QE	quantum efficiency
RPWELL	Resistive plate well
SC-GEM	Single conical GEM
SiPM	silicon photomultiplier
THGEM	Thick gaseous electron multiplier
TPB	tetraphenyl butadiene
TPC	time projection chamber
UV	ultraviolet
VUV	vacuum ultra violet
WIMP	Weakly interacting massive particle

Experimental setups acronyms

MiniX	Mini Xenon Apparatus
WISArD	Weizmann Institute of Science Argon Detector
WILiX	Weizmann Institute Liquid Xenon apparatus

11 Bibliography

1. Baudis, L., *Direct dark matter detection: the next decade.* Physics of the Dark Universe, 2012. **1**(1): p. 94-108.
2. Aprile, E. and T. Doke, *Liquid xenon detectors for particle physics and astrophysics.* Reviews of Modern Physics, 2010. **82**(3): p. 2053.
3. Chepel, V. and H. Araújo, *Liquid noble gas detectors for low energy particle physics.* Journal of Instrumentation, 2013. **8**(04): p. R04001.
4. Karagiorgi, G., *Current and future liquid argon neutrino experiments.* arXiv preprint arXiv:1304.2083, 2013.
5. Auger, M., et al., *Search for neutrinoless double-beta decay in Xe 136 with EXO-200.* Physical Review Letters, 2012. **109**(3): p. 032505.
6. Rubbia, C., et al., *Underground operation of the ICARUS T600 LAr-TPC: first results.* Journal of Instrumentation, 2011. **6**(07): p. P07011.
7. Mihara, S. *MEG liquid xenon detector*. in *Journal of Physics: Conference Series*. 2011. IOP Publishing.
8. Grignon, C., et al., *Nuclear medical imaging using β+ γ coincidences from 44 Sc radio-nuclide with liquid xenon as detection medium.* Nuclear Instruments and Methods in Physics Research Section A: Accelerators, Spectrometers, Detectors and Associated Equipment, 2007. **571**(1): p. 142-145.
9. Breskin, A., et al., *A novel liquid-Xenon detector concept for combined fast-neutrons and gamma imaging and spectroscopy.* Journal of Instrumentation, 2012. **7**(06): p. C06008.
10. Vartsky, D., et al., *Liquid-Xe detector for contraband detection.* Nuclear Instruments and Methods in Physics Research Section A: Accelerators, Spectrometers, Detectors and Associated Equipment, 2016. **824**: p. 240-242.
11. Israelashvili, I., et al., *A comprehensive simulation study of a Liquid-Xe detector for contraband detection.* Journal of Instrumentation, 2015. **10**(03): p. P03030.
12. Berger, M.J., Hubbell, J.H., Seltzer, S.M., Chang, J., Coursey, J.S., Sukumar, R., Zucker, D.S., and Olsen, K. *XCOM: Photon Cross Section Database (version 1.5)*. 2010; Available from: http://physics.nist.gov/xcom.
13. Aprile, E., *The XENON1T dark matter search experiment*, in *Sources and Detection of Dark Matter and Dark Energy in the Universe*. 2013, Springer. p. 93-96.
14. Acciarri, R., et al., *Long-baseline neutrino facility (LBNF) and deep underground neutrino experiment (DUNE) conceptual design report, volume 4 the DUNE detectors at LBNF.* arXiv preprint arXiv:1601.02984, 2016.
15. Bethe, H. and J. Ashkin, *The passage of heavy particles through matter.* Experimental nuclear physics, 1953. **1**: p. 166-201.
16. Berger, M.J., Coursey, J.S., Zucker, M.A., and Chang, J. . *ESTAR, PSTAR, and ASTAR: Computer Programs for Calculating Stopping-Power and Range Tables for Electrons, Protons, and Helium Ions (version 1.2.3)*. 2005; Available from: http://physics.nist.gov/Star
17. Aalseth, C.E., et al., *DarkSide-20k: A 20 tonne two-phase LAr TPC for direct dark matter detection at LNGS.* The European Physical Journal Plus, 2018. **133**(3): p. 131.
18. NIST. *NIST Chemistry WebBook*. 2018; Available from: https://webbook.nist.gov/chemistry/.
19. Solovov, V., et al., *Measurement of the refractive index and attenuation length of liquid xenon for its scintillation light.* Nuclear Instruments and Methods in Physics Research Section A: Accelerators, Spectrometers, Detectors and Associated Equipment, 2004. **516**(2-3): p. 462-474.
20. Babicz, M., et al., *Propagation of scintillation light in Liquid Argon.* Journal of Instrumentation, 2020. **15**(03): p. C03035.

21. Aprile, E., et al., *Measurements of proportional scintillation and electron multiplication in liquid xenon using thin wires.* Journal of Instrumentation, 2014. **9**(11): p. P11012.
22. Aalbers, J., et al., *DARWIN: towards the ultimate dark matter detector.* Journal of Cosmology and Astroparticle Physics, 2016. **2016**(11): p. 017.
23. Marchionni, A., et al. *ArDM: a ton-scale LAr detector for direct Dark Matter searches*. in *Journal of Physics: Conference Series*. 2011. IOP Publishing.
24. Aprile, E., et al., *Observation of Excess Electronic Recoil Events in XENON1T.* arXiv preprint arXiv:2006.09721, 2020.
25. Dawson, J. and D. collaboration. *Status of ProtoDUNE Dual Phase*. in *Journal of Physics: Conference Series*. 2019. IOP Publishing.
26. Bolozdynya, A.I., *Emission detectors*. 2010: World Scientific.
27. Bondar, A., et al., *Electron emission properties of two-phase argon and argon-nitrogen avalanche detectors.* Journal of Instrumentation, 2009. **4**(09): p. P09013.
28. Buzulutskov, A. and A. Bondar, *Electric and Photoelectric Gates for ion backflow suppression in multi-GEM structures.* Journal of Instrumentation, 2006. **1**(08): p. P08006.
29. Igarashi, T., et al., *Performance of VUV-sensitive MPPC for liquid argon scintillation light.* Nuclear Instruments and Methods in Physics Research Section A: Accelerators, Spectrometers, Detectors and Associated Equipment, 2016. **833**: p. 239-244.
30. Bondar, A., et al., *MPPC versus MRS APD in two-phase Cryogenic Avalanche Detectors.* Journal of Instrumentation, 2015. **10**(04): p. P04013.
31. Roy, A., et al., *First results of Resistive-Plate Well (RPWELL) detector operation at 163 K.* Journal of Instrumentation, 2019. **14**(10): p. P10014.
32. Arazi, L., et al., *First results of a large-area cryogenic gaseous photomultiplier coupled to a dual-phase liquid xenon TPC.* Journal of Instrumentation, 2015. **10**(10): p. P10020.
33. Hamilton, P., *First Measurement of Neutrino Interactions in MicroBooNE.* arXiv preprint arXiv:1611.00820, 2016.
34. Akerib, D., et al., *The large underground xenon (LUX) experiment.* Nuclear Instruments and Methods in Physics Research Section A: Accelerators, Spectrometers, Detectors and Associated Equipment, 2013. **704**: p. 111-126.
35. Yang, Y., *Search for dark matter from the first data of the PandaX-II experiment.* arXiv preprint arXiv:1612.01223, 2016.
36. Alexander, T., et al., *DarkSide search for dark matter.* Journal of Instrumentation, 2013. **8**(11): p. C11021.
37. Tonazzo, A. and W. Collaboration. *WA105: a large-scale demonstrator of the Liquid Argon double phase TPC*. in *Journal of Physics: Conference Series*. 2016. IOP Publishing.
38. Badertscher, A., et al., *First operation and performance of a 200 lt double phase LAr LEM-TPC with a 40× 76 cm2 readout.* Journal of Instrumentation, 2013. **8**(04): p. P04012.
39. Bondar, A., et al., *Direct observation of avalanche scintillations in a THGEM-based two-phase Ar avalanche detector using Geiger-mode APD.* Journal of Instrumentation, 2010. **5**(08): p. P08002.
40. Howlett, J., E. Aprile, and X. Team, *The XENONnT Dark Matter Search Experiment.* APS, 2019. **2019**: p. H17. 006.
41. Baudis, L., et al., *Characterisation of Silicon Photomultipliers for liquid xenon detectors.* Journal of Instrumentation, 2018. **13**(10): p. P10022.
42. Fischer, P., et al. *SPAD array chips with full frame readout for crystal characterization*. in *Ejnmmi Physics*. 2015. SpringerOpen.
43. Ferenc, D., A. Chang, and M.Š. Ferenc, *The Novel ABALONE Photosensor Technology: 4-Year Long Tests of Vacuum Integrity, Internal Pumping and Afterpulsing.* arXiv preprint arXiv:1703.04546, 2017.

44. Cantini, C., et al., *Performance study of the effective gain of the double phase liquid Argon LEM Time Projection Chamber.* Journal of Instrumentation, 2015. **10**(03): p. P03017.
45. Breskin, A. *Liquid Hole-Multipliers: A potential concept for large single-phase noble-liquid TPCs of rare events*. in *Journal of Physics: Conference Series*. 2013. IOP Publishing.
46. Arazi, L., et al., *Liquid Hole Multipliers: bubble-assisted electroluminescence in liquid xenon.* Journal of Instrumentation, 2015. **10**(08): p. P08015.
47. Arazi, L., et al., *First observation of liquid-xenon proportional electroluminescence in THGEM holes.* Journal of Instrumentation, 2013. **8**(12): p. C12004.
48. Erdal, E., et al., *First demonstration of VUV-photon detection in liquid xenon with THGEM and GEM-based Liquid Hole Multipliers.* Nuclear Instruments and Methods in Physics Research Section A: Accelerators, Spectrometers, Detectors and Associated Equipment, 2016.
49. Sauli, F., *GEM: A new concept for electron amplification in gas detectors.* Nuclear Instruments and Methods in Physics Research Section A: Accelerators, Spectrometers, Detectors and Associated Equipment, 1997. **386**(2): p. 531-534.
50. Breskin, A., et al., *A concise review on THGEM detectors.* Nuclear Instruments and Methods in Physics Research Section A: Accelerators, Spectrometers, Detectors and Associated Equipment, 2009. **598**(1): p. 107-111.
51. Breskin, A., *CsI UV photocathodes: history and mystery.* Nuclear Instruments and Methods in Physics Research Section A: Accelerators, Spectrometers, Detectors and Associated Equipment, 1996. **371**(1): p. 116-136.
52. Erdal, E., et al., *Recent advances in bubble-assisted Liquid Hole-Multipliers in liquid xenon.* Journal of Instrumentation, 2018. **13**(12): p. P12008.
53. Erdal, E., et al., *Direct observation of bubble-assisted electroluminescence in liquid xenon.* Journal of Instrumentation, 2015. **10**(11): p. P11002.
54. Pinto, S.D., et al., *Progress on large area GEMs.* Journal of Instrumentation, 2009. **4**(12): p. P12009.
55. *COMSOL Multiphysics® v. 5.4*. Available from: www.comsol.com.
56. Aprile, E., et al., *Performance of CsI photocathodes in liquid Xe, Kr, and Ar.* Nuclear Instruments and Methods in Physics Research Section A: Accelerators, Spectrometers, Detectors and Associated Equipment, 1994. **338**(2-3): p. 328-335.
57. Brooks, H., et al., *Electron drift velocities in xenon.* Journal of Physics D: Applied Physics, 1982. **15**(6): p. L51.
58. Aprile, E., R. Mukherjee, and M. Suzuki, *Ionization of liquid xenon by 241Am and 210Po alpha particles.* Nuclear Instruments and Methods in Physics Research Section A: Accelerators, Spectrometers, Detectors and Associated Equipment, 1991. **307**(1): p. 119-125.
59. Weber, M., *Gentle neutron signals and noble background in the XENON100 dark matter search experiment*. 2013, Ruprecht-Karls-Universität Heidelberg.
60. Erdal, E., *Estimating average energy of non-spectroscopic 241Am source (internal report)*. 2017.
61. NIST. *X-Ray Mass Attenuation Coefficient*. 2018; Available from: https://www.nist.gov/pml/x-ray-mass-attenuation-coefficients.
62. Faham, C., et al., *Measurements of wavelength-dependent double photoelectron emission from single photons in VUV-sensitive photomultiplier tubes.* Journal of Instrumentation, 2015. **10**(09): p. P09010.
63. Araujo, G., T. Pollmann, and A. Ulrich, *Photoluminescence response of acrylic (PMMA) and polytetrafluoroethylene (PTFE) to ultraviolet light.* The European Physical Journal C, 2019. **79**(8): p. 1-8.
64. K.K., H.P., *VUV-MPPC 4th generation Product Flyer*. 2016.

65. Vartzky, D., *Calculation of reconstructed light point source position for 4 SiPMs (internal report)*. 2018.
66. Yamamoto, K., et al. *Development of multi-pixel photon counter (MPPC)*. in *2006 IEEE Nuclear Science Symposium Conference Record*. 2006. IEEE.
67. Liu, C.-Y. and A.L. Goertzen, *Improved event positioning in a gamma ray detector using an iterative position-weighted centre-of-gravity algorithm.* Physics in Medicine & Biology, 2013. **58**(14): p. N189.
68. Gray, R.M. and A. Macovski, *Maximum a posteriori estimation of position in scintillation cameras.* IEEE Transactions on Nuclear Science, 1976. **23**(1): p. 849-852.
69. Morozov, A., et al., *Adaptive algorithms of position and energy reconstruction in Anger-camera type detectors: experimental data processing in ANTS.* Journal of Instrumentation, 2013. **8**(05): p. P05002.
70. Erdal, E., et al., *First imaging results of a bubble-assisted Liquid Hole Multiplier with SiPM readout in liquid xenon.* Journal of Instrumentation, 2019. **14**(01): p. P01028.
71. Amsler, C., et al., *Luminescence quenching of the triplet excimer state by air traces in gaseous argon.* Journal of Instrumentation, 2008. **3**(02): p. P02001.
72. Bonesini, M., et al., *An innovative technique for TPB deposition on convex window photomultiplier tubes.* Journal of Instrumentation, 2018. **13**(12): p. P12020.
73. Veloso, J., et al., *The Photon-Assisted Cascaded Electron Multiplier: a concept for potential avalanche-ion blocking.* Journal of Instrumentation, 2006. **1**(08): p. P08003.
74. Breskin, A., et al., *High flux operation of the gated multistep avalanche chamber*, in *Research On Particle Imaging Detectors*. 1995, World Scientific. p. 264-278.
75. Rubin, A., et al., *First studies with the Resistive-Plate WELL gaseous multiplier.* Journal of Instrumentation, 2013. **8**(11): p. P11004.
76. Bressler, S., et al., *Recent advances with THGEM detectors.* Journal of Instrumentation, 2013. **8**(12): p. C12012.
77. Arazi, L., et al., *Laboratory studies of THGEM-based WELL structures with resistive anode.* Journal of Instrumentation, 2014. **9**(04): p. P04011.
78. Bressler, S., et al., *Beam studies of novel THGEM-based potential sampling elements for Digital Hadron Calorimetry.* Journal of Instrumentation, 2013. **8**(07): p. P07017.
79. Moleri, L., et al., *The Resistive-Plate WELL with Argon mixtures-a robust gaseous radiation detector.* Nuclear Instruments and Methods in Physics Research Section A: Accelerators, Spectrometers, Detectors and Associated Equipment, 2016.
80. Moleri, L., et al., *In-beam evaluation of a medium-size Resistive-Plate WELL gaseous particle detector.* Journal of Instrumentation, 2016. **11**(09): p. P09013.
81. Raether, H., *Electron avalanches and breakdown in gases.* 1964.
82. Paschen, F., *Ueber die zum Funkenübergang in Luft, Wasserstoff und Kohlensäure bei verschiedenen Drucken erforderliche Potentialdifferenz.* Annalen der Physik, 1889. **273**(5): p. 69-96.